

https://dspace.org/

Electronic properties of single walled carbon nanotubes synthesized by laser ablation

Ncube, Siphephile

2014-07-21
http://hdl.handle.net/10539/14938

Downloaded from a DSpace repository. https://dspace.org/

Electronic properties of single walled carbon nanotubes synthesized by laser ablation

Siphephile Ncube

A dissertation submitted to the Faculty of Science, University of the Witwatersrand, Johannesburg, in fulfillment of the requirements for the degree of Master of Science

Johannesburg, 2013

DECLARATION

I declare that this dissertation is my own, unaided work. It is being submitted for the Degree of Master of Science in the University of the Witwatersrand, Johannesburg. It has not been submitted before for any degree or examination in any other University.

11th day of November 2013

ABSTRACT

Current research in the field of nano-electronics is directed towards device miniaturization in order to find ways to increase the speed of electronic devices. The work presented in this dissertation is on the electronic transport properties of single walled carbon nanotube (SWNT) ropes synthesized by laser ablation. The measurements were performed on devices with different geometries; namely SWNT mats, metal incorporated (aligned individual and bundled) SWNTs and lastly on aligned pure SWNTs from low temperatures up to room temperature. The work was performed so as to gain an understanding on how best to utilize SWNTs in the semiconductor industry towards miniaturization. Such an understanding would ultimately highlight if SWNTs can be considered as a viable alternative to the current silicon-based technology, which seems to be approaching its physical limit.

For a mat of SWNTs, 3D-Variable range hopping is the principal conduction mechanism from 2 K – 300 K. The magneto-resistance was found to be predominantly negative with a parabolic nature which converts to a linear nature as the temperature is increased. The negative MR is a consequence of quantum interference and the positive upturn is attributed to wave function shrinkage at low temperatures as described by the Efros-Shklovskii model. The hopping ranges of the electrons for a SWNT mat increases as the temperature decreases due to manifestation of quantum effects and reduced scattering. It was also found that metal incorporation does not alter the properties of the SWNT significantly.

SWNT ropes aligned by di-electrophoresis across a 1 micron gap between gold micro-electrodes, exhibit Tomonaga-Luttinger liquid (TLL) like behaviour, within the 80 K – 300 K temperature range. The effects of confinement and electron-electron interaction unique to one dimension were identified in electronic transport

as a non-universal power law dependence of the differential conductance on temperature and source-drain voltage. Ballistic conductance at room temperature was confirmed from the high frequency transport of the SWNT devices. The complex impedance showed some oscillatory behaviour in the frequency range 6 to 30 GHz, as has been predicted theoretically in the Tomonaga-Luttinger Liquid model.

The observation of Luttinger Liquid behaviour demonstrates the outstanding nature of these one-dimensional molecular systems. In these devices the charging Coulomb energy of a single particle played a critical role in the overall device performance. This study can be used to understand the nature of dynamics of plasmons which are the charge carriers in a TLL system and how Coulomb interactions can be used to design highly tuneable systems for fabrication of single molecule devices.

The incorporation of metal onto individual SWNT ropes does not alter its electronic properties significantly but the properties of the bundled metal incorporated SWNT ropes are altered. This study has found that under optimized conditions SWNTs might be a viable option for incorporation in nano electronics devices. Individual SWNT ropes promise better devices compared to SWNT mats and further work should be done on individual SWNTs.

DEDICATION

To my parents Robert and Zulu.

ACKNOWLEDGEMENTS

Many people deserve credit for guidance, assistance, support and encouragement in this project. First and foremost, I would like to appreciate and thank all those who contributed towards making this project a success. A special acknowledgment goes to the DST/NRF Centre of Excellence in Strong Materials (COE) for the financial support throughout my MSc studies.

Much credit goes my supervisor, Prof Somnath Bhattacharyya, founder of the Nanoscale Transport Physics Lab, who taught and gave me guidance, and supervised this project in a special and wonderful way. I started the project with little or no idea, but with his guidance and patience, I developed the confidence, skills and knowledge to go through it. Thanks a million! A special acknowledgment to Dr Z. Chiguvare for his contribution. Thank you for the guidance and support that lead to this breakthrough. I thank the exceptional members of the Nanoscale Transport Lab, George Chimowa for the high frequency measurements, Ross McIntosh, Chris Coleman, and Kirsty Sanders. Thank you to each one of you for the countless discussions we had, the encouraging words and mostly for being good friends. I also extend my gratitude to Dr R. Erasmus, Dr S. Durbach, Dr M.K. Moodley, Prof N. J. Coleville, members of the CATOMAT group, Mr C. Sandrock, the members of the Physics Workshop and the School of Physics for assisting me with various aspects of my research.

I would also like to thank my family and friends for their moral support. To my parents, all my brothers and sisters, thank you for remembering me in your prayers. To Nkosi and Sibongile, Thandi, Thuba, the Mushangwe's, thank you for sacrificing a lot to bring joy and happiness in my life. May God bless you! To Kim, thank you for being the driving force in my ambition. Most of all I would to thank the Almighty God for his unfailing LOVE and MERCY.

TABLE OF CONTENTS

DECLARATION ii
ABSTRACT iii
DEDICATION v
ACKNOWLEDGEMENTS vi
TABLE OF CONTENTS vii
LIST OF FIGURES xi
LIST OF TABLES xiv
ACRONYMS xv

1 Introduction 1
1.1 Current research direction 1
1.2 Background 1
1.3 Aim and Objectives 3
1.4 Motivation 4
1.5 Summary 5

2 Literature Review 7
2.1 Allotropes of carbon 7
2.1.1 Diamond 8
2.1.2 Graphene 9
2.1.3 Graphite 10
2.1.4 Fullerene 11
2.2 Properties of single walled nanotubes 13
2.2.1 Physical properties 14
2.2.2 Electronic properties 16
2.2.3 High frequency properties 18

2.2.4 Magnetic properties 19
2.3 Synthesis methods 20
2.3.1 Growth mechanism 20
2.3.2 Arc discharge 21
2.3.3 Chemical Vapour Deposition 22
2.3.4 Laser ablation 23
2.4 Di-electrophoresis of single-walled carbon nanotubes 24
2.5 Electronic transport in low dimensional structures 25
2.5.1 Ballistic transport in metallic SWNT 25
2.5.2 The Coulomb Blockade effect in SWNT 28
2.6 DC conductivity in carbon nanotubes 29
2.7 Magneto conductivity 30

3 Synthesis of Single WalledCarbon Nanotubes by LaserAblation 32
3.1 Laser development and operation principles 32
3.1.1 Laser development 32
3.1.2 Design of a laser 33
3.1.3 Principle of operation 34
3.2 Laser matter interaction 36
3.3 Laser ablation - experimental 37
3.3.1 Overview of experimental setup 37
3.3.2 Description of the Nd:YAG laser components 38
3.3.3 Beam alignment procedure 39
3.4 Synthesis of single walled carbon nanotubes 40
3.4.1 Target preparation 40
3.4.2 Synthesis process 42
3.5 Summary 44

4 Experimental 46

4.1 Introduction 46
4.2 Structural characterization 46
4.2.1 Raman analysis 46
4.2.2 Electron Microscopy 48
4.3 Low temperature transport measurements 51
4.3.1 Device fabrication by Di-electrophoresis 51
4.3.2 Modification by metal incorporation 55
4.3.3 Measurement under a Probe-Station. 56
4.3.4 Measurement in the Cryogenic system. 59

5 Results and Discussion 60
5.1 Introduction 60
5.2 Synthesis process optimization 60
5.2.1 Raman analysis of SWNTs 68
5.2.2 Summary of synthesis conditions 70
5.3 Electronic transport through SWNT mats. 71
5.3.1 Electrical resistance 72
5.3.2 Magneto-resistance 75
5.3.3 Discussion 81
5.4 Electronic transport in a rope of metal incorporated SWNTs. 83
5.4.1 Raman spectroscopy studies 85
5.4.2 Electronic transport studies 86
5.5 Conclusion 88

6 Luttinger Liquid behaviour in single walled carbon nanotube ropes 89
6.1 Introduction 89
6.1.1 Luttinger liquid model 89
6.2 Electronic transport in single walled carbon nanotube ropes 94
6.2.1 Di-electrophoresis process optimization 94

6.2.2 Current voltage characteristics 97
6.2.3 Conductance of aligned SWNT ropes 99
6.2.4 Differential Conductance 101
6.3 Luttinger liquid behaviour in SWNT ropes 104
6.4 Frequency response studies 107
6.5 Discussion 110

7 Conclusions and recommendations 111
7.1 Synthesis of single walled carbon nanotubes 111
7.2 Electronic transport in single walled carbon nanotubes 111
7.3 Future outlook 114

References 115

LIST OF FIGURES

Figure 2.1: Crystal structure of diamond..... 8
Figure 2.2: Graphene crystal structrure..... 9
Figure 2.3: Crystal structure of graphite 10
Figure 2.4: Buckminsterfullerene, C_{60} crystal structure..... 11
Figure 2.5: Illustration of the stepwise formation of a carbon nanotube 13
Figure 2.6: A "de Heer" abacus showing the different chiralities..... 14
Figure 2.7: Models of different SWNTs. 15
Figure 2.8: Sketch of band structure and DOS for semiconducting and metallic SWNTs..... 17
Figure 2.9: Visualization of a possible carbon nanotube growth mechanism. 21
Figure 2.10: Arc discharge experimental setup..... 21
Figure 2.11: Chemical vapor deposition experimental set up..... 22
Figure 2.12: Laser ablation experimental setup 24
Figure 2.13: The normalized conductivity of mats and a rope of SWNT,..... 30
Figure 3.1: Overview of experimental setup 37
Figure 3.2: Experimental setup of laser ablation synthesis of SWNT 43
Figure 4.1: JEOL 7001F SEM facility used for structural characterization... 49
Figure 4.2: Di-electrophoreisis experimental setup 52
Figure 4.3: Hall microstructure used to fabricate devices by DEP 53
Figure 4.4: Agilent B1500A Semiconductor Device Analyze 56
Figure 4.5: Gold microstructure used for fabrication of devices placed on the semiconductor analyzer probe station sample chuck..... 57
Figure 4.6: Cryogenic measurement system for low temperature electronic transport characterization of SWNT mats. 59

Figure 5.1: SEM image and Raman of material produced before optimization of the process parameters 61
Figure 5.2: SEM image of SWNTs produced at a low laser power 61
Figure 5.3: SEM image and Raman spectra of material at temperatures lower than 900 K..... 62
Figure 5.4: SEM image and Raman spectra of low yield SWNT due to target contamination..... 63
Figure 5.5: SEM image of SWNT nanotubes produced after optimization of all process parameters..... 64
Figure 5.6: Raman spectra of SWNTs bundles aftyer opimization..... 64
Figure 5.7: SEM and TEM image of the as prepared material..... 65
Figure 5.8: SEM images after purification..... 66
Figure 5.9: TEM image of a single rope of SWNT..... 67
Figure 5.10: Individual SWNT ropes on Si substrate. 68
Figure 5.11: Raman spectra taken at different laser excitation wavelengths ... 70
Figure 5.12: Resistance as a function of temperature of SWNT 72
Figure 5.13: Mott R-T fits dependence data for a SWNT mat..... 74
Figure 5.14: Resistance against magnetic field at different temperatures..... 75
Figure 5.15: Magneto-resistance at different temperatures..... 76
Figure 5.16: Positive magneto resistance at low temperature 78
Figure 5.17: Temperature dependence of a_1..... 80
Figure 5.18: Calculated a_2 at different temperatures..... 81
Figure 5.19: SEM image of metal incorporated SWNT ropes before purification..... 84
Figure 5.20: SEM image of metal incorporated of SWNT ropes after purification..... 84
Figure 5.21: Raman Spectra of metal incorporated SWNT 85
Figure 5.22: I-V curve for bundled metal incorporated SWNT 86
Figure 5.23: I-V of individual metal incorporated SWNTs 87

Figure 6.1: Illustration of electrons tunnelling into a Fermi liquid and Luttinger liquid 90
Figure 6.2: Illustration of charge density and spin density waves propagating at different velocities 92
Figure 6.3: Device fabricated from DEP at a low voltage 95
Figure 6.4: Device fabricated by DEP at a high frequency..... 96
Figure 6.5: SEM of efficiently aligned SWNT at optimized DEP..... 97
Figure 6.6: (a-c) DEP aligned SWNT ropes (d) Sketch showing the 1D model satisfying the condition $d_t << L$ 98
Figure 6.7: Typical I-V characteristicsfor aligned SWNT ropes 99
Figure 6.8 : Resistance – temperature dependence of SWNT ropes at different voltages 100
Figure 6.9: Differential Conductance against bias voltage from 77 K to room temperature 102
Figure 6.10: (a)Differential conductance as a function of applied bias voltage at selected temperatures (b) Double log plots show the power laws…… 103
Figure 6.11: Differential conductance against voltage showing scaling of the in the high field limit..... 105
Figure 6.12: Collapsed curves in universal scaling coordinates 106
Figure 6.13: Scattering parameters S_1..... 107
Figure 6.14: Real and Imaginary Impedance of SWNTs after de-embedding 108
Figure 6.15: Real Impedance of SWNTs showing and oscillatory response.The inset shows the device configuration employed 109

LIST OF TABLES

Table 3.1: Nd: YAG PRO 270 expected performance 39
Table 3.2: Target Pressing conditions 41
Table 3.3: Optimized process parameters 42
Table 5.1: Calculated parameters from R (T) and R (H) data 79

ACRONYMS

SWNT	Single walled carbon nanotube
CNT	Carbon nanotube
TLL	Tomonaga-Luttinger Liquid
1D	One dimensional
DEP	Di-electrophoresis
CVD	Chemical vapour deposition
Nd: YAG	Neodymium doped Yttrium Aluminum Garnet
RBM	Radial breathing mode
TEM	Transmission electron microscopy
SEM	Scanning electron microscopy
VRH	Variable range hopping
MR	Magneto-resistance
R-T	Resistance against Temperature
I-V	Current against Voltage
FL	Fermi Liquid
CB	Coulomb blockade
Ni-SWNT	Nickel incorporated single walled carbon nanotubes
DMF	Dimethyl formamide
e-e	electron-electron
p-p	peak to peak

1 Introduction

1.1 Current research direction

There are a number of innovations attributed to CNT research. De Volder and co-workers [**1**] state that "In 2006 the winning tour de France bicycle was made from a CNT composite frame. In 2008 antifouling CNT paint was developed to coat the hull of a ship to prevent the build-up of deposits, in 2009 printed CNT transistors on a polymer film were produced, in 2011 a CNT based electrostatic discharge (ESD) shield was used in a space craft." In addition supercapacitors, water filters, wind turbine blades, nonvolatile random access memory devices and many CNT incorporated devices have been fabricated [**2**,**3**].

During the last ten years carbon nanotube (CNT) related industrial activity has developed significantly. Since 2006, wide-reaching CNT production capabilities have improved by at least a factor of 10 and are projected to reach billion sensor networks by 2020 [**4**]. Reports from the International Technology Roadmap for Semiconductors advocate that CNTs could substitute the existing microelectronic interconnects (Cu, Si and GaAs), due to their low scattering, high current-carrying capacity, and resistance to electro-migration [**5**]. After the first CNT transistor in 1998 [**6**], milestones include the first SWNT tunneling FET with a sub threshold swing of < 60 mV decade^{-1} in 2004 [**7**,**8**] and CNT-based radios in 2007 [**9**]. In 2012, SWNT FETs with sub-10 nm channel lengths showed a normalized current density (2.41 mA mm^{-1} at 0.5 V), which is greater than those obtained for silicon devices [**10**].

1.2 Background

The electronic properties of a system are strongly dependent on its dimensionality. With the ongoing advances in nanotechnology it has become possible to fabricate and study low dimensional systems where the electrons are strongly confined. Studies on such systems have yielded new and interesting results which have

contributed to the wide body of knowledge in the field of nanotechnology [**1**,**11**]. Since their discovery [**12**], CNTs have been regarded as potential quantum wires [**13**] where electrons propagate long distances through discrete electron states. The realization of single molecule devices initially proved challenging due to difficulty of making contacts. Continual advances in the field of nanotechnology have however presented ways of dealing with this problem [**14**,**15**,**16**,**17**]. The ultimate accomplishment in device miniaturization would be the fabrication of functional devices based on individual molecules. In multi walled carbon nanotubes which consist of a varying number of tubes the electronic properties have been shown to vary from tube to tube [**18**] and to be dominated by localization and disorder [**19**]. However SWNTs are promising candidates for individual molecule devices as they provide highly tuneable systems which allow for the study of the effects in many-electron systems [**20**].

Amongst all the nanostructured materials SWNTs are presently considered by some to be the most exciting and promising [**21**,**22**]. They incite a huge significance owing to their exceptional one dimensional atomic structure giving rise to outstanding mechanical, electrical and chemical properties. Moreover SWNTs have the highest geometric anisotropy factors amongst the low dimensional materials known [**17**].

The exceptional properties of SWNTs are not only a result of their extraordinary tubular structure, but also the fact that they are nearly free from any structural defects [**12**,**23**]. Their electronic properties are strongly dependent on the zero bandgap graphene structure since a nanotube is essentially a wrapped up graphene sheet [**24**,**25**,**23**]. The elementary properties of these graphene tubules depend on their chirality and the diameter [**26**]. However, to date the synthesis and isolation of SWNTs with desired chirality is not known [**27**,**28**]. Consequently, numerous efforts have been made to separate SWNTs by their conductivity i.e. semiconducting from metallic disregarding the chirality.

Electronic transport measurements showed that metallic SWNTs exhibit exceptional coherence lengths and that the presence of defects and disorder do not alter the electronic transport significantly [**29**]. Electrons in such one-dimensional 1D system form a strongly correlated electron gas which can be modelled through the Tomonaga Luttinger liquid theory (TLL) [**30**] rather than by Landau's Fermi-liquid theory [**31**]. The TLL state reveals itself through interaction-dependent uncharacteristic exponents in the correlation functions, density of states and momentum distribution of the electrons [**32**,**33**,**34**]. The transport properties of 1D conductors through electrons confined to 1D are strongly transformed as adding an electron to the system requires changing the many body states of its collective excitations [**35**,**36**,**37**].

1.3 Aim and Objectives

The aim of this study was to investigate the electronic properties of SWNTs synthesized by laser ablation. Metallic single walled carbon nanotubes have been reported as capable high current carriers [**38**] and may be considered for high speed nanoscale electronic devices. In this study we aim to probe further TLL behaviour that has already been observed but not yet fully understood using low resistance devices made from high quality SWNT. We also aim to investigate the effect of different device geometries on the overall electronic properties of SWNT based devices.

This will be achieved by optimization of the laser ablation process to synthesize high quality SWNTs. The synthesized material will be characterized structurally to confirm the existence of the SWNTs and the quality of the material produced. Di-electrophoresis will be employed to fabricate two-terminal SWNT based devices and a mat will be pressed to fabricate a SWNT based four-terminal device. The electronic properties of the two

-terminal devices will be measured in the Agilent Semiconductor probe station and the four-terminal devices will characterised in the Cryogenic high field measurement system. The conduction mechanism of SWNT mats and aligned SWNTs will be presented and compared to conclude which device geometry would yield best result towards miniaturized device fabrication.

1.4 Motivation

Miniaturization is the backbone driving the current information revolution by providing devices with faster speed, lower energy consumption at a lower cost [**39**]. Up till now, semiconductor companies have depended on silicon chips, endeavouring to discover alternative methods to improve their efficiency, whilst decreasing their size. However miniaturization of silicon based transistors has become increasingly difficult due to the fact that the physics limit of the material is being approached. Scientists have discovered that this approach has limitations due to enhanced quantum leakages at reduced dimensions [**40**]. The prototypical electronic circuit, fabricated around a single atom [**41**] might possibly represent the future of semiconductors. Hence, of all the above mentioned applications the most lucrative is to use CNTs to replace the role of silicon in transistors.

Single walled carbon nanotubes (which can be conceptualized as a tube formed from wrapped sheet of graphene) possess exceptional mechanical and electronic properties stemming from the zero band gap semiconductor graphene structure. It has been reported experimentally that the electrical properties of SWNTs are comparable and may even be superior to the preeminent metals and semiconductors which are currently being used in the electronics industry [**38**]. Hence the study of their electronic properties is not only of academic interest but it is imperative in order to gain a comprehensive understanding of this material which has great potential in the nano-electronic industry.

High quality SWNTs are ideal for transistor fabrication due to their low electron scattering and their band gap, determined by the diameter and chiral angle.

Additionally, SWNTs are ideal for field effect transistor (FET) fabrication due to the extremely high carrier mobility [**38**] and ballistic transport [**42**].

1.5 Summary

The purpose of the study is to shed more light on the evolution of properties of SWNTs synthesized by laser ablation. Ideally the bulk properties of a system should give a concise idea of the individual tube properties. Hence we study the properties of a SWNT mat and individual SWNTs. The study is extended by investigating the properties of modified SWNTs. The study was broken down into different sections as outlined below.

Chapter 2 is focused on the literature review of the material being studied i.e. single walled carbon nanotubes, growth methods and their properties.

Chapter 3 describes the synthesis method beginning from basic principles of laser operation to the laser matter interaction up to the production of nanomaterial using this method. The laser ablation experimental setup is described and optimization of the process parameters to synthesis high quality SWNTs.

Chapter 4 is the characterization section. It describes the how the morphology of the SWNTs was characterized by Raman spectroscopy, Scanning and Transmission electron microscopy. Furthermore the fabrication of SWNT ropes two-terminal devices by di-electrophoresis is described and SWNT mat devices are described. Measurement techniques employed to investigate the electronic properties of these devices are also described.

In chapter 5 the results for process optimization and morphology studies of the synthesized SWNTs are presented. Then the study of electronic properties of the SWNT mats and metal incorporated SWNTs are also discussed.

Chapter 6 is a dedicated to the electronic transport properties of aligned pure SWNTs ropes. These experiments show evidence of Luttinger-liquid behavior, in

which the electron-electron interactions lead to a qualitatively different ground state than what would be expected with Fermi-liquid theory.

Finally Chapter 7 is the conclusion and recommendations of the work presented in this dissertation. The conduction mechanisms in the different geometries are compared and contrasted and recommendations based on the findings of this work are made towards device miniaturization.

2 Literature Review

2.1 Allotropes of carbon

Carbon is the sixth element in the periodic table with four valence electrons in the outer $2s^2$ $2p^2$ atomic orbitals. The energy difference within the valence band atomic orbitals is very small giving rise to hybridization. During hybridization different allotropes of carbon are formed and the versatility of carbon atom is revealed. The eminent crystal allotropes of carbon are CNTs (single and multi-walled), fullerenes, diamond and graphite. There are also amorphous allotropes namely coal, charcoal and lamp black. These materials are completely different in appearance, as well as their mechanical and electrical properties.

The carbon atom is the basic building block of all its allotropes. Graphene is a sheet of carbon atoms, assembled in a regular hexagonal array. Bilayer graphene is formed from the stacking of two layers of graphene and tri-layer graphene is formed by stacking three layers. Graphite is produced from the stacking from a multitude of graphene sheets. Wrapping the graphene sheet into a seamless less tube yields a single walled carbon nanotube. Theoretically these tubes are very thin, with a very small diameter and considerably long, thus representing one dimensional structure. The carbon nanotubes are found in three classes single (0.4-2 nm), double (1.1-3.5 nm) and multi-walled (2-100 nm) determined by the number of concentric cylinders within the formation. Fullerenes can be conceptualized as graphene sheet wrapped into a ball, also known as the "Bucky ball". Hence the graphene sp^2 is a flexible carbon system giving rise to many different materials with different and interesting properties as will be described in the following subsections.

2.1.1 Diamond

Diamond is one of the hardest and most precious minerals known to man. It is made purely from carbon atoms unless if it has been modified. It occurs naturally and it can be grown synthetically [**43**]. It captures a wide interest in industrial applications due to its hardness and gemological applications due to its high light dispersion property. In industry diamond is used for cutting, drilling, grinding and polishing.

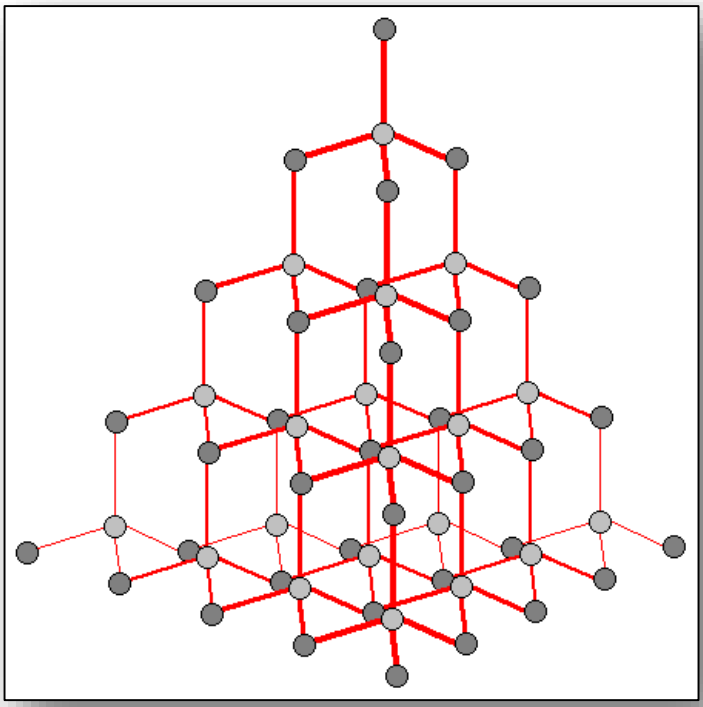

Figure 2.1: Crystal structure of diamond showing the sp^3 carbon-carbon bonding face centered cubic lattice forming a strong tetrahedral structure (Image adapted from www.substech.com).

The carbon atoms in diamond are arranged in a face-centered cubic (FCC) lattice, each carbon atom is bound to its four nearest neighbors by sp^3 bonds as shown in Figure 2.1, forming a strong tetrahedral structure (triangular prisms). It is the most stable form of solid carbon ever discovered, shiny and clear in appearance with a

very high melting point of 3 823 K. In diamond the valence electrons are localized between the atoms hence it does not conduct electricity.

2.1.2 Graphene

Graphene is a single layer of covalently bonded carbon atoms which was discovered in 2004 [**44**] and is known as "The mother of all graphitic sp^2 carbon materials" [**45**] since it can be wrapped into Bucky balls, rolled into nanotubes and layered into

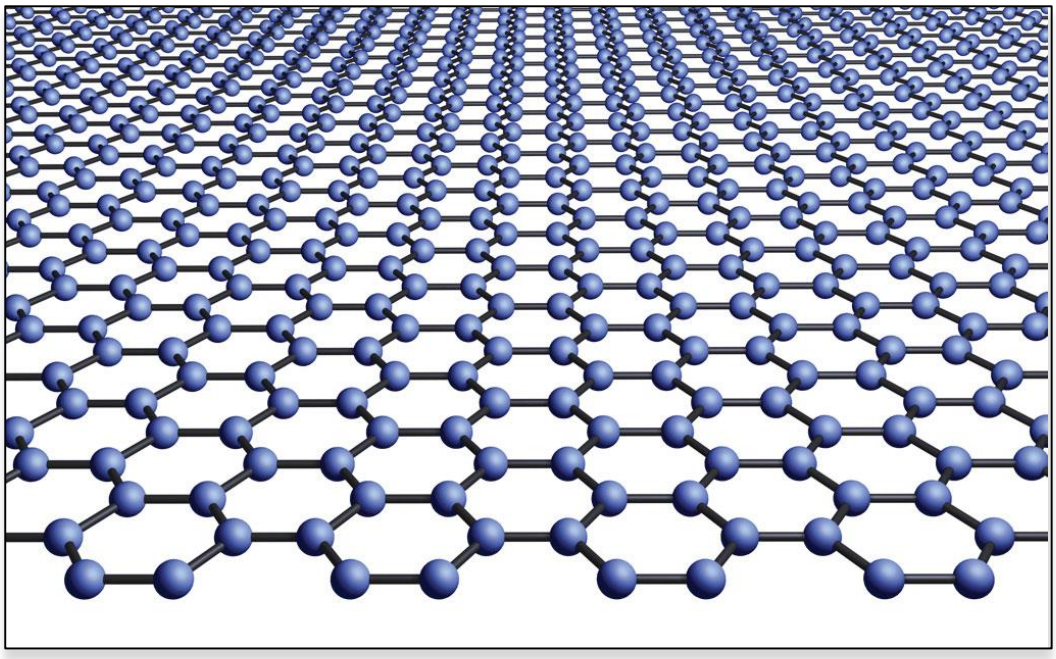

Figure 2.2: Crystal structure of graphene showing the two atom basis unit cell with one lattice point superimposed onto a hexagonal lattice [46**].**

graphite. In 2010 a Nobel Prize was awarded to scientists Andre Geim and Kostantin Novosolev, who in 2004 successfully isolated a single layer of graphene [**46**].

In graphene the electron orbitals in the valence band overlap resulting in a gapless conduction band. It can be prepared by exfoliation of graphite or grown synthetically by CVD. Graphene has become a highly pursued topic in the nanotechnology field due to its outstanding properties. It is very thin (one atom

thick), strong material, with a large surface area and ballistic conductor. It finds numerous applications for ultra-fast switching electronic devices, DNA sequencing [**47**,**48**].

2.1.3 Graphite

Graphite is a soft shiny dark material commonly used to make pencil leads. It can also be used in lubricants and during electrolysis to separate various compounds [**49**]. Graphite is sp^2 hybridized carbon, consisting of three covalent bonds between neighboring carbon atoms (0.14 nm apart) [**50**] forming layers with a bi-dimensional hexagonal crystal structure as shown in Figure 2.3.

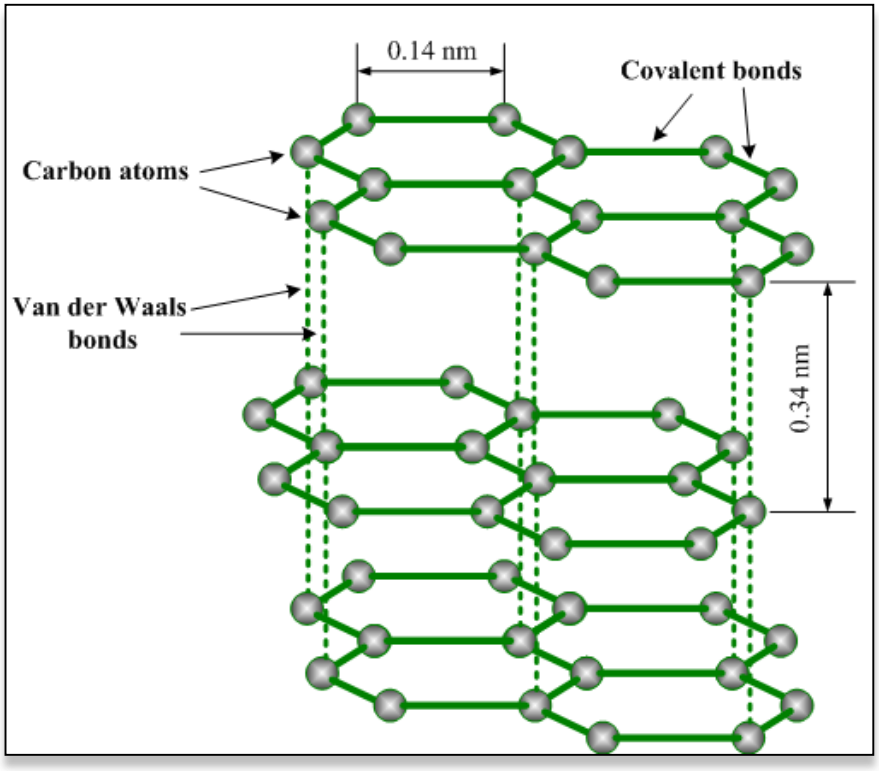

Figure 2.3: Crystal structure of graphite showing the stacking of sp2 bonded bi-dimensional structured graphene layers held together by weak van der Waals forces (Image adapted from (www.substech.com.)

As stated in section 2.1 carbon has 4 valence electrons hence graphite has a delocalized electron making graphite a conductor even though it is non-metal. The graphene layers are stacked at a distance 0.34 nm apart held by weak van der Waals force arising from dipole-dipole interaction resulting from correlated motion of electrons in different planes.

2.1.4 Fullerene

Graphite and diamond were the only allotropes of carbon known up to close the end of the 20th century. A new class of carbon was discovered in 1985 from small clusters of carbon during molecular beam experiments, called fullerenes [**51**]. Fullerenes are a hollow sphere comprising of pentagonal and hexagonal rings formed entirely from carbon atoms. The most famous fullerene is C_{60}, known also as “buckyball" as shown in Figure 2.4.

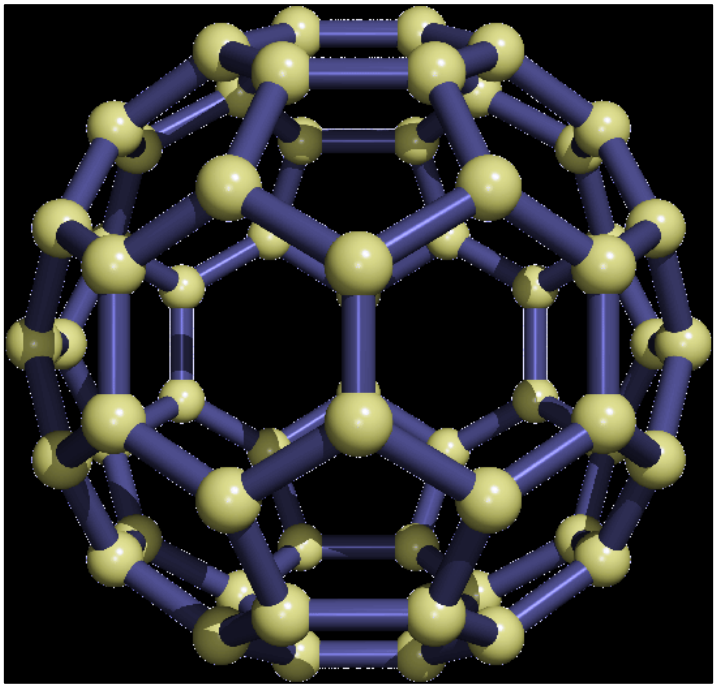

Figure 2.4: Buckminsterfullerene, C60, the third allotrope of carbon comprising of 12 pentagonal and 20 hexagonal rings (Image adapted from www.nanowerk.com)

Other relatively common clusters are C_{70}, C_{72}, C_{74}, C_{76}, C_{80}, C_{82} and C_{84} (plenty of others, higher or lower than C_{60}, exist too but less abundant in the experimentally produced mixture fullerene soot **[**52**]**. Each carbon on the sphere is surface is bonded to three carbon atoms hence it is sp^2 hybridized. The fullerene molecule became the third crystalline structure of carbon and is shown in Figure 2.4. Fullerenes find applications in artificial photosynthesis, nonlinear optics, cosmetics and biological applications **[**53**]**.

2.1.5 Carbon nanotubes

In 1991 Iijima [**12**] discovered a different class of fullerenes in the form nanometer sized cylindrical tubes called carbon nanotubes (CNTs). CNTs as described above can be envisaged as a sheet of graphene wrapped to form a seamless tube of a diameter 0.4 nm – 2 nm and a length of a few micrometers. The diameter of a nanotube is comparable to the size of a single molecule hence it is justifiable to classify it as a molecule. Due to their dimensions they exhibit properties of molecules, resulting in their unique physical and chemical properties. They have been an active area research for the past 20 years and currently scientists are moving from the laboratory to applications [**1**].

There are three different structural arrangements of CNTs depending on the number of concentric cylinders, i.e. single-walled carbon nanotubes (SWNT), double walled carbon nanotubes (DWNT) and multi walled carbon nanotubes (MWNT). Figure 2.5 shows the conceptual formation of nanotubes from a graphene sheet and the different classes of nanotubes. MWNTs and DWNTs were the first to be discovered in 1991 [**12**] in an arc discharge experiment whilst trying to synthesize Bucky balls and SWNTs were independently discovered later on in 1993 by Bethune and Iijima [**54**,**55**].

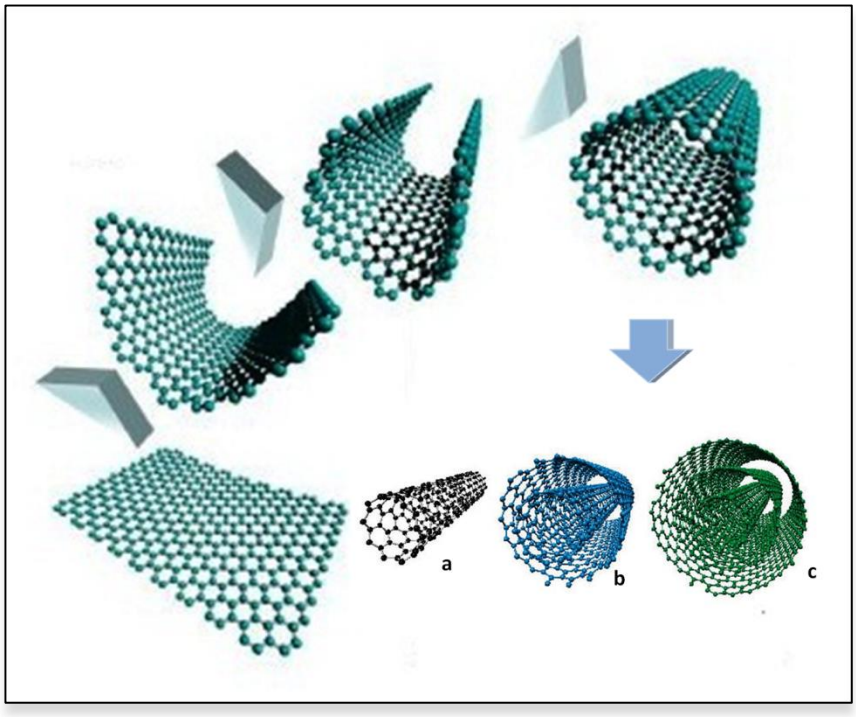

Figure 2.5: Illustration of the stepwise formation of a carbon nanotube from a graphene sheet. Three possible structures may result from the wrapping of a graphene sheet (a) single walled carbon nanotube (b) double walled carbon nanotube and (c) multi walled carbon nanotube.

2.2 Properties of single walled nanotubes

SWNTs conceptualized as a layer of graphene wrapped into a cylindrical tube have a high aspect ratio; diameters in the nanometer range, usually from 0.4 nm to 2nm and a length ranging from a few nanometers to hundreds of micrometers. Their properties are derived from the arrangement of its atoms. They are resistant to oxidation when exposed to air up to 1 023 K and 2 073 K in an inert atmosphere. The physical and chemical properties of SWNTs are consequently associated with their distinctive structural features [**56**].

2.2.1 Physical properties

Nanotubes can be classified into three groups; zigzag, armchair and chiral subject to the manner in which the graphene sheet is rolled up. A “de Heer” abacus shown in the Figure 2.6 below is a simple way of to visualize the formation.

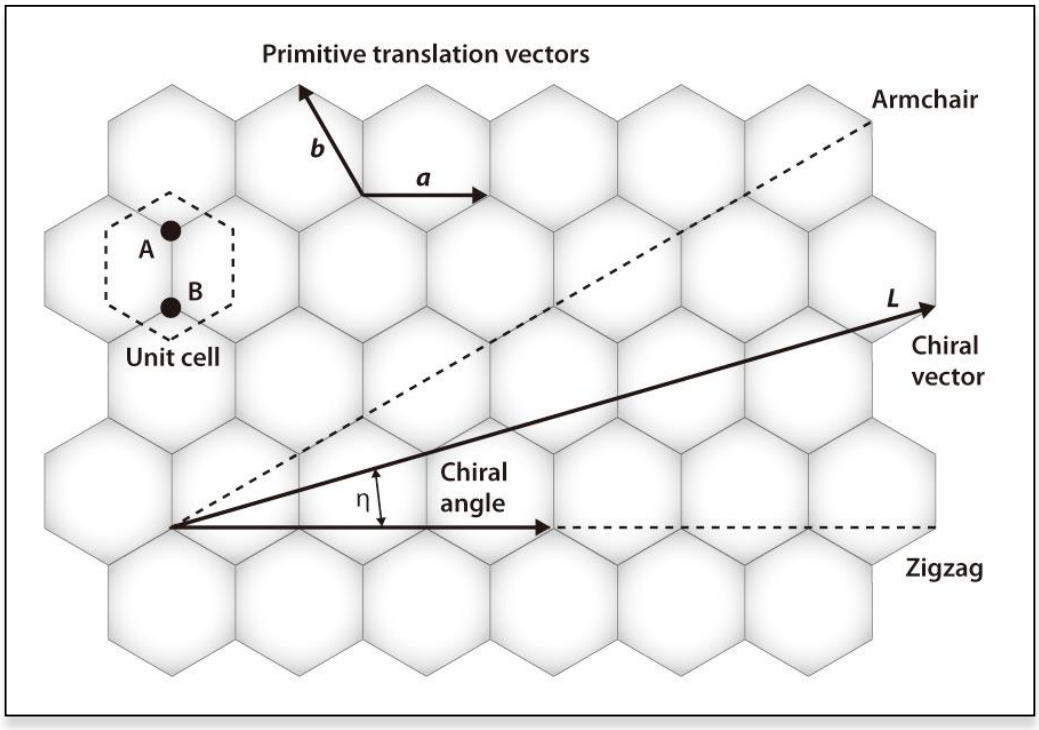

Figure 2.6: A "de Heer" abacus showing how the different chiralities denoted by (n, m) of nanotubes arise. The translation vectors $\vec{a}$ and $\vec{b}$ from the origin determine the value (n, m).

The nanotube can be classified into semiconducting or metallic depending on how the graphene sheet is wrapped. A single walled nanotube, for example, can be visualized as a rolled up sheet of graphene. Figure 2.5 illustrates the idea of rolling. MWNTs consist of a number of concentric graphite sheets rolled up to form a cylindrical tube of few nm in diameter. Due to their special structure, perfect carbon nanotubes are light, flexible, thermally stable and chemically inert. Furthermore SWNTs are found either as individual freestanding nanotubes or ropes consisting

of nanotubes entangled together which requires further processing to separate them [**57**]. A bundle if from an entangle network of ropes.

The chiral vector ($\vec{L}$) can be defined in terms of the lattice translation indices (n, m) and the basic vectors $\overrightarrow{a_1}$ and $\overrightarrow{a_2}$ of the hexagonal lattice (a layer of graphene sheet), that is:

$$\vec{L} = m\overrightarrow{a_1} + n\overrightarrow{a_2} \qquad \textbf{2.1}$$

The chiral vector ($\vec{L}$) is indicated in Figure 2.6, is defined as the line that is connecting two crystallographically equivalent sites from the origin to an arbitrary point on a two dimensional graphene structure.

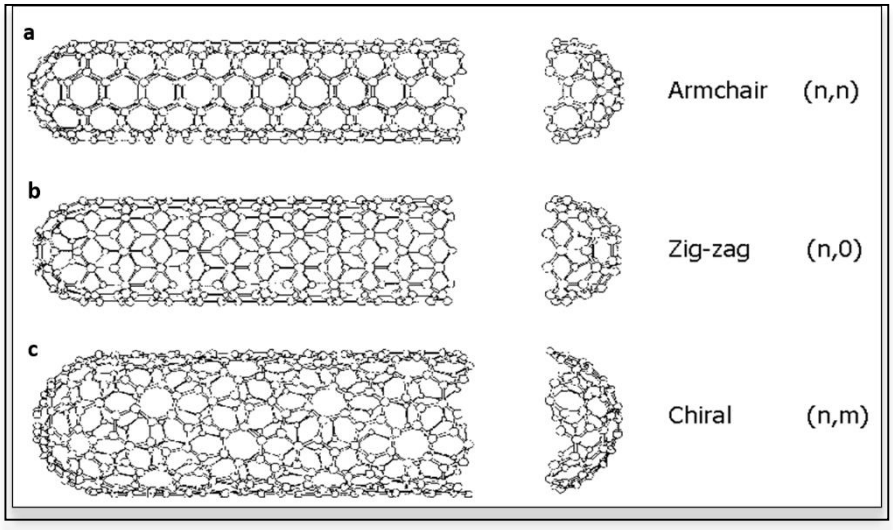

Figure 2.7: Models of different SWNTs (generated with Mathematica on the left, and taken from [23]. Schematic theoretical models of single walled carbon nanotubes, their hexagon orientations and cap structures (a) the armchair, (n,n), tube; (b) the zigzag, (n,0), tube; (c) the chiral, (2n,n), tube.

The description of CNT structures is related to the manner in which they are "rolled up" as in Figure 2.7. If after rolling, (0,0) and (5,0) overlap each other, then the tube thus formed is called a (5,0) zigzag nanotube. A zigzag nanotube would thus always be parallel to a (n,0) nanotube. An armchair nanotube can be formed by rolling such

that (0,0) and (n,n) overlap. The angle between a zigzag and armchair nanotube is always 30º. Any nanotube formed with chiral angle between 0º and 30º is called a chiral nanotube. This chirality of a nanotube determines its electronic properties. A nanotube is considered to be metallic if (n-m) is a multiple of 3. If it does not satisfy this condition then it is said to be semi-conducting. Thus the angle and the magnitude of the curl, plays a huge role in determining the chirality, and hence the electronic property. Figure 2.6 shows the chiralities of SWNTs (metallic and semi-conducting) which depend on the chiral vector $\vec{\boldsymbol{L}}$.

2.2.2 Electronic properties

The one dimensional tubular structure of SWNTs plays a crucial role in their electronic properties [**58**]. The tubes can be modeled as rolled up sheets of graphene where the "seam" gives rise to periodic boundary conditions that must now be imposed on the electronic wave function. This gives rise to one dimensional sub-bands with van Hove singularities in the density of states [**59**] complimented by different band structures for the metallic and semiconducting SWNTs as shown in Figure 2.8. The rolling up can be quantified by the chirality (helicity) vector$\vec{\boldsymbol{L}}$, which also determines the diameter and has been discussed previously. Pure graphene sheets have conduction and valance bands which touch at six points (K points) at the corner of the Brillioun zone. If the sub-band, introduced when rolling graphene to form SWNT, passes through the K point the formed nanotube will be metallic, otherwise the SWNT is semiconducting [**60**] as shown in Figure 2.8..This is a unique property that is not found in any other one-dimensional system. This means that for certain orientations of the honeycomb lattice with respect to the tube axis (chirality), some nanotubes are semiconducting and others are metallic. Metallic nanotubes possess a linear (massless) dispersion near the K point as shown in Figure 2.8, which makes them insensitive to any long range disorders such as

localized charges near the tube and hence their mean free paths become order of magnitude higher than semiconducting nanotubes.

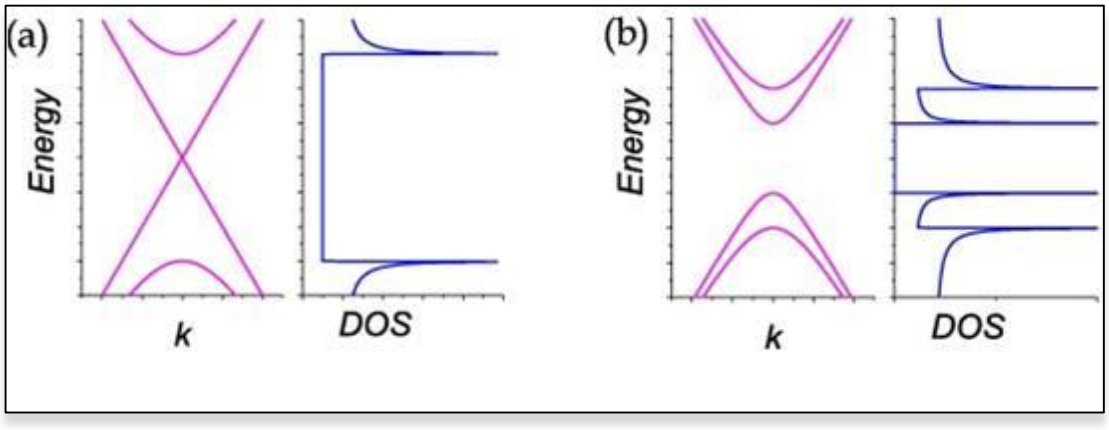

Figure 2.8: Sketch of band structure (left panel) and density of state (right panel) of a (a) metallic single-walled carbon nanotube and (b) semiconducting single-walled carbon nanotube.

In SWNT which are semiconducting it has been found that the band gap is inversely proportional to the tube diameter [**61**]. Electronic and optical properties of SWNT are substantially influenced by their environment [**62**] and electronic transition energies are typically found in the infrared and visible spectrum.

Electron scattering in SWNTs is reduced and this coupled with stability at high temperatures allows the nanotubes to support current densities as high as 109 A/cm^2, three orders of magnitude higher than Cu [**63**]. Nevertheless, structural defects may lead to quantum interference, localizing the charge carriers. Such localization results in increased resistivity in the material. Furthermore, carbon nanotubes may also exhibit positive or negative magneto resistance depending on the current, the temperature, and the field. Finally we find the thermal conductivity of SWNTs to be comparable to that of a single isolated graphene layer or high purity diamond (6000 $Wm^{-1}K^{-1}$). The large phonon free path in the material is ascribed to a combination of cylindrical topography and a reduced number of defects.

2.2.3 High frequency properties

The RF circuit properties of a 1D conductor were originally discussed by Wesstrom [**64**], who developed a transmission line description. However, at the time the technology to experimentally address the concepts was lacking. In a related set of papers, theoretical physicists considered the ac impedance of 1D conductors from the Luttinger liquid point of view for over a decade [**65**]. The concepts of transmission line theory were applied to develop a general RF circuit model for a single walled nanotube [**66**]. Salahuddin generalized this approach to include multi-mode quantum wires [**67**].

Theoretical models, benchmarking studies of the high-frequency potential have shown that bundles of SWNTs could outperform Cu provided SWNTs have resistance, inductance, and capacitance values at high frequencies that are consistent with predictions for ballistic conductors with quantized energy states [**67**]. At present, the propagation of high-frequency signals on high-performance modern integrated circuits is performed using copper interconnects. The bulk resistivity of copper is about 1.7 Ωm. However, as the copper feature size shrinks below 100 nm, surface scattering increases this resistivity. As we discussed above, CNTs have lower resistivity than copper, as they are not negatively impacted by surface scattering. The effective resistance and inductance of SWNT interconnects scale with the number of SWNTs in the bundle, that is, SWNTs in a bundle behave as resistors and inductors in parallel.

Validating the theoretical inductance and capacitance of SWNTs at high frequencies has proven to be extremely difficult. Measurements of the high-frequency impedance of bundles of SWNTs show that the bundle inductance scales with the number of individual SWNTs in the bundle, thereby effectively reducing the large kinetic inductance and resistance. This scaling behaviour makes SWNT bundles promising candidates for low-latency interconnects. The standard high-frequency characterization technique for Ultralarge-scale-integration (ULSI) circuit

interconnects is to measure the reflected and transmitted wave forms, typically represented by scattering or *S* parameters, from a two port network using a vector network analyser (VNA) and to de-embed the parasitic resistance, inductance, and capacitance of the interconnect electrode from the circuit element of interest. The S parameter of the CNT is obtained by applying a general de-embedding technique, [**68**] to remove the parasitic effects of the coplanar waveguide CPW and fit them to a physically meaningful equivalent circuit model. An intriguing sphere of application which has until recently received relatively minor attention is in the area of high speed (RF, microwave, mm-wave, and THz) electronics. The intrinsic speed limit of CNT devices can be very high, up to the THz range, so that on further reflection it seems potentially feasible to fabricate high speed devices and ultimately systems out of CNTs.

2.2.4 Magnetic properties

It has been demonstrated by experiment and theoretically that carbon based nano-materials are magnetic when there are no impurities present [**69**]. It is important to gain an understanding of the mechanism which brings about the magnetism to extend the technological applications of the material. A complete interpretation for the source of magnetism from experimental observations has not been provided to date. The bucky ball C_{60} has been reported to exhibit ferromagnetism which arising from the interaction of vacancy defects and sp^3 hybridization [**70**].

Localized states at the edges of zigzag SWNTs and graphite sheets are thought to induce magnetic polarization. It has been reported that due to vacancies the electronic structure of metallic SWNTs can change to semiconducting and vice-versa [**69**]. Ferro or ferrimagnetism has been reported for metallic SWNTs with vacancies, while semiconducting SWNTs with vacancies are antiferromagnetic. The magnetic properties of SWNTs are determined by the chirality, the arrangement

and concentration of the vacancy. The pure carbon nanotubes are well known to exhibit diamagnetic behavior [**71**].

2.3 Synthesis methods

CNTs can be produced using different methods. There are three main methods used namely arc discharge, chemical vapor deposition and laser ablation. CNTs were discovered during an arc discharge experiment and the other experiments were developed later. The common element in all these methods is the carbon feed stock and the presence of a metal catalyst for the synthesis of SWNTs and possibly the growth mechanism.

2.3.1 Growth mechanism

The growth mechanism of nanotubes is still being speculated about with two possible routes. The first mechanism known as “root growth” states that the catalyst acts as a root and the carbon atoms assemble to form a CNT on top. The second mechanism states that the catalyst acts as a growth center and the carbon atoms are adsorb from the surface and a CNT grows with the catalyst on top. These two mechanisms are illustrated on Figure 2.9. The mechanism however is expected to be same for all synthesis methods. The nature of the catalyst (floating or supported) should not affect the growth mechanism as well. MWNTs can be formed from a carbon source in the absence or presence of a catalyst whereas SWNTs only form when there is a catalyst.

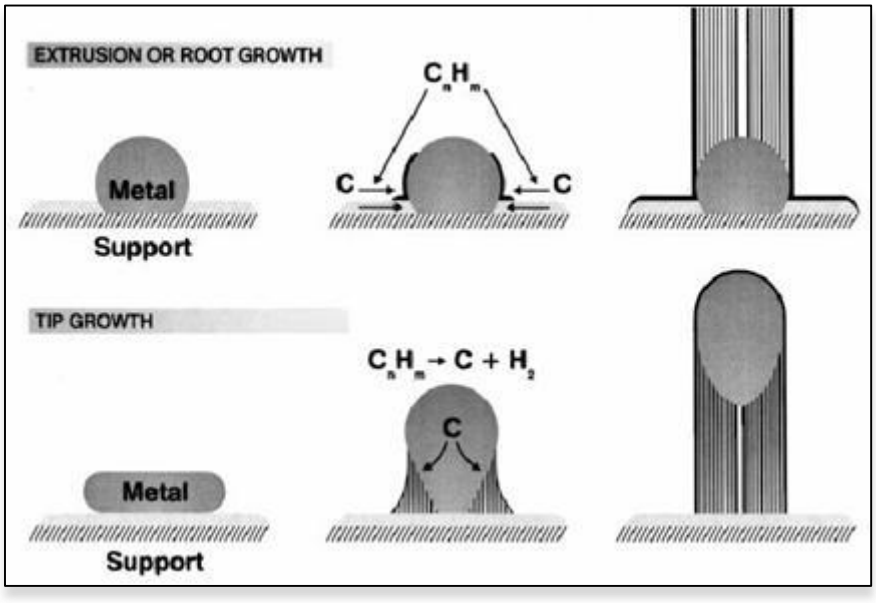

Figure 2.9: Illustration of possible CNT growth mechanisms, root growth and tip growth

2.3.2 Arc discharge

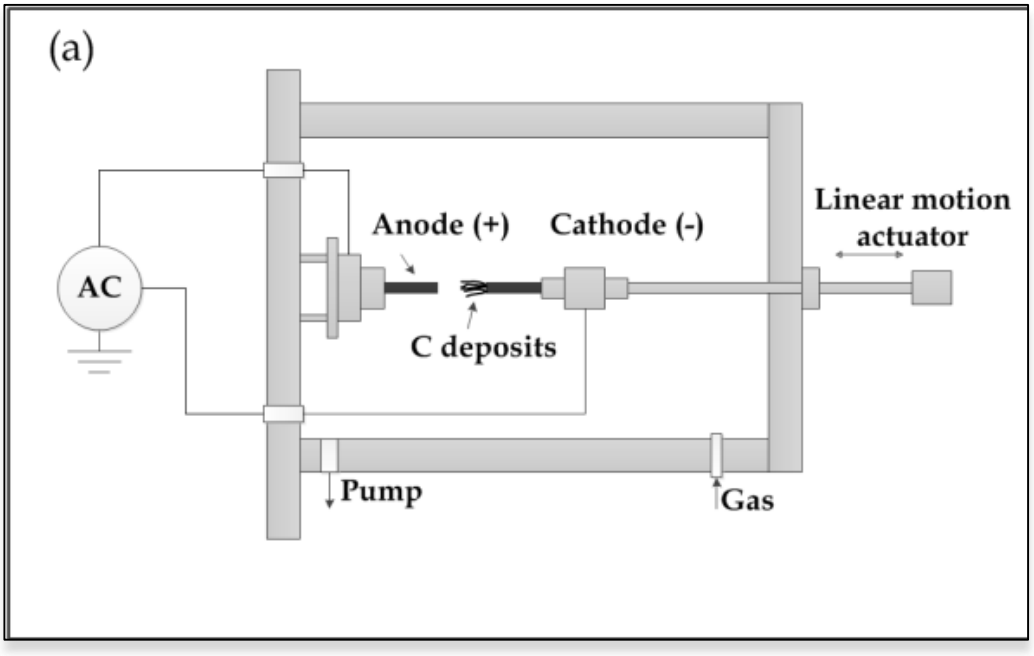

Figure 2.10: Arc discharge experimental setup

Figure 2.10 shows a schematic illustration of arc-discharge setup showing the anode and cathode graphite electrodes. An inert gas line and pump are connected to evacuate the apparatus. The arc discharge method was initially used to produce C_{60}bucky balls [**72**] when CNTs were discovered. In this method the carbon feedstock is in the form of two high purity graphite electrodes immersed in an inert gas. The nanotubes are produced by applying an arc voltage (DC) between these two electrodes at high temperatures. Both single walled and multi walled carbon nanotubes can be produced depending on whether the graphite rods contain a metal catalyst or not. However this method yields a soot containing nanotubes along with large amounts of impurities including carbonaceous material and remnants of the catalyst if was present in the initial target. To produce good quality nanotubes the cathode must be efficiently cooled [**12**,**73**,**74**].

2.3.3 Chemical Vapour Deposition

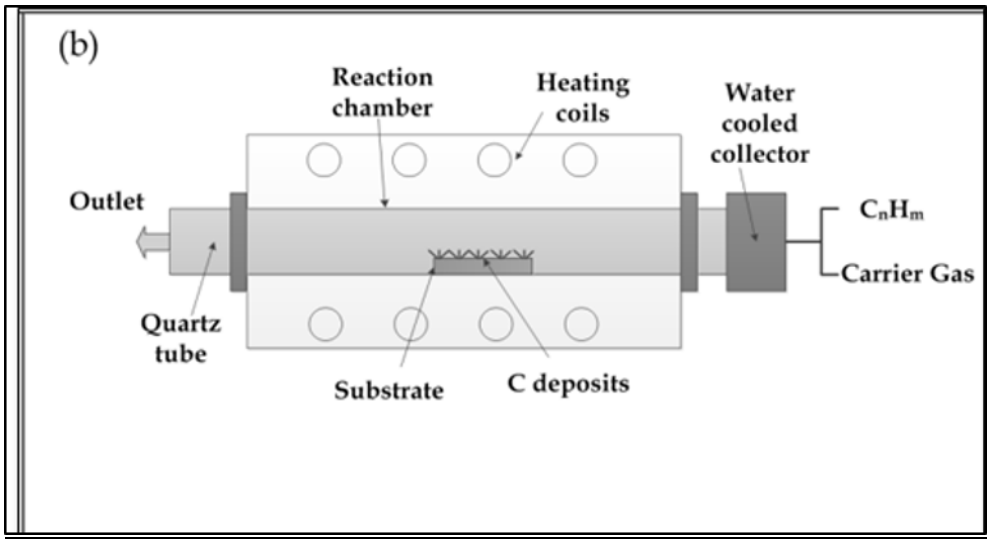

Figure 2.11: Chemical vapor deposition experimental set up

The chemical deposition method (CVD) is another method used to synthesize CNTs using catalysis, illustrated in Figure 2.11 In this method the CNTs are grown by the decomposition of gaseous hydrocarbon precursors in the presence of a transition

metal catalyst at temperatures ranging from 300 - 1000 K. A supported and floating catalyst can be used. During CVD the hydrocarbon gas dissociates into individual carbon atoms which precipitate onto nanosized catalyst particles. Use of catalysis reduces the need for high temperatures. Hydrogen from the decomposition process and the carrier gas contribute to the activation and reactivation of the catalytic surface. The CVD method has a better CNT yield and is potentially scalable to commercial manufacturing [**75**].

2.3.4 Laser ablation

Smalley *et al* [**76**] were the first to synthesize CNTs through pulsed ablation in 1995. In this method a high power laser pulse is used to ablate and vaporize a graphite target containing metal catalyst at high temperatures. The method can be used to produce single and multi-walled CNTs. SWNTS are produced when a small percentage of metal catalyst is added to the graphite target and at target without catalyst would result in the production of MWNT, analogous to the arc discharge method. The yield and quality of the CNTs produced depends on the process parameters to be discussed in details in the chapters that follow.

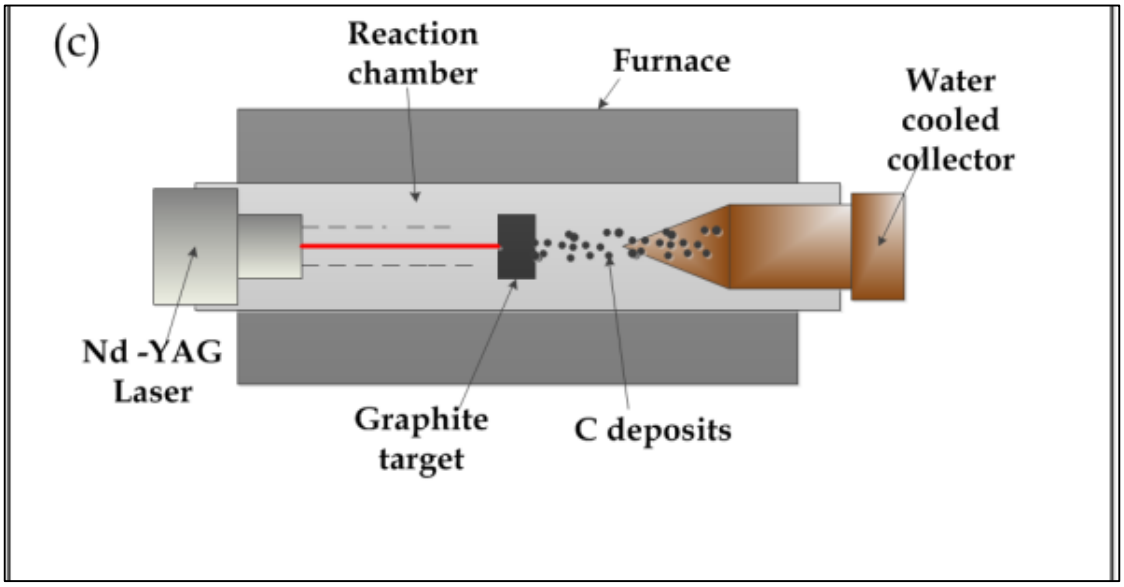

Figure 2.12: Laser ablation experimental setup

Figure 2.12 is a schematic diagram of the laser ablation set up. The laser beam is focused onto the graphite targets in a quartz tube furnace at high temperature, 1200 °C with argon flowing. Carbon atoms are ablated from the surface of the target by the laser beam and vaporize into an atomic plume. The argon gas carries the plume to the cooler region downstream where they condense onto the walls of the flow tubes to form CNTs or a cooled collector as shown in Figure 2.12. The SWNTs produced from this method have a narrow diameter distribution and they of superior quality compared to the other two methods.

2.4 Di-electrophoresis of single-walled carbon nanotubes

The term di-electrophoresis (DEP) is derived from the Greek word *phorein* which means the ability of an uncharged particle to move when subjected to an electric field depending on its dielectric constant. Di-electrophoresis is the process whereby an electric dipole moment is induced in a particle in the presence of an electric field resulting in a di-electrophoretic force which draws the particle into the region of greatest field strength and aligns the particles in the electric field. All particles exhibit di-electrophoretic activity in the presence of electric fields. However, the strength of

the force depends strongly on the medium and particles' electrical properties, shape and size, as well as on the frequency of the electric field. Consequently, fields of a particular frequency can manipulate particles with great selectivity. In CNT research, DEP was originally introduced as a tool to assemble and contact individual or bundled SWNTs on predefined electrode structures [**77**,**78**,**79**]. The di-electrophoretic force is sensitive to the relative dielectric constant of particles and as semiconducting and metallic nanotubes have different dielectric constants, metallic tubes are preferentially aligned while the resulting modification in the electric field repels semiconducting tubes [**80**,**81**].

The controlled assembly and contacting of the nanotubes is a prerequisite for an elective device fabrication. In this study deposition and alignment of metallic SWNT onto electrodes is accomplished via the alternating field controlled di-electrophoresis method. This is the main method for device fabrication which is also used as a separation technique i.e. separation of nanotubes with different chiralities. Research has shown that this method can be used for deposition and alignment of SWNT for several devices and can be used for the wafer scale fabrication of SWNT based integrated circuits [**82**].

2.5 Electronic transport in low dimensional structures

2.5.1 Ballistic transport in metallic SWNT

Ballistic transport occurs when the length of an electrical conductor is less than the mean free path of the charge carriers' i.e.

$$L \ll l_m \qquad \textbf{2.2}$$

Where L is the length of the conducting channel and l_m is the mean free path.
This implies that an electron traverses the length of the channel without momentum relaxation. In this regime the electrical resistivity due to scattering by the atoms and

or impurities in the system is negligible. Ballistic transport cannot be described by Ohm's law. Ohmic law applies only to classical incoherent regime where both phase coherence length and mean free-path are greatly less than sample length. The conductance is expected to increase infinitely as the width of the channel is increased as stated by the Ohmic scaling relationship,

$$G = \frac{\sigma W}{l} \qquad \textbf{2.3}$$

Where with α is the material system's conductivity and W the channel width.

To fully understand the transport characteristics of carbon nanotubes, we start with the Landauer formula, which states that the conductance of a quasi-1D system is given by:

$$\mathbf{G} = \frac{4e^2}{h}\sum_i \int_{-\infty}^{\infty} \frac{df\left[\frac{E-E_f}{k_B T}\right]}{dE}\tau_i(E_f)dE \qquad \textbf{2.4}$$

where $\tau_i(E_f)$ is the transmission of the *i*th 1D sub-band state at the Fermi energy and d*f*/d*E* is the energy derivative of the Fermi function. Conductance is thus a measure of the transmission of electrons through the entire device at the Fermi energy, broadened by the finite thermal width of the Fermi function.

Ballistic conductance, evidence of quantization due to finite tube length, has been reported for nanotubes by Bockrath *et al.* [**35**]. A carbon nanotube may have many 1D subbands described by discrete angular momenta and axial wave vectors [**83**]. Universal conductance fluctuations in electrical transport experiments have been observed in SWNT mesoscopic systems. These fluctuations originate from coherence effects for electronic wave functions of the plasmons, and thus the phase-coherence length L_Φ needs be larger than the momentum relaxation length $\mathbf{L}_m$. The fluctuations are dominant when electrical transport is in weak localization regime.

$$L_\Phi > l_c \qquad \textbf{2.5}$$

Where $l_c = M$ x l_m, M is the number of conduction channels and l_m is the momentum relaxation length or mean free path. The change in conductance for weakly localized samples is equivalent to the fundamental conductance irrespective of M.

Metallic SWNT are expected to be ballistic conductor at room temperature [**35**]. In a ballistic 1D quantum wire the electron motion in one direction is free and continuous and quantized in the other two directions. Hence the charge carriers propagate freely in a defect free, narrow metallic SWNT with no scattering. Each conduction channel would contribute

$$\mathbf{G_0} = \frac{e^2}{h} \approx \mathbf{12.9\ k\Omega} \qquad \mathbf{2.6}$$

to the total conductance $G(E)$, where e is the electronic charge and h is Planck's constant. According to the Landauer formula the conductance $G(E)$ of a SWNT is independent of its diameter and length given by;

$$\mathbf{G}\ (\boldsymbol{E}) = \frac{2e^2}{h} \boldsymbol{N}\ (\boldsymbol{E}) \qquad \mathbf{2.7}$$

Where $N(E)$ is energy, dependent on the number of available quantum channels. A metallic nanotube has two quantum channels at the Fermi energy $E=0$ also known as the charge neutrality point resulting in G_0 is equal to a conductance of $2G_0$. At higher energies more channels become available for charge carrier propagation which results in an increase in conductance. Hence the ideal case of a 1D system representing CNTs would conduct current ballistically with no dissipation of heat. Consequently metallic SWNTs provides a very good test bed for the TLL theory as it represents a nearly perfect 1D conductor with a very long mean free path.

However experimentally is has been revealed that in such a system as discussed above the conductivity saturates at a fixed value. Electrons are injected into 1D modes of the channel at the chemical potential of their respective source electrodes. The absence of scattering inside a ballistic channel produces no voltage drop along the channel length, and hence the chemical potentials for charge carriers moving to

the left and right are constant across the channel. Accordingly, the entire voltage drop associated with the quantization of conductance occurs at the leads such that we may define a contact resistance of *12.9 kΩ* per mode, consistent with experimental observations [**13**].

2.5.2 The Coulomb Blockade effect in SWNT

The ropes of SWNTs connected by two leads can be envisaged as an electron island connected to non-interacting Fermi liquid points. The central idea for Coulomb blockade is that the thermal and potential energy applied to the island are less than the energy required to add an electron into the island [**84**] i.e. the coulomb charging energy given by,

$$\mathbf{E_c} = \frac{\mathbf{e^2}}{\mathbf{2C}} \qquad \mathbf{2.8}$$

where *C* is the island capacitance. At low thermal energies lower than the charging energy,

$$\boldsymbol{K_B T \ll E_c} \qquad \mathbf{2.9}$$

The propagation of charge through the island is blocked at low biases

$$\boldsymbol{eV = E_c} \qquad \mathbf{2.10}$$

The smaller the conductor is the more significant the effect of the Coulomb interactions is due to the limited degrees of freedom. Due to the significance of coulomb interactions at 1D there is an excitation of collective degrees of freedom which hinders the charge transfer at low energies. Coulomb Blockade in low excitation energy regime can be overcome by introducing a gate voltage. The gate voltage is a massive electrode that is electrically disconnected from the island and the Fermi electrodes but can excite charges to flow in the island even at low thermal energies. At thermal energies, $k_B T \ll E_c$ lower than the charging energy transport

is usually dominated by Coulomb blockade. There can be a periodic lifting of the Coulomb blockade resulting in Coulomb oscillations with a period, $\frac{e}{C}$ of conductance as a function of gate voltage. At higher thermal energies beyond the Coulomb blockade regime power law behavior is observed for the temperature and bias dependence of the conductance.

For metallic SWNT, the differential conductivity decreases but reaches a finite value at zero bias, consistent with TLL signature This behavior indicates a conductivity which is independent of bias voltage, i.e., constant. We note that this behavior may be interpreted as the existence of Coulomb blockade at low biases, necessitating a reasonably high voltage to trigger plasmon propagation.

Hence to realize the Coulomb blockade three conditions must be met: (1) The bias voltage must be lower than ratio of elementary charge to the self-capacitance of the island: $V_{bias} < e/C;$ (2). The total thermal energy in the source contact and the island, i.e. k_BT should be less charging energy: $k_BT < e^2/C,$ if it's more the electron will propagate through the SWNT by thermal excitation; and (3) The resistance due to tunneling R_t should be greater than h/e^2 as derived from Heisenberg's uncertainty principle [**85**].

2.6 DC conductivity in carbon nanotubes

Theoretical band structure calculations confirm a metallic conduction behavior for some CNT configurations. Bulk SWNTs samples are usually mats containing CNT ropes indiscriminately oriented, where each rope is made up of parallel individual CNTs. Fischer *et al* [**86**] established a consistent metallic signature for the conductivity of SWNT mats at room temperature, i.e. an inverse relationship between conductivity and temperature. Further he found that at temperatures below 200 K the dependence of the conductivity on the temperature regressed to non-metallic signature. Figure 2.13 shows the measurements carried out by different

authors [**87**] for the conductivity of SWNT mats showing the metal insulator transition (turning point on the curve) at different temperatures for different configurations of SWNTs.

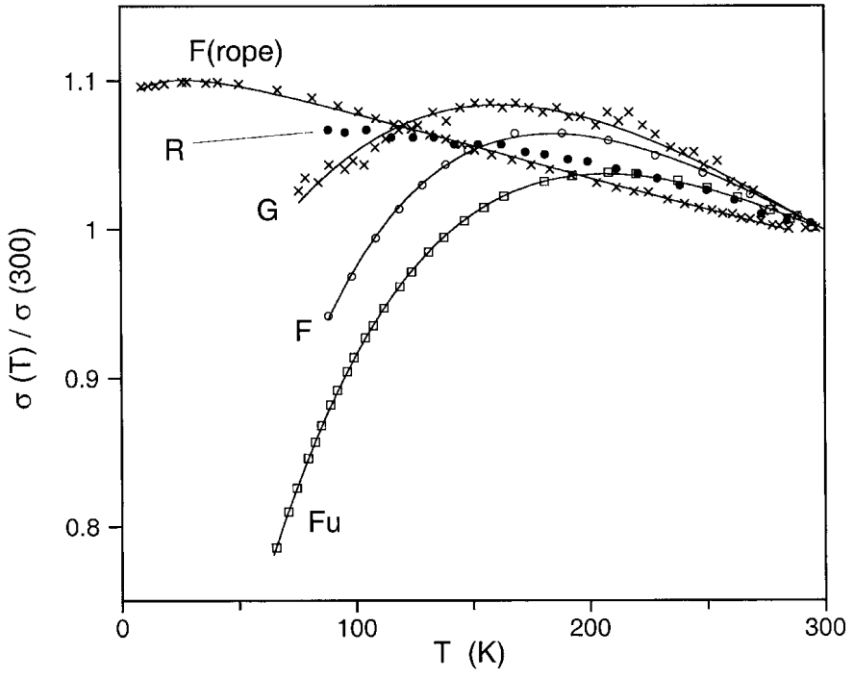

Figure 2.13: The normalized conductivity of SWNT mats and a rope showing a metal-insulator transition occurring at different temperatures, from Fischer *et al* (1997) (F), Rinzler *et al* (1998) (R), Grigorian *et al* (1998) (G), and Fuhrer *et al* (1999) (Fu).

2.7 Magneto conductivity

Disordered metals are more sensitive to the effects of magnetic fields than crystals, especially at low temperatures as the magnetic field tends to break weak localization found in these materials. Quantum interference enhances the probability for backscattering in a disordered system in the metallic regime. This is the precursor of strong electron localization and has therefore become known as weak localization. Weak localization depends crucially on phase coherence of the electronic wave function and constructive interference is destroyed when an

external magnetic field alters the relative phase of the scattered wave. A magnetic field therefore tends to increase conductivity.

Conductivity σ is expected to have a complicated dependence on B proportional to B^2 in the low field limit (0-6 T) and $B^{1/2}$ at higher fields (greater than 6 T) [**88**]. Such behavior has been observed experimentally, however, negative magneto-conductivity has also been found in some cases [**89**]. Current models explaining magneto-conductivity derive from weak localization and electron-electron interactions in disordered materials. Variable range hopping (VRH) could account for large positive magneto-conductivity as spin-flips increase the likelihood of finding an electron in a desired conductive state [**90**]. Negative magneto-conductivity may be due to spin- orbit coupling or quantum interference effects.

3 Synthesis of Single WalledCarbon Nanotubes by LaserAblation

3.1 Laser development and operation principles

3.1.1 Laser development

Briefly, a laser is described as a device that amplifies light waves (optical amplifier). The acronym **LASER** in fact stands for Light Amplification by Stimulated Emission of Radiation. A laser produces light rays of a particular wavelength in a constricted single color beam. The main difference between a laser and other radiators like the sun or a light bulb is that they emit light with different wavelengths in all directions. A laser emits light (electromagnetic radiation) through a process of optical amplification based on stimulated emission of photons. The laser light emitted is noteworthy for its high degree of spatial and temporal coherence. The most outstanding feature of lasers is the ability it possesses to precisely deliver large quantities of energy into very small areas of a material.

Albert Einstein established the theoretical foundations for the laser and the maser in the paper *Zur Quanterntheorie der Strahlung* (on the Quantum theory of Radiation) [**91**], from Max Planck's laws, theoretically based on Einstein's probability coefficients for the absorption, spontaneous and stimulated emission for electromagnetic radiation in 1917. In 1960 the first working laser termed "a solution looking for a problem" was reported. It was Theodore Main who made this accomplishment based on the ruby crystal at the Hughes research laboratory in California [**92**]. To date lasers have been produced using different materials such as gases, solid-state crystals material and diode laser fabricated from semiconducting material [**93**,**94**,**95**]. Lasers are now able to produce much higher energies than

before. In the following sections the basic of how a laser operates leading to material synthesis will be described.

3.1.2 Design of a laser

The design of a laser is based on four main components; the gain medium, energy source to provide an excitation mechanism, a provision for optical feedback and an output coupler [**96**] as illustrated in Figure 3.1.

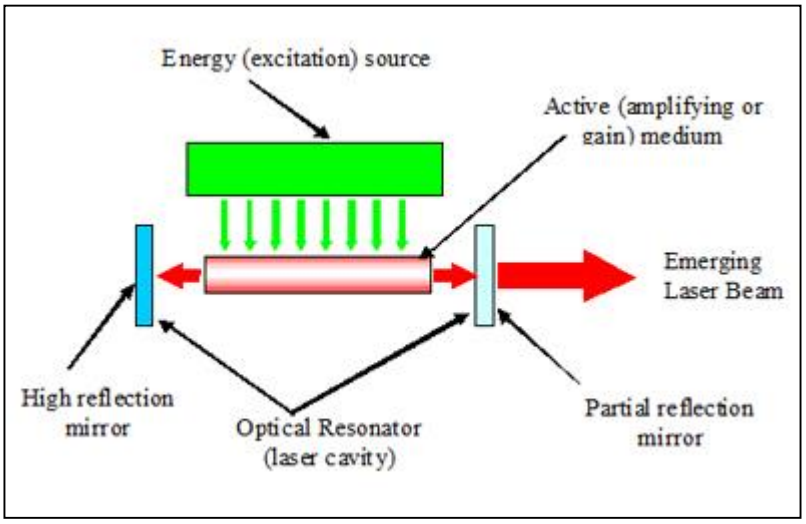

Figure 3.1: Laser design diagram showing the basic components that make a laser; the excitation mechanism, gain medium, optical resonator and an output coupler

The gain medium which can be either gas solid or semiconductor should be a material that allows for the amplification of light. Light from an excitation mechanism consisting of a power supply, flash lamp or another laser, passes through the gain medium where it is amplified through a process called pumping, Mirrors provide the optical feedback mechanism and output is via an output coupler. The continuous emission of laser light is a repetition of the processes described above. Most practical laser setup consists of additional components to improve the properties of the light produced such as wavelength and the shape of the beam.

3.1.3 Principle of operation

As defined above LASER stands for light amplification by stimulated emission of radiation. This definition is a brief outline the principle of operation of the laser. So to understand the principle of operation one needs to appreciate the terms in the acronym. Light contains photons possessing a dual nature i.e. particle like- and wave-like. The energy of each photon is dependent on its frequency given by;

$$\mathbf{E} = \boldsymbol{h\nu} \qquad \mathbf{3.1}$$

Where v is the frequency of the light and h is Planck's constant. The frequency is related to the wavelength by

$$\mathbf{c} = \mathbf{v\lambda} \qquad \mathbf{3.2}$$

Where λ is the wavelength and c is the speed of light in a vacuum. Using this relationship the energy of a photon can be related to its wavelength.

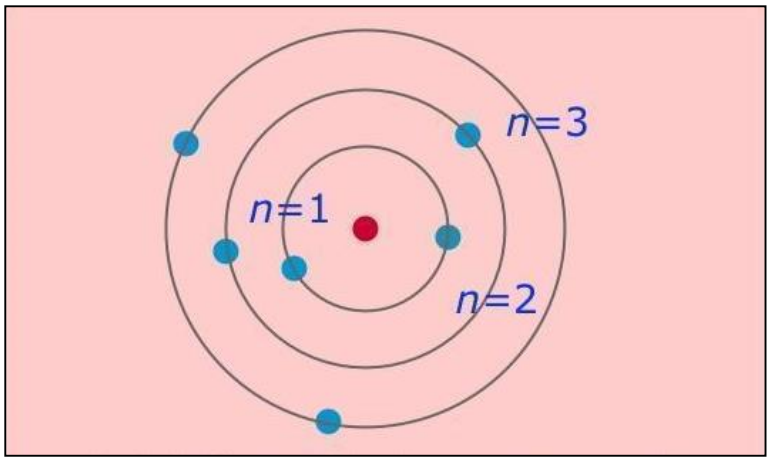

Figure 3.2: Bohr Model of the atom (adapted from http://chemwiki.ucdavis.edu/) showing that electrons can only occupy orbitals with integer values, n =1,2,3 etc

The Bohr model shown in Figure 3.2 is used to understand the concept of stimulated emission. In this model the energy of electrons orbiting the nucleus are expected to be larger for atoms further from the nucleus compared to those closer. In 1913 Niels Bohr proposed that quantum mechanical effects force electrons to acquire distinct

position within the orbitals called quantum states [**97**]. Hence, electrons can only be found in number of fixed orbits corresponding to particular energy levels of an atom.

Transitions within discrete energy levels n=1, 2, 3, occurs when an electron absorbs energy from photon or phonon. When an electron absorbs energy due to an external electro-magnetic field to move to higher energy level the process is called absorption (Figure.3.3). An electron which moves from a lower energy level to higher energy level is said to in an excited state. Decay refers to the process when it moves from a high energy level to a lower energy level. If it decays to a lower energy state unperturbed the process is called spontaneous emission (Figure 3.3) as the case for fluorescence and thermal emission. Stimulated emission (Figure 3.3) results from a transition from a higher energy level to a lower energy level due to an external magnetic field. These mechanisms are illustrated below in Figure 3.3.

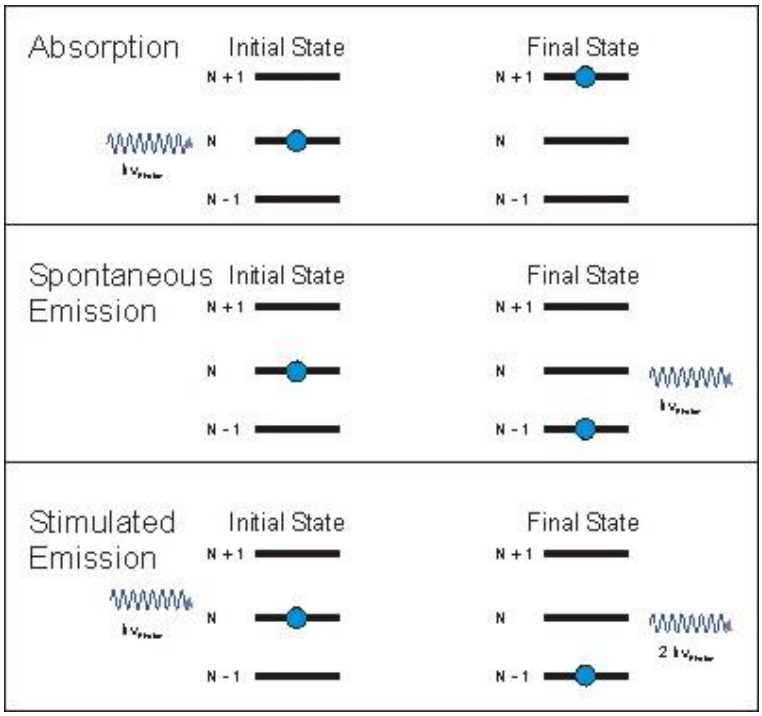

Figure 3.3: Illustration of absorption, spontaneous emission and stimulated emission

Laser light is produced through the processes described above. The external source is used to excite the gain medium. As mentioned in section 3.1.3 the gain medium should be a material which allows for the amplification of light. Hence the energy supplied by the excitation mechanism excites the atoms in the gain medium. The beam is amplified by a process of stimulated emission as described above. Population inversion is achieved when the number of excited states in the gain medium exceeds the number of electrons in a lower energy level, i.e. the stimulated emission exceeds the absorption of the gain medium. This is actually the process of light amplification.

3.2 Laser matter interaction

The use of the laser for material processing is based on the controlled interaction of the laser with matter. The light emitted by the laser should be fined tuned so as deliver the energy that will alter the material to the desired properties. When light is incident onto the surface of a solid material components of the light are reflected depending on the index of refraction of the material and the environment, the polarization and incidence angle of the light and the rest is absorbed by the material. This is expressed through the Fresnel equation as;

$$\boldsymbol{R = R_s = R_p \left(\frac{n_1 - n_2}{n_1 + n_2}\right)} \qquad \textbf{3.3}$$

Where R is the reflectivity of the material, R_s and R_p are the reflection coefficients of s and p polarized light, n_1 and n_2 are the indices of refraction of environment and material respectively. The absorption coefficient $\propto$ of the material determines the decay rate of the light intensity given by the Beer-Lambert law as;

$$\boldsymbol{I(z) = I_o e^{-\propto z}} \qquad \textbf{3.4}$$

where I_0 the intensity at the surface after considering reflection loss and z is the depth of the beam.

3.3 Laser ablation - experimental

In this study the aim is to investigate the electronic properties of a 1D system in the form of SWNTs. This is achieved through the synthesis of high quality single walled nanotubes by pulsed laser ablation. The nanotube ropes are isolated and connected to external leads in order to investigate their electrical properties. This section will explain how the SWNT were synthesized and treated.

Pulsed laser ablation, utilizing short and intense pulses to vaporize a solid target, provides high quality material and the desired flexibility. The ablated solid target is composed of an atomic plume subsequently condenses to form nanotubes. Briefly, the nanotubes are produced when a high energy laser beam is incident onto a graphite target thereby removing material on the surface due to heat induced vaporization. The detailed synthesis will be discussed further in this chapter.

3.3.1 Overview of experimental setup

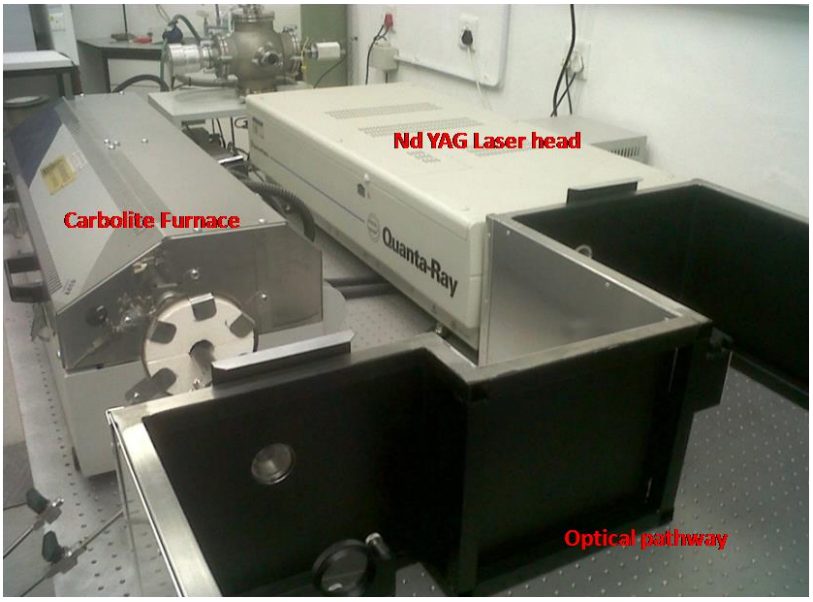

Figure 3.4: Overview of experimental setup showing Nd:YAG laser, optical pathway and furnace.

The experimental setup consists of three interconnected subsections specifically for the production of nanotubes. These are the laser source and optics; furnace, and

flow control. The laser source is a Quanta-Ray PRO-270 Nd:YAG (neodymium doped yttrium aluminum garnet), producing a 532 nm (green light) laser beam. A Carbolite electric furnace is used as the growth chamber where a 25 mm quartz tube holding the target is placed. The flow of gas in the experiment is controlled by a Vacutec MKS mass flow controller interfaced with a turbo pump. The laser head and furnace are aligned parallel on an optical board such that the laser beam is steered to trace a rectangular pathway during ablation.

3.3.2 Description of the Nd:YAG laser components

The Nd:YAG laser includes of the following components; laser head, power supply and analog controller. Control of the beam position is through a desktop computer interfaced with LabVIEW software program and an analog controller providing control of the motorized mirrors. The laser head is a pulsed 1064 nm oscillator and amplifier system coupled to a harmonic generator (HG) stage, to generate 532, 355 or 266 nm output wavelengths. Dichroic mirrors are used to reflect the desired output simultaneously transmitting the undesired harmonics into a beam dump. The laser operates on a dual ac/dc power, supply for the flash lamp supply that provides energy to operate the laser and PFN simmer power supply that stores the power required to flash the lamps. A chiller is connected for cooling the power supply. An analog controller also connected remotely to the power supply of the laser employs conventional analog knobs and switches to set and control the system parameters.

The Quanta- Ray PRO series Nd:YAG pulsed laser head provides compensation for thermally-induced birefringence in the YAG rod, providing uniform beam. The fold and dichroic mirrors provides beam pointing performance (+/-50 μrad). It also has diffused gold reflectors for optimum mode control over time. The Quanta Ray laser has an internal maintenance through the use of nitrogen purged beam tubes. The sealed beam greatly extends the longevity of optical coatings by shielding all optics from contamination. Optics resistant to damage from high laser pulses is employed

in the optical path setup. It also has a single rod and amplifier which facilitate high repetition rates. The output frequency can be varied by 10% of the nominal frequency.

Table 3.1: Nd:YAG PRO 270 expected performance

Wavelength (nm)	Repetition rate(Hz)	Energy (mJ)	Pulse width(ns)	Short term energy stability	Long term power drift
1064	10	1750	8 to 12	2 s	Less 3%
532	10	860	10	2 s	Less 5%

The fundamental wavelength 1064 nm, is dumped and the source is frequency doubled to output the second harmonic i.e. 532 nm at 10 Hz at a pulse duration of 10 ns .Newport mirrors are used to steer the beam to the target surface. The beam path is guided by two mirrors, an aperture, and lens The first mirror is placed at an angle so that it reflects the beam though an aperture which is used to adjust the beam size. The beam is directed to a second motorized mirror. This mirror plays a crucial role in beam positioning. Since it is motorized it can be adjusted so as to raise or lower the beam path, relative to the target position, depending on its positioning angle. The beam was directed through a lens which determines the target position in the synthesis chamber. In this study a 1 m focal length lens was used to focus the beam to a concentrated spot size of 3 mm with a full power fluence of 860 mJ.

3.3.3 Beam alignment procedure

The laser source is positioned parallel to the furnace where the target is located, nevertheless, exact calibration alignment must still be performed. Below is a step-wise description of the beam alignment procedure;

1. Turn chiller on.

2. Turn nitrogen purge on to around 5.5 sccm on the needle valve on the cylinder.
3. Turn laser power source on.
4. Allow 20 minutes for laser coils to warm up.
5. Switch laser in the long pulse mode to low energy oscillation ~100 mJ.
6. Locate the beam position using ZAP – IT ^{TM} laser alignment paper.
7. The first mirror can be adjusted in the x – and y – direction so as to adjust the position of the beam.
8. The aperture can be adjusted so at to alter the size of the beam.
9. The motorized mirror can be adjusted manually and through a LabVIEW program for beam positioning.
10. Once the beam has been located its position can be fine-tuned through the LabVIEW program which facilitates manipulation in the x- and y- direction.

3.4 Synthesis of single walled carbon nanotubes

3.4.1 Target preparation

The target, in the form of a graphite-metal composite pellet, was prepared in the laboratory. Catalyst particles need to be incorporated in the target for the production of SWNT, hence, the inclusion in the graphite powder of a small percentage of Nickel and Cobalt. The graphite powder, ground from a graphite rod and sieved through a 150 μm pore sized sieve was mixed with Nickel; 2 μm and Cobalt 9 μm sized powder and compacted into cylindrical targets in a steel mold using a cold press. The powder to be pressed is mixed such that it has the following atomic composition; 98%C; 1% Ni; 1%Co (atomic percentage) which gives high quality SWNT as has been reported in literature [**98**]. The powders are mixed meticulously by grinding in a crucible. The graphite-metal powder is the mixed with a binder, namely polyvinyl alcohol (PVA) dissolved in ethanol, which is to be removed at a

later stage. To make a pellet the powder is loaded into a 15mm steel mould and cold pressed at 10 tonnes for 15 min. The pellet is unloaded carefully from the back end of the mould and placed in an evacuated tube in an oven. The oven temperature is ramped at 100 K steps from room temperature to 1173 K in an argon atmosphere to remove the binder and other impurities that have been absorbed during the preparation. This is a very important step as the target retains its shape as it is annealed. The resulting target is 15 mm in diameter and the thickness depends on the amount of powder loaded into the mould. It is kept in dry conditions prior to ablation so as to maintain purity. The critical parameters in target preparation are amount of catalyst, force applied during pressing and annealing temperature. It was also found that the metal used as catalyst has an effect on the yield. The process of annealing has to be done stepwise at 100 K, for 60 minute intervals up to 1373 K, otherwise the pellet crumbles due to thermal shock. The annealing is done in the presence of Argon so that the target is not oxidized at higher temperatures. The pellet remains in the oven for 6 hours after 1373 K has been reached then the oven is switched off and it is allowed to cool down naturally. After all these steps the target is ready for ablation. The design and composition of the target is important for the production of good quality CNTs. It has been found that the composition and conditions used above are the optimal.

Table 3.2: Target Pressing conditions

Atomic Composition	Force applied	Diameter	Heat treatment temperature
C98%: Ni1%; Co1%	10 tonnes	15 mm	1373 K

3.4.2 Synthesis process

The experimental setup is shown in Figure 3.4. Pulsed laser ablation is the preferred method of synthesis due to its precise stoichiometric transfer between target and product under the right conditions. Optimization of the synthesis process is necessary for good quality nanotubes. In optimization the process parameters that had to be varied were target composition, chamber pressure, temperature, gas flow rate, target position, beam focus, target surface area scanned by beam, pulse energy. The Table 3.3 gives the process parameters used in this study.

Table 3.3: Optimized process parameters

Process parameter	Set point
Target composition	98%C;1%Ni;1%Co
Gas Pressure	600 mbar
Furnace Temperature	1373 K
Carrier Gas	Argon
Gas flow rate	200 sccm
Flow tube inner diameter	25 mm
Beam focus	Slightly defocussed
Beam spot size when defocused	4.6 mm
Beam spot size when focused	3 mm
Laser pulse frequency	10 Hz
Pulse duration	10 ns
Pulse energy during synthesis	860 mJ

To synthesis SWNT the graphite-metal composite target supported by a steel rod is positioned in a flow tube placed in the furnace at a distance determined by the 1 m lens used for focusing the beam. The tube is sealed off using O-rings and clamps. The laser beam is switched on and focused on the target surface at a spot size of 3 mm. A rotary pump is used to pump the flow tube vacuum down to a base pressure of 2 mbar. Argon gas is flowed in through a mass an MKS flow controller at 200 sccm. The beam on the target surface is slightly unfocussed to ablate a larger area and to increase the yield of SWNTs [**99**]. When a stable pressure and temperature are attained the laser beam is switched on to full oscillation and amplification.

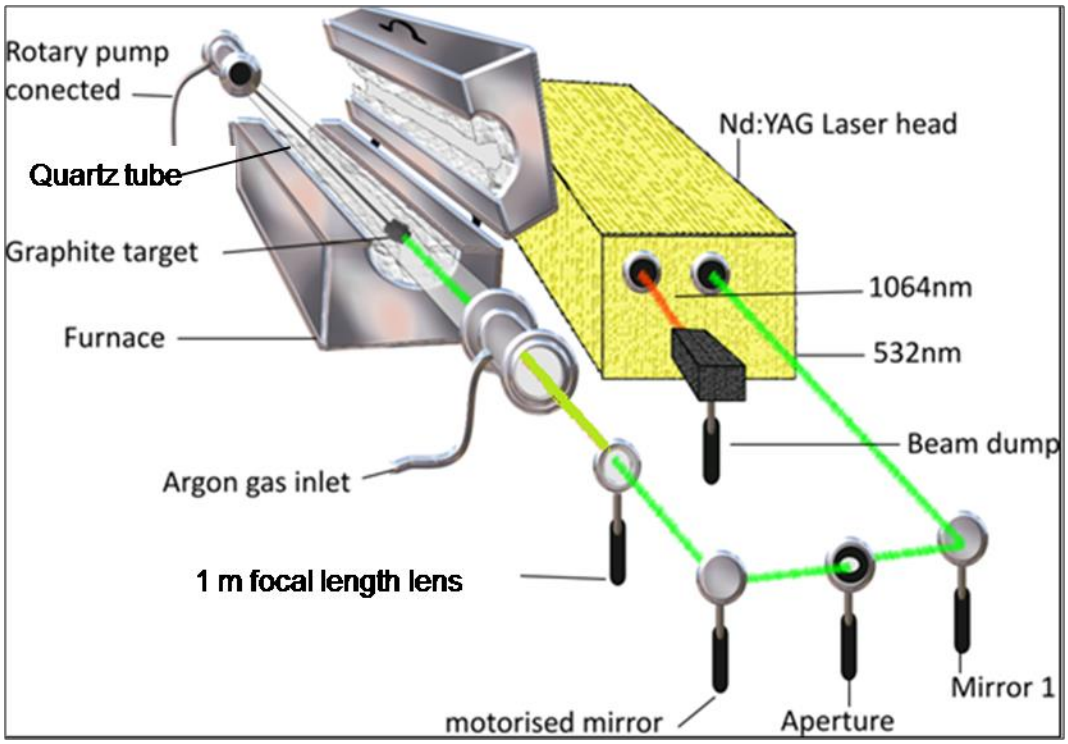

Figure 3.5: Detailed experimental setup of laser ablation synthesis of SWNTs.

An atomic plume which consists of ionized and neutral carbon atoms and metallic particles by vaporization of the target due to the incident high energy laser beam and high temperature in the furnace is formed at the point of ablation. The argon gas is used as a carrier gas for the plume as well as a buffer. The atomic sized

particles are carried from the hot zone to the cooler region where they condense and the metallic particles act as growth centers for the formation SWNT which are deposited on the walls of the flow tube. The beam is allowed to raster the target for 10 minutes before it is switched off. The furnace undergoes natural cooling before the argon gas is turned off at approximately 300 K to avoid oxidation of the synthesized material and residual graphite target. The SWNTs which look like sticky black soot are scrapped off from inner walls of the tube.

3.4.3 Purification of single walled nanotubes

The as synthesized SWNTs from the laser ablation technique are known to have a few defects. However it contains a metal catalyst particle which has an effect on the overall electronic properties on the material and amorphous carbon. They can be purified through a wet purification method by using nitric acid treatment. The raw SWNTs are refluxed in 2 M nitric acid for 30 h at 400 K. The nitric acid is removed through successive ultracentrifugation steps, rinsing in distilled water after each cycle to purify. The sample is dried and heated in open air at 400 ^{o}C to remove any remnants. Highly purified nanotubes are obtained from this procedure as seen on the TEM imaging (Figure 5.9). This method is also used for the purification of nanotubes synthesized by other methods with a slight difference of acid concentration though. It has been found that longer exposure of nanotubes to the acid treatment or a higher concentration would cause functionalization of the walls. On the other hand if the nanotubes are under exposed to the acid or concentration is too low the carbonaceous material will not be effectively removed.

3.5 Summary

Pulsed laser ablation is the chosen synthesis method for this work due to its flexibility affording an opportunity to tune the process parameters in order to achieve the desired results. The method allows for the modification of the physical

and chemical properties of the graphite over multiple length scales to produce far much better material i.e. carbon nanotubes which possess superior electrical and mechanical properties after optimization.

4 Experimental

4.1 Introduction

In this study the aim is to investigate the electronic properties of a 1D system represented by SWNTs. This is achieved through the synthesizing of high quality single walled nanotubes by laser ablation. The individual SWNTs agglomerate into crystalline ropes that aggregate into tangled networks due to strong van der Waals attraction [**57**]. The nanotube ropes are isolated and connected to external leads in order to investigate their electrical properties. This section will explain how the synthesized SWNT were characterised structurally, how devices were fabricated and finally how the electronic transport measurements were carried out.

4.2 Structural characterization

4.2.1 Raman analysis

Raman spectroscopy has been used to for structural characterization of SWNTs because it is one of the most sensitive characterization tools for these nanostructures. This technique is a powerful tool for understanding the behavior of electrons and phonons in a material. The three dominant Raman features are the radial breathing mode (RBM) at low frequencies, the tangential (G band) multi feature at higher frequencies and the disorder-induced D band [**45**].

The RBM frequency is unique to SWNTs and is not observed in other carbon materials. It results from the coherent vibrations of carbon atoms of each nanotube in the radial direction and normally appears at frequencies between 120 and 250 cm^{-1}. The RBM frequency is inversely proportional to the diameter, hence the

chirality an isolated SWNT can be assigned when considering the resonance condition. The diameter-dependent RBMs of carbon nanotubes give detailed information about the one-dimensional confinement of their electronic structure, thus giving information about the unusually strong Coulomb coupling between optically generated electrons and holes (i.e., about excitons). The Raman spectra can determine the tube diameter with 1 Angstrom accuracy. The frequencies of the RBMs are resonant with electronic transitions in the nanotubes. This means that for a given sample of bundled SWNTs, RBM peak frequencies and intensities will be different for different excitation energies. RBM line widths also depend on other factors such as temperature dependent effects, tube-tube interactions, deformations and defects, electronic structure and curvature [**100**].

The G band in SWNTs is composed basically of two stronger peaks (G^+ and G^-) related to the circumferential (TO) and axial (LO) atomic vibrations [85]. The splitting for these two peaks depends on the tube-wall curvature, so that the G has a small frequency dependence on d_t that can be used to corroborate the diameter information obtained from the RBM. The most important characteristic is the strong line shape dependence of the G^- peak on the tube type and doping. While in semiconducting tubes the circumferential TO mode has a lower frequency when compared to the axial LO mode, the opposite happens in metallic tubes. The LO mode in metallic tubes shows up at a much lower frequency than the G^-peak (TO) from semiconducting tubes, and it exhibits a broad and asymmetric (Fano-like) line shape.

The D band has been widely used for the characterization of carbons samples. It is observed when there is symmetry breaking on the hexagonal sp^2-bonding lattices. The observation of a D band in the Raman spectra is, therefore, related to either the presence of defects in the tube walls (e.g., vacancies,7-5 pairs (Stone Wales defects), dopants or just the presence of tube ends) or to the presence of amorphous-carbon material in the sample. As a metric for the internal calibration procedure, the

analysis is typically made based on the I_D/I_G intensity ratio. The more defective the material, the larger and broader the D band, and the larger the I_D/I_G ratio.

The as-synthesized material is black soot consisting of a film of SWNT bundles which is placed on a silicon substrate for analysis. A Bruker Raman spectroscopy instrument is used calibrated with a silicon wafer. The Raman analysis is done at room temperature and ambient pressure. For all-purpose Raman analysis, all samples were subjected to 532 nm (green) excitation lasers. The laser power at the sample for each of the lasers was adjusted to about 1.5 mW. To take spectra the sample of the as synthesized material is loaded on a glass substrate holder and the spectra is taken at different magnifications. Low laser powers 1– 10 mW and high integration times are preferred so as not to damage the sample.

For detailed analysis a Jobin-Yvon T64000 VIS-NIR-IR Raman spectrometer equipped with an Olympus BX41 microscope was used. The system was equipped with two detectors; a CCD detector for use with lasers excitations in the UV-VIS-NIR range and a liquid nitrogen cooled InGaAs detector which is designed for use with IR lasers. The system was optimized to deliver 514.5 nm (green) and 647 nm (red) laser lines.

Due to the varying texture there was need for multiple spot analysis, it was found the best approach was prepare a thin film of the as-prepared material on the microscope slide. To do this, 5 mg of the as-prepared material was ultra-sonicated for 2 minutes in 5 ml of laboratory grade ethanol using a Heilscher UP400S horn sonicator which was operated at 100 W electrical power. A few drops of this solution was placed on a glass slide and allowed to dry to produce a thin film. The Raman was done only on the as prepared material.

4.2.2 Electron Microscopy

Scanning electron microscopy is used to confirm the presence of nanotubes on the as prepared material and for surface morphological analysis on the purified SWNTs.

In this study a JEOL 7001-F scanning electron microscope SEM is used. The acceleration voltage can be varied from 1 kV to 15 kV. The resolution of the secondary electron image (SEI) is 1 nm at acceleration voltage of 15 kV and 2 nm at an acceleration voltage of 1 kV. Magnification is from 25 times to 1 200 000 times. The microscope operates at a vacuum of 10^{-8} Pa to produce high resolution images even at low acceleration voltages. Nanomanipulators are coupled to the microscope in order to extend the functionalities of the instrument. They are useful during device fabrication to manipulate the position of the nanomaterial.

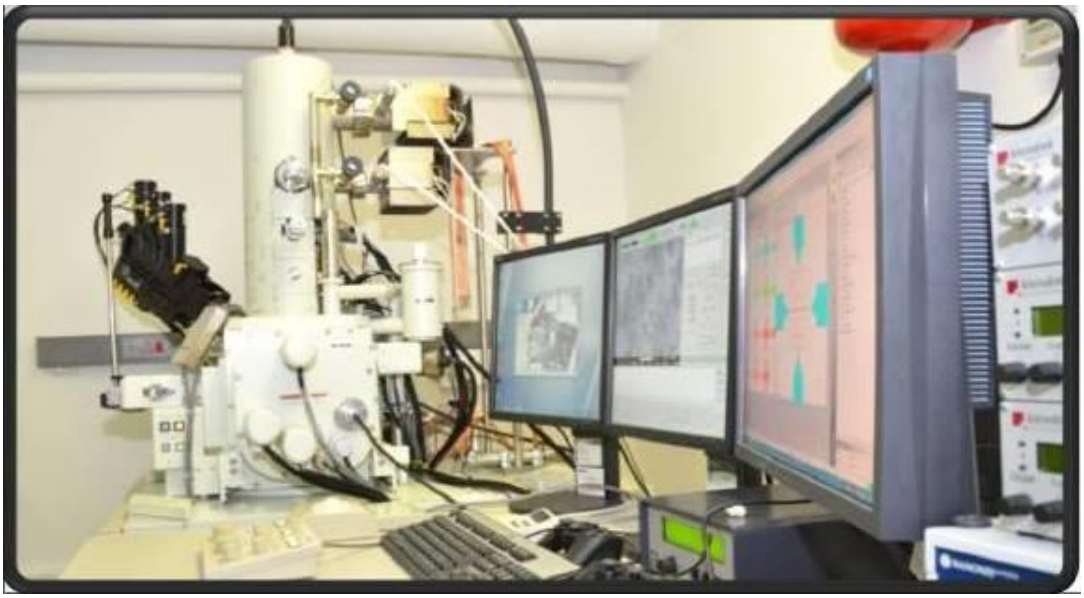

Figure 4.1: JEOL 7001F SEM facility used structural characterization of the synthesis. It is coupled to a gas injection system and nano-manipulators operated with at acceleration voltage up to 15 kV.

Two different solvents are used for sample preparation. Firstly the nanotubes were dispersed in methanol for general viewing, and then DMF which is compatible for DEP was used at later stage for dispersing the nanotubes in for SEM imaging. The CNTs in solvent are ultra-sonicated for 12 h to disperse the particles thoroughly. The sample is deposited on a vacuum compatible flat substrate that is also

conductive to prevent charging. A silicon (110) wafer is used. The sample is allowed to dry before mounting it on the SEM substrate holder. For silicon wafer, acceleration voltage of 2 kV, spot size 3 mm, and secondary electron imaging (SEI) mode is most compatible. The imaging is done in a high vacuum of 9 x 10^{-5} Pa, as gas molecules interfere with the electron beam and with the emitted secondary back scattered electrons used for imaging. A low vacuum would be trade-off for resolution. Carbon tape is used to fix the substrate on the holder and also to minimize charging effects. Close inspection by SEM of the soot like material produced by laser ablation reveals felt-like material at high magnification of 30 000 times which consists of long tangled fibres. The fibres are bundles SWNT as shown in next chapter.

For an internal structural analysis of the purified SWNTs the FEI Spirit Transmission Electron Microscope (TEM) is used. The microscope operates at a transmission voltage of 120 kV and standard magnification from 10^6 times. In this technique a beam of electrons interacts with an ultra-thin specimen to generate an image. To make a sample for TEM analysis, 1 mg of the purified SWNT is dispersed in 10 ml methanol and ultra-sonicated for 12 h. One drop of the specimen is deposited on a holey carbon film supported by a TEM copper grid. The copper grid is allowed to dry in air before is it loaded onto the TEM single tilt substrate holder. The substrate holder is inserted into the microscope through an inlet provided taking care not to crash the vacuum. When the vacuum is below 31 Torr the beam is switched on and the proper alignment procedure is carried out in order to obtain high quality images with the greatest amount of contrast between particles. The beam is aligned from the top to down. It is also important to use purified material for imaging in order to get clearer images of the material of interest as TEM imaging relies upon differences in electron density between the sample and the surrounding substrate - the presence of non-volatile organic molecules that are not removed under vacuum during sample preparation, or the presence of inorganic species that are collected while drying a sample the surroundings may reduce the

image quality. The sample need not be to dilute so as to make finding it on the copper grid effortless. After alignment the beam is focused on the specimen and zoomed in to capture detailed structural features of the CNTs. High resolution images were taken at magnification 97 000 times, beam spot size 4 mm which showed individual nanotube ropes at 20 nm resolution (Figure 5.9).

4.3 Low temperature transport measurements

4.3.1 Device fabrication by Di-electrophoresis

The purified nanotubes are dispersed in ACE gold line n,n dimethyl formamide (DMF). Studies have shown that in this solvent the dispersion of SWNT is stable and uniform due to the higher viscosity of DMF compared to other solvents. 1 mg of SWNT powder was added to 10 ml of DMF and sonicated thereafter for 4 h. The dispersion was subjected to further processing through centrifugation at 25000 rpm for 30 minutes. The resulting supernatant was decanted for the sediment of nanotubes which was subjected to the purification process once more. The process was repeated three times before finally dispersing the nanotubes in a solvent with a low concentration and purer SWNTs.

The patterned substrate is first cleaned using acetone, methanol and distilled water. It is placed in a beaker with the solvent and sonicated for five minutes in each solvent starting with the acetone, drying with nitrogen after each solvent. An optical microscope is used to select good microstructures before the alignment procedure as the patterning is not precise due to lift off errors. In this study bulk contacted devices are used, which means the nanotubes are suspended on top.

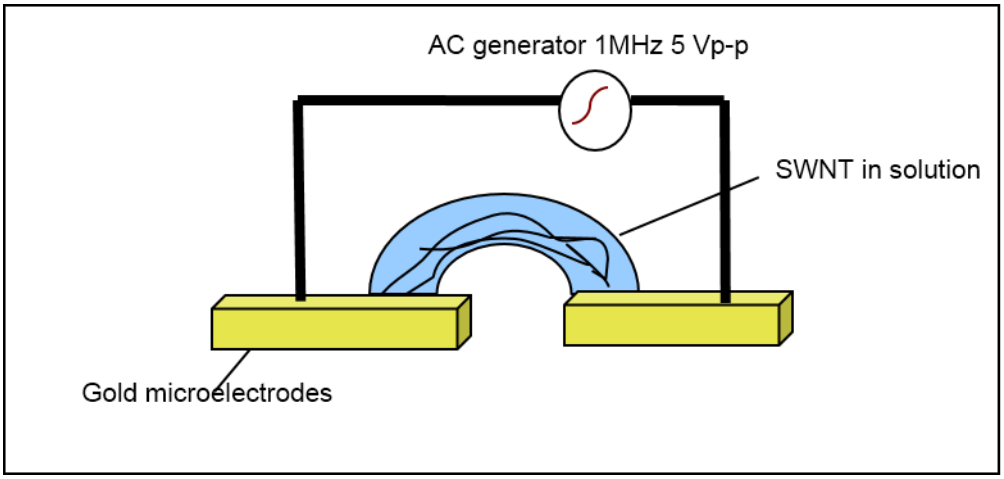

Figure 4.2: Di-electrophoreisis experimental setup where an alternating current of 5V pp at frequency 1 MHz is used to align metallic SWNT across electrodes 1 µm apart.

A DEP probe station has two probes that can be adjusted in the x, y and z directions is used for aligning. This makes it easy to move the probes around the substrate during aligning. The probes are connected to alternating current (ac) at 5 V peak to peak (p-p) at a frequency of 1 MHz from a function generator. The frequency used is a standard references, above that frequency the nanotubes break and below that frequency the alignment is poor. The substrate is placed under the probes with the microstructures to be aligned on, oriented in a perpendicularly to the probes. The setup is shown in Figure 4.2.

Figure 4.3 shows the two electrodes device which was designed and fabricated on a silicon substrate using electron beam lithography for the deposition and alignment of CNTs. This device is called is a high frequency coplanar wave guide. It is designed in such a way that it has two electrodes separated by a 1 µm gap for negative and positive bias more info on the microstructures. Ground electrodes are patterned on both sides of the electrodes. This design facilitates alignment of the nanotubes to establish contact across the two electrodes so that a voltage can be supplied across the electrodes and the current generated through the nanotube measured.

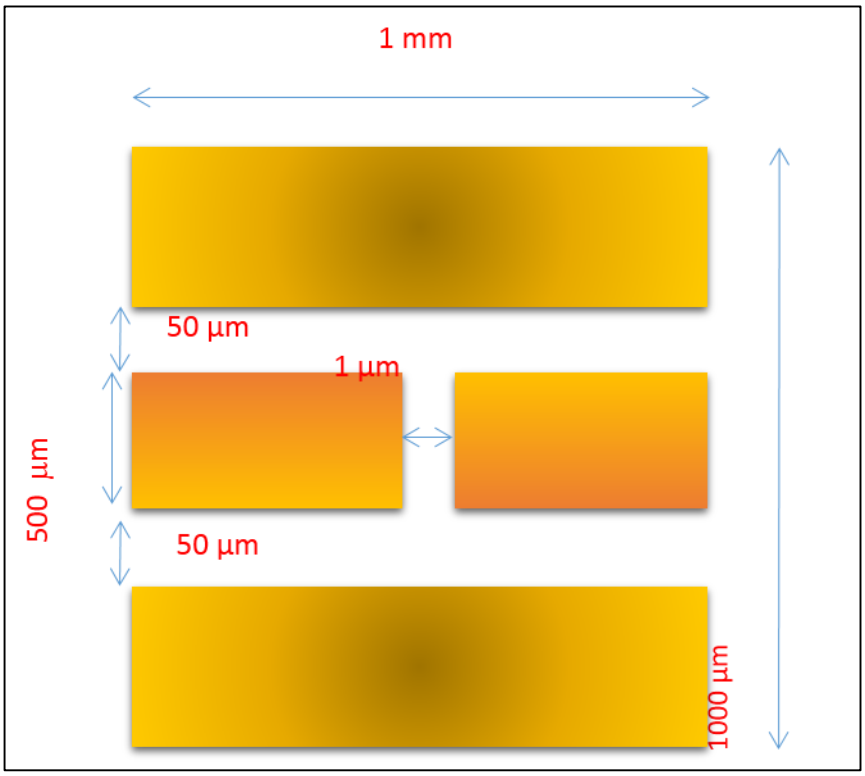

Figure 4.3: Hall microstructure used to fabricate devices by di-electrophoresis across the gap to yield two terminal SWNT devices (Not drawn to scale).

Device info: The microstructures were designed using an auto-CAD (computer assisted design) program, various structures were created on each substrate, and these include four, six and eight armed hall bars, high frequency transmission lines and multi-lined electrodes. The substrates were high resistive amorphous boro-silicate glass. These microstructures were produced using an evaporative technique namely optical lithography, whereby the substrates are covered with a mask having the desired pattern etched out. First tungsten followed by a thin coating of gold are evaporated over the mask, only exposed areas will be marked by the metal thus forming the desired structured contacts. The specific devices used for the measurements in this study were the high frequency transmission lines due to the

favourable dimensions which allowed for effective DEP alignment. The coplanar wave guide dimensions can be seen in Figure 4.3.

To make SWNT devices the probes are contacted on both sides of the electrodes. The oscilloscope is switched on so that an alternating current flows. An optical microscope is used to visualize the alignment. A 0.2 µl drop of the SWNT in DMF is retrieved using a micropipette and deposited across the two electrodes. The ac is kept on whilst monitoring the drop through an optical microscope. Immediately after the drop dries the ac is switched off. Nitrogen is used to dry the substrate further. After the alignment is done SEM is used to check the degree of alignment. These images are generated quickly as the SEM can deposit some carbonaceous material while imaging. The microstructure is placed on a substrate holder secured by a carbon tape. The alignment is checked by zooming into each device where the alignment was attempted and scanning through the cross section of the 1 µm gap. The device is also checked for short-circuiting between ground and source /drain and for any other material that may cause a short- circuit. Nano-manipulators are used to remove any such kind of material. After verifying that contact across the gap is only through the nanotubes the substrate is transferred to the Agilent semiconductor analyser probe station for current voltage measurements. In all cases, voltage was varied from negative to positive. High frequency measurements were performed on the coplanar waveguide (CPW) using an Agilent vector network analyzer (VNA) on the same devices that I-V was performed on at room temperature in a cryostat shielded from light. The measurement was performed from 0.01 to 65 GHz at an IF bandwidth reduced to a frequency of 500 Hz for improved accuracy. Standard de-embedding techniques were employed using an industrially approved Open-Short technique to eliminate parasitic effects.

4.3.2 Modification by metal incorporation

A wet chemistry method is used to incorporate metal onto the SWNTs. The as prepared material was placed in a glass ampoule together with a concentrated solution of nickel chloride ($NiCl_{3)}$. The ampoule was sealed and placed in an electronic furnace for 48 h at a temperature of 523 K. The sample was purified to remove $NiCl_3$ in concentrated 2 M nitric acid at 400 K for 12 h and multiple centrifugations with distilled water, at which after each centrifugation cycle (0.5 h, 4000 rpm), whilst replacing the water after each run [**101**]. As the last step, the sample was heated in air for 1 h, at 593 K, in order to decompose remnants of $NiCl_3$ to nickel and chlorine. Raman spectroscopy studies and SEM were used to investigate the structural changes of the as prepared material due to incorporation of a foreign material.

The Ni incorporated/decorated nanotubes are dispersed in methanol and sonicated in an ultrasonic bath, one sample with a higher concentration and the other with a lower concentration in order to investigate the electronic properties of a single rope and a bundled ropes. The material is aligned by di-electrophoresis on a high frequency microstructure. Current-voltage characteristics of low concentration (individual) and high concentration (bundled) ropes are measured through an Agilent semiconductor high probe frequency station with a micro manipulated semiconductor analyser at room temperature down to 77 K. The data collected is used to conduct resistance-temperature dependence, magneto resistance studies in order to study quantum tunnelling effects which might be able to give a conclusive interpretation of the nanotube-metal interaction.

4.3.3 Measurement under a Probe-Station.



Figure 4.4: Agilent B1500A Semiconductor Device Analyzer used for two terminal devices I-V measurements from 77 K to 300 K.

An Agilent B1500A Semiconductor Device Analyzer micromanipulated probe station is used for current voltage characterization. It is run on desktop operated on EasyEXPERT software. The software provides an efficient test environment for intuitive operation, analysis and exploration in device characterization. It consists of a source/monitor unit (SMU) which allows for the simultaneous supply and measurement of voltage and current through the device respectively. Therefore the real time resistance of the device can be recorded. This measurement system has a high resolution in the pA range. The probe station is mounted on a vibration isolator table to increase stability during measurements. .

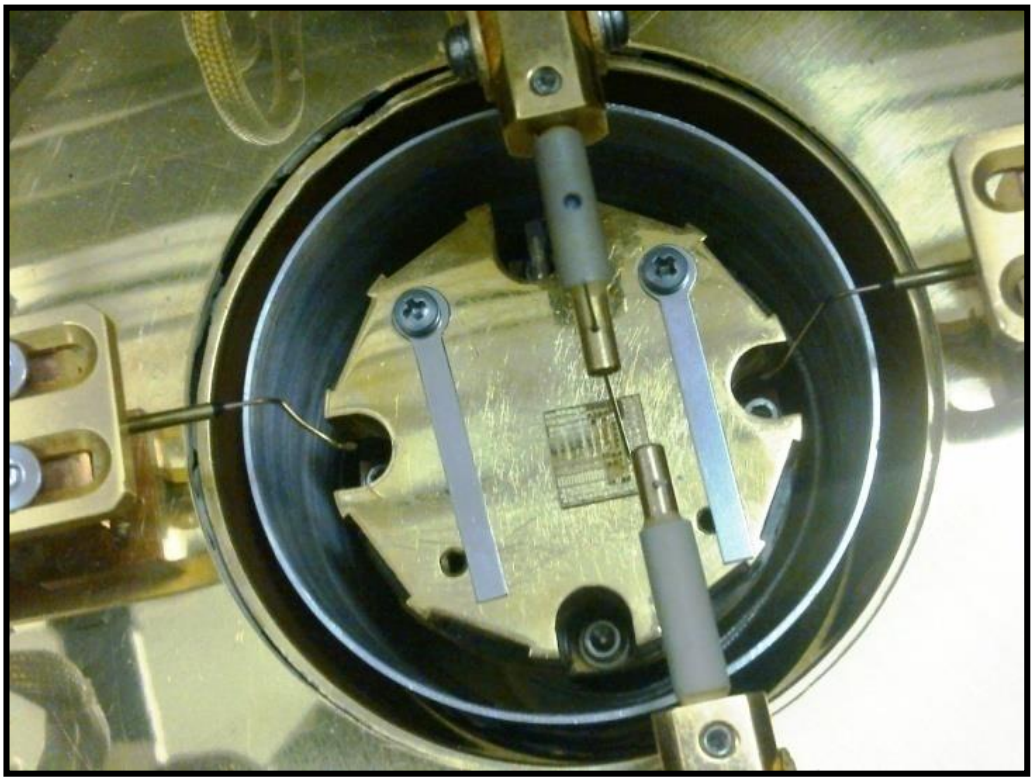

Figure 4.5: Gold microstructure used for fabrication of devices placed on the Agilent B1500A semiconductor analyzer probe station sample chuck.

To perform a measurement the microstructure is placed on the sample chuck in the semiconductor analyser chamber as shown in Figure 4.5. The chamber is sealed off using valves to create a vacuum. A BOC Edwards Turbo pump is used to pump the vacuum down to 1E-6 Pa. Whilst the pump is still running liquid nitrogen is introduced into the chamber through a transfer line causing the temperature in the chamber to go down to 77 K as well as the vacuum to go further down to 1E- 8 Pa due to cryopumping. The nitrogen flow through the transfer line can be controlled by adjusting the respective valves. A workspace is selected in the EasyEXPERT program to source a potential and measure a current. Hold and delay times are introduced to eliminate transient effects.

In the probe station, the nanotube device is contacted by metal tips which can be manipulated in the x-, y-, and z- three directions under a stereo microscope. Care must be taken when manipulating the metal tips so as not to scratch the gold microstructure and create a short-circuit. Extra care is taken by making sure that the z- direction adjustment is stopped as soon as the nanomanipulator makes contact with the gold. All measurements are carried out in the dark. Another precaution that must be taken is with regards to the hazard of electrostatic charge. The electrostatic potential carried by a manipulator can be up to several thousand of volts. Such a high voltage can easily induce a large pulse current through the nanotube which would destroy the device if contact is established. This is avoided by discharging the tips through ground.

High frequency measurements were performed on the coplanar waveguide (CPW) using an Agilent vector network analyzer (VNA) on the same devices at room temperature in vacuum (10^{-5} Pa) in a cryostat shielded from light. The measurement was performed from 0.01 to 65 GHz at an IF bandwidth was reduced to a frequency of 500 Hz for improved accuracy. Standard de-embedding techniques were employed using an industrially approved Open-Short technique to eliminate parasitic effects.

4.3.4 Measurement in the Cryogenic system.



Figure 4.6: Cryogenic measurement system for low temperature electronic transport characterization of SWNT mats from 2 – 300 K in the presence of a magnetic field 0– 12 T

SWNT mat devices were fabricated for low temperature electronic characterisation in the cryogenic high field measurement system shown in Figure 4.6. The devices were fabricated on the substrate holder for four-terminal measurement configurations. The sample is mounted into Cryogenic measurement system through a probe that connects the sample to the electronics. The system is robust and it uses a LabVIEW interface to control the hardware. Resistance temperature measurements were performed from 2 - 300 K for electronic characterisation. We also investigated the change in resistance as the magnetic field was varied from 0 – 12 T at different temperatures for Magneto-resistance studies.

5 Results and Discussion

5.1 Introduction

The main objective of this study was to investigate the electronic properties of single walled carbon nanotubes (SWNTs). The study was partitioned into three different parts which will be discussed in the following subsections. The first involved optimization of the synthesis process to produce high quality SWNTs using pulsed laser ablation. The second part dealt with the structural characterization of SWNTs using SEM, TEM and Raman. The last part is dedicated to the study of the electronic properties of SWNTs in different configurations.

5.2 Synthesis process optimization

To synthesize SWNTs a graphite target containing a metal catalyst is ablated by a laser beam at high temperatures in the presence of argon flow. The factors which critically affect the production of a reasonable yield of high quality SWNTs are the Ar flow rate, laser fluence, growth chamber pressure, synthesis temperature, target geometry, target composition and area scanned during ablation. As discussed in section 3.4.2 there is a thermal gradient in the CVD chamber. At the surface of the target the combination of the laser power and the temperature raises the thermal energy [**102**]. The laser plume is formed at high temperaturesand carried to the reaction by a gas at fixed pressure.As the plume is carried over along the CVD oven the temperature decreases to the ambient temperature~1000 K. The plume condenses in the cooler region and SWNTs are deposited towards the end of the quartz tube.

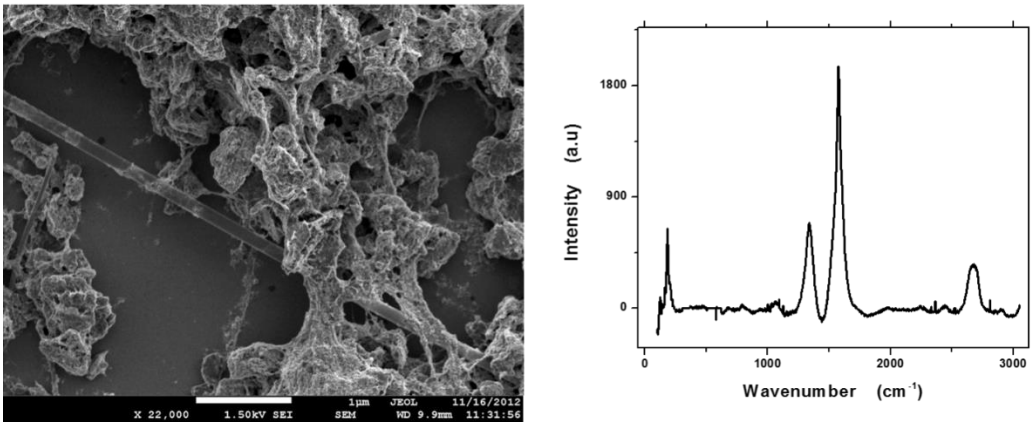

Figure 5.1: SEM image of material produced before optimization of the process parameters showing a combination of high defect SWNTs, fibrous material and carbonaceous material. The Raman confirms that SWNTs have been produced.

Before process optimization, SWNTs containing a mixture of fibrous material and carbonaceous material are produced as shown in Figure 5.1. The $I_D/I_G = 0.42$ shows that the material has a considerable amounts of defects but SWNTs are present as can be seen from the RBM peaks at lower wavenumbers in the Raman spectra. Stepwise optimization of the process was conducted.

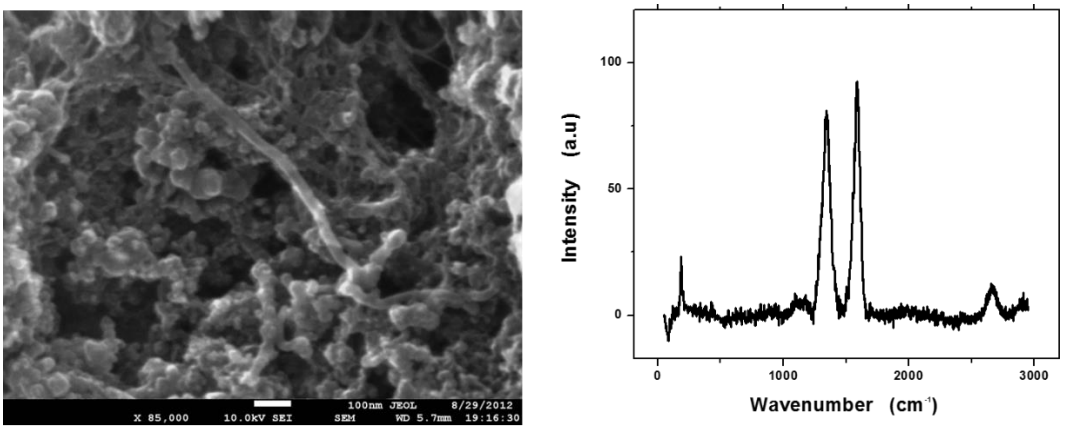

Figure 5.2: SEM image of SWNTs produced at a low laser power showing graphitic material with a very low concentration of SWNTs and the corresponding Raman spectra shows that at a low laser power SWNTs with a high D: G ratio indicating that the material is of poor quality.

During optimization it was discovered that low laser fluence resulted in the production of low quality, high defect SWNT with high concentration of carbonaceous material as shown. At a low fluence, graphitic powder with a small percentage of SWNTs is synthesized as shown on the SEM image and Raman, Figure 5.2. This results from chunks ablated from the target at a low fluence which are not broken down to atomic sized particles (plume) that are more favourable to SWNT formation. The SWNTs have a high $I_D / I_G = 0.82$ indicating high defects concentration.

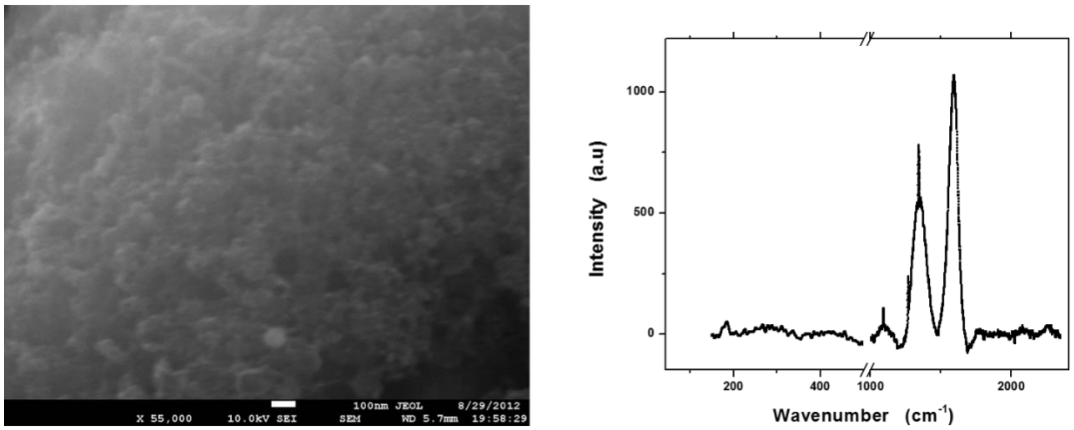

Figure 5.3: SEM image of resulting material at temperatures lower than 900 K showing graphitic material and the corresponding Raman spectra shows that the material produced does not contain SWNTs

At temperatures lower that 900 K graphitic material with no SWNTs were produced as shown in Figure 5.3. The material produced has a high I_D / I_G ratio, 0.65 showing that very poor quality graphite is produced at lower temperatures. We also observed that a flow rate lower that 200 sccm resulted in a low yield of high defect SWNTs and a pressure lower or higher than 600 mbar decreases the yield.

The target geometry and composition were also assessed using the [**98**] recipe for synthesis and a target with a composition of 98%C; 1%Ni; 1% Co as stated in Sec 3.4.1. We discovered that using a pre-pressed 20 mm pellet in a 25 mm tube retarded

free stream conditions. This is due to the fact that the geometry of graphite target plays an important role on the dynamics of the gaseous carbon plume ejected from the target. The yield was extraordinarily low at the recommended conditions seen in Figure 5.4. Furthermore we noticed that the target degrades over time as graphite absorbs oxygen and nitrogen from the atmosphere which act as impurities. Hence good results were obtained from a freshly annealed pellet.

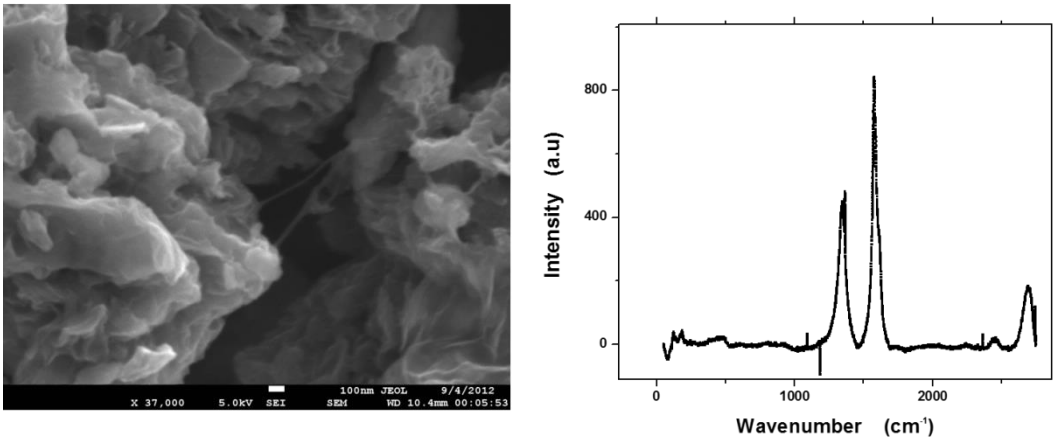

Figure 5.4: **SEM image and Raman spectra of low yield SWNT due to target geometry retarding free stream conditions.**

Before optimization a thin layer of powdery material with a high concentration of carbonaceous material was collected in the reaction zone a very low concentration of SWNTs as shown by the weak RBM peaks. The laser power and furnace ambient temperature were tuned in order to ensure breakdown of graphite to atomic level, as well as the gas flow rate to carry the plume to the reaction zone unperturbed. At a low laser power and low temperature more of the graphitic carbon is produced close to the target surface due to the inability to breakdown the carbon to atomic level. If the flow rate is too low the atomic plume loses its momentum and condenses close to the target surface.

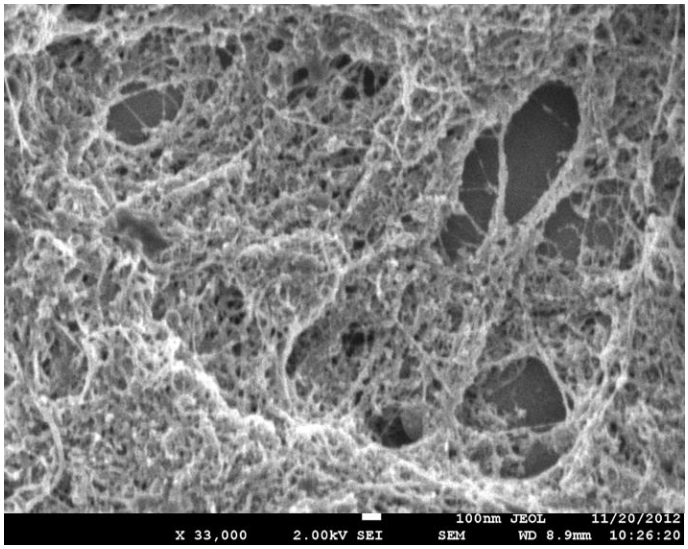

Figure 5.5: **SEM image of SWNT nanotubes produced after optimization of all process parameters showing a high yield of SWNT ropes embedded in carbonaceous impurities before purification.**

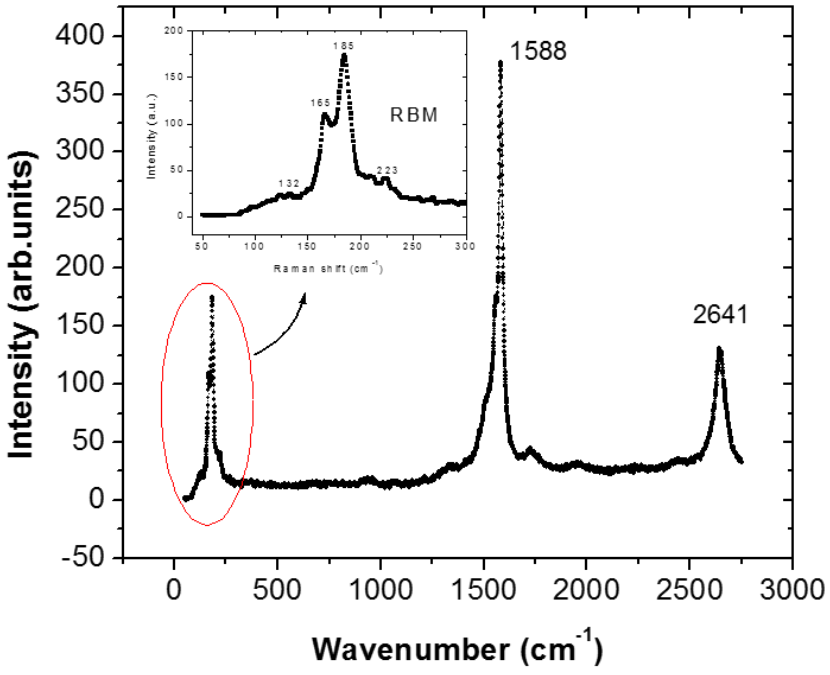

Figure 5.6 : **Room temperature Raman spectra (green laser light) of SWNTs bundle produced by pulsed laser ablation before purification showing the RBM frequency, a signature of SWNTs and very low D band to G band ratio which confirms the high quality of the material produced. Inset shows the spectrum**

fragment of the RBM frequency mode peaks due to the different diameter tubes that make up a bundle.

After optimization of all process parameters a high yield of SWNTs were synthesized using the process parameters reported in 3.4.2. Figure 5.5 is an SEM image showing a high yield of SWNT ropes embedded in impurities. The corresponding Raman spectra is shown in Figure 5.6 showing a very low I_D/ I_G = 0.04 and high intensity RBMs which confirms that the material produced is high quality SWNTs.

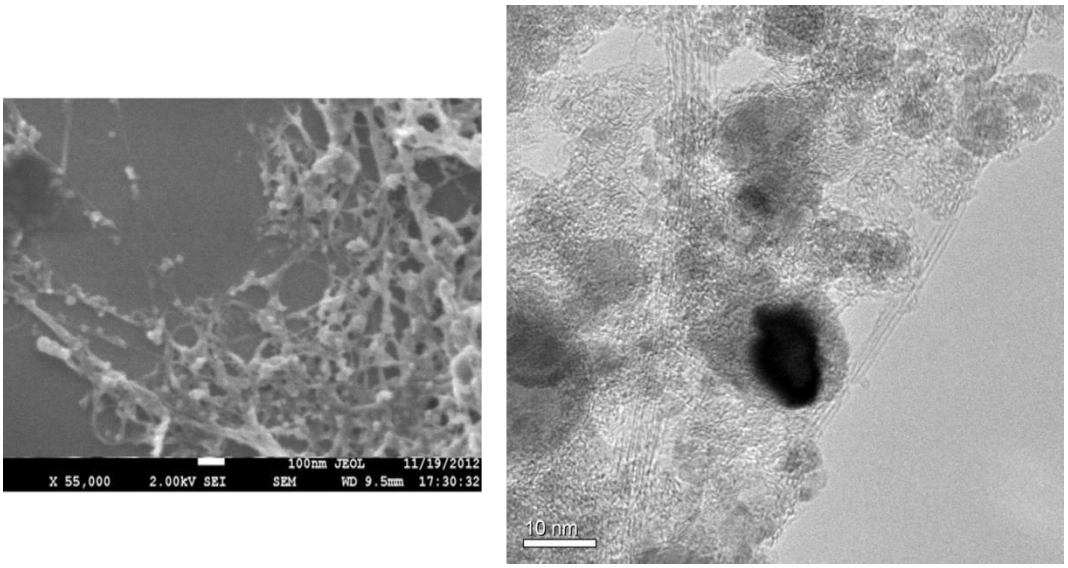

Figure 5.7: SEM image of the as prepared material showing ropes of SWNTs with impurities and the corresponding TEM images shows a SWNT ropes with catalyst impurities

Figure 5.7 is an SEM image showing the spaghetti like material produced from the optimized synthesis conditions consisting of large amount of SWNT ropes. The corresponding TEM shows that the ropes coagulate due to the weak van der Waals forces of attraction complimented by the Raman analysis. Dispersing small amount of the SWNT in a solvent and soliciting facilitates the separation of the rope bundles. The TEM images also show the catalyst impurities that are found in the as-

prepared material.

The as-synthesized material is purified as discussed in section 3.4.3. After purification the SWNTs can be seen as ropes with different diameters Figure 5.8 and remnant carbonaceous impurities which can be extracted by DEP which favours the alignment of metallic tubes.

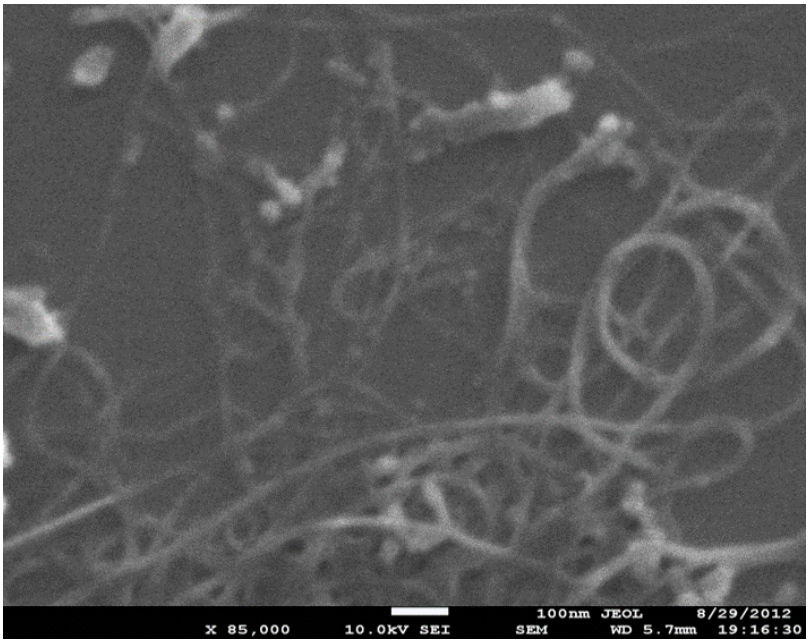

Figure 5.8: SEM images after purification showing SWNT ropes with different diameters and remnant impurities.

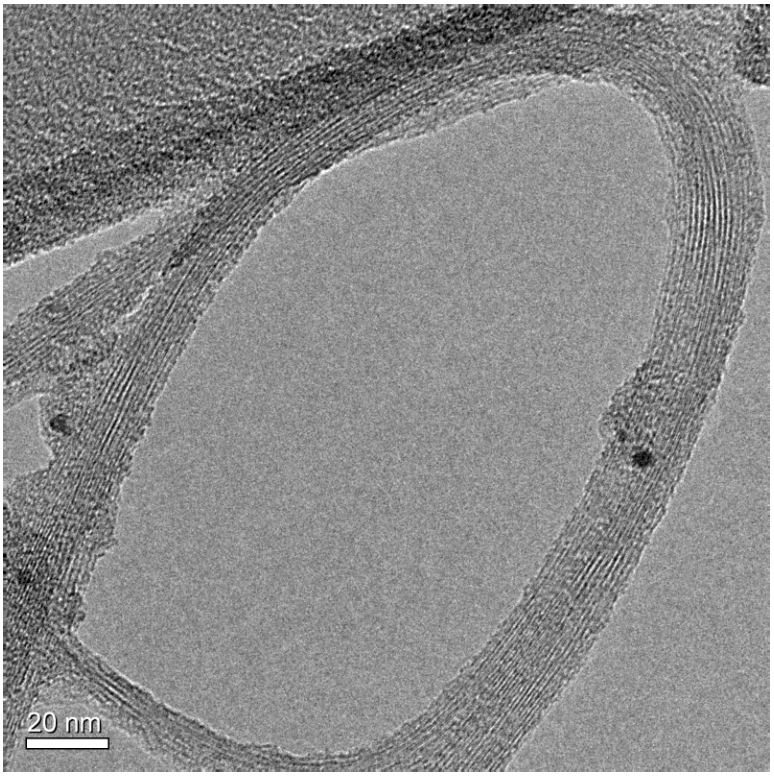

Figure 5.9: **TEM image of a single rope of SWNT with a diameter of approximately 20 nm consisting of about 15 nanotubes.**

Figure 5.9 is a TEM image showing individual ropes which approximately 20 nm thickness. It is clear to see that these are ropes not MWNTs which would be characterized by a hollow center giving the diameter of the innermost tube The laser ablation process promotes the growth of SWNT ropes not free-standing individual nanotubes. SWNT device were fabricated from ropes which reduces the probability of introducing defects into the material during processing.

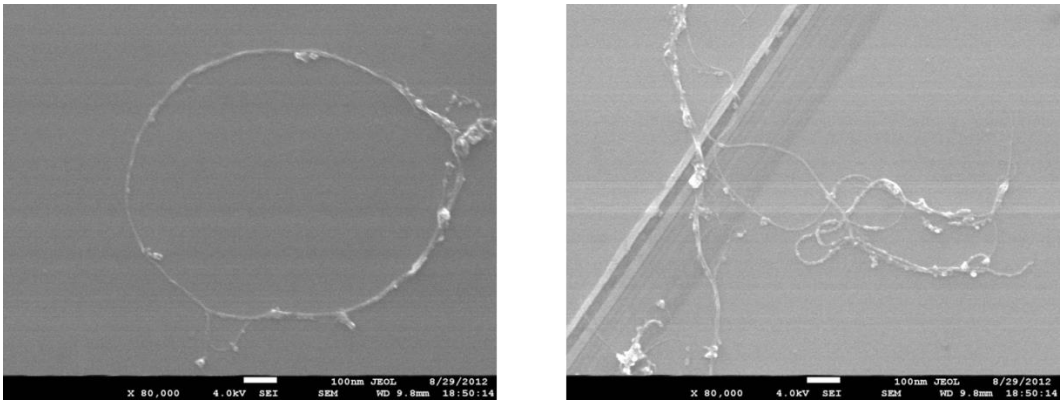

Figure 5.10: Individual SWNT ropes on Si substrate showing that bundles that can be separated into single ropes by ultra-sonication.

Furthermore the purified material was deposited on Si substrate after ultra-sonication. The SEM image Figure 5.10 shows how the bundles were separated into individual long ropes with fewer impurities compared to the purified bundle. This becomes an advantage when it comes to fabrication of DEP aligned devices.

5.2.1 Raman analysis of SWNTs

The most significant feature to look out for in the Raman results is the presence of the radial breathing mode (RBM) frequency, a signature of SWNTs in the low wavenumber range of the spectrum. The spectra recorded are shown in Figure 5.6 and confirm that the material synthesized is indeed SWNTs. Complimentary features are the disorder induced D band and the tangential mode G band as stated in section 4.2.1. The diameter of a SWNT is proportional to the position of the RBM Raman peak [**103**] the relationship being given by the equation;

$$\overline{\upsilon}_{RBM} = \frac{\mathbf{A}}{\mathbf{d_t}} + \mathbf{B} \qquad \mathbf{5.1}$$

Where $\overline{\upsilon}_{RBM}$ is the RBM wavenumber, d_t is the diameter of the corresponding nanotubes and A=243 cm^{-1} and B=10 cm^{-1} for a bundle, constants determined by the environment [**104**]. We used this relationship to approximate the diameter distribution of the sample by evaluating each RBM peak for different laser

excitation wavelengths. From the Figure 5.6, the spectra taken from green laser light, the prominent diameter distribution is 1.34 nm and 1.50 nm corresponding to the 185 cm^{-1} and 165 cm^{-1} wave numbers the better part of the bundle being 1.34 nm as observed from the intensity. There is a small amount of tubes with diameters of 1.91 nm and 1.04 nm in the bundle. Thus the diameter distribution detected by the green light is 1.04 - 1.91 nm.

The morphology of synthesized material is shown by the features of the G peak, where the G^- peak is slightly visible and the G^+ peak is symmetric The G band which is an indication of sp^3 bonding is very sharp showing low disorder, the D band which is an indication of disorder at 1300cm^{-1} is slightly visible with a very low intensity in comparison to the G band (I_D/I_G is low) which shows that this is a high quality carbon nanotube sample with low defect concentration.

Figure 5.11 shows the Raman spectra of the SWNTs taken with different laser excitations, namely red (785 nm) and green (514.5 nm) light. Figure 5.11 inset shows the RBM spectra from the different laser excitations. It should be noted that the shapes of the RBM spectra are a little different from one laser excitation to the other as reported by Rao *et al.* [**105**].

Figure 5.11 confirms that the RBM frequency is determined by the diameter of the nanotube, Eqn. 5.1. This confirms that laser ablation grown SWNTs are made up of different diameters as detected by the different laser excitations. Furthermore it can be seen from the spectrum that the red light is more sensitive and detects a wider diameter distribution compared to the green light. Hence a bundle of SWNTs contains nanotubes of different diameters which are sensitive to a particular excitation wavelength and it is recommended to do multi-wavelength Raman spectroscopy to get a clearer picture of the diameter distribution.

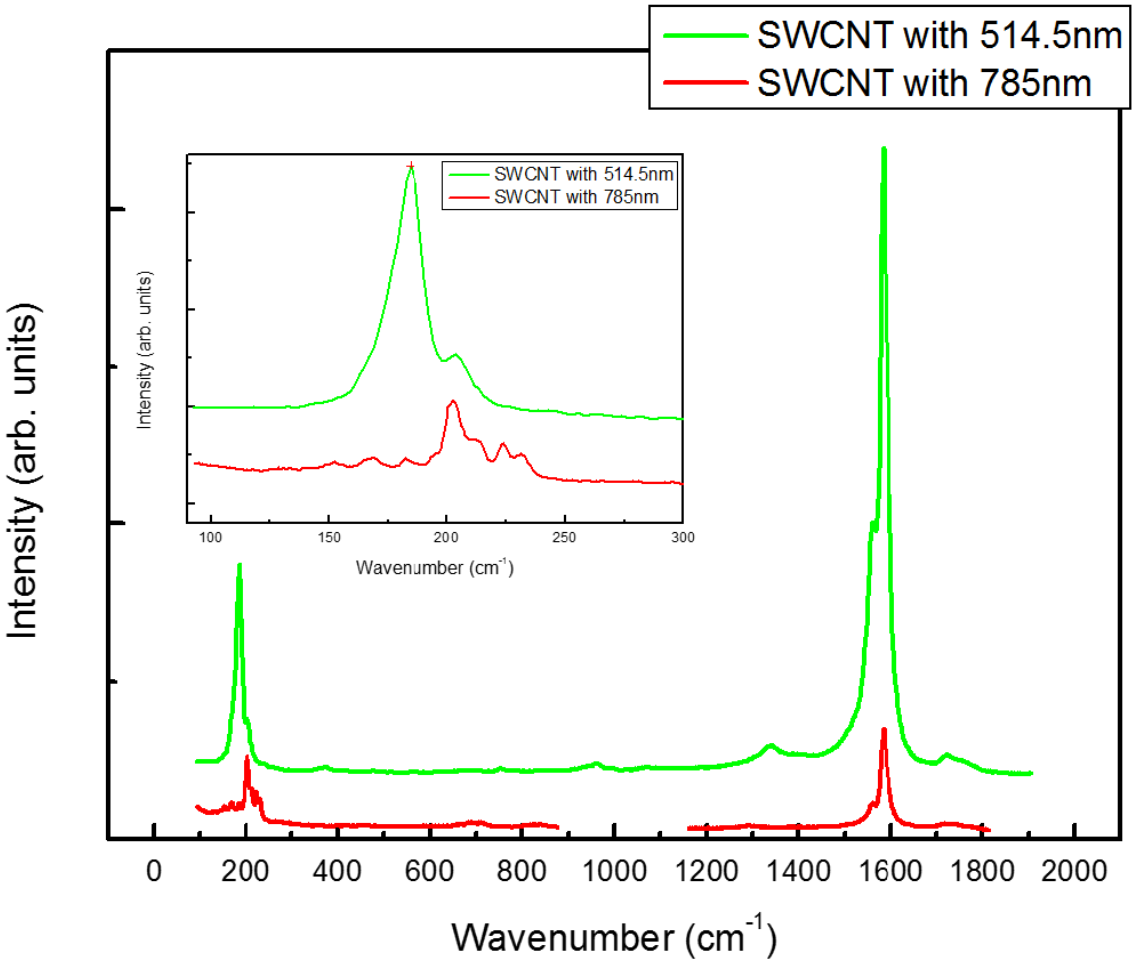

Figure 5.11: **Raman spectra taken at different laser excitation wavelengths showing that different laser wavelengths are sensitive to nanotubes with different chiralities hence different diameter distributions can be picked up from different laser wavelengths.**

5.2.2 Summary of synthesis conditions

During process optimization we were able to investigate the effect of the different process parameters on the quality and yield of the SWNTs. The thermal energy (laser power and temperature) determines the atomization of the plume hence the

quality of the nanotubes synthesized. A low laser power results in the ablation of large chunks of material which cannot be carried over to the reaction zone. A lower temperature has a similar effect. The gas flow rate determines the amount of material carried over to the reaction zone. A low flow rate reduces the yield. The target composition affects the yield of SWNTs as the catalyst determines the seeding during growth. The bimetallic catalyst supports growth better than most catalysts.

In this work we report that a good yield producing 1 mg/min^{-1} of high quality SWNTs as shown on SEM image Figure 5.5 complimented by the Raman spectra Figure 5.6 were produced only after the process was optimized to the following conditions; temperature 1373 K, Argon flow rate 200 sccm. Pressure 600 mbar, target composition 98%C; 1%Ni; 1%Co. The Raman analysis of the nanotubes synthesized under these conditions shows that the material produced is low defect and high quality SWNTs.

5.3 Electronic transport through SWNT mats.

It is necessary to understand the electronic transport through SWNT macroscopic configurations due to the fact individual nanotube devices present a lot of challenges. It has also been discussed that the synthesis of nanotubes of a controlled geometry is still an open problem. Hence the macroscopic SWNT devices are more feasible. The material finds applications for the fabrication of CNT-based sensors, where the signal from the sensor output depends on the conductivity of device [**106**]. In such configurations the defects and length of the individual tubes as well as the contact resistance of the array are the factors most critical to electronic transport.

In this section we report the electrical transport properties of SWNT mats derived from resistance as a function of temperature (*R-T*) measurements, as well as the magneto-transport (*MR*) trend also derived from the former as a function of

magnetic field. The TEM image of the sample, Figure 5.6 shows a rope of SWNTs which make up bundles due to the weak van der Waals forces of attraction. A mat consists of a random network of these one dimensional SWNTs bundles which can be modeled as a 3 dimensional metal (depending on the thickness of the mat) [**86**]. The investigation was done from 2 K to room temperature and the magnetic field was ramped from 0 – 12 T. This measurement is expected to give the bulk properties of the material, which in principle might also indirectly give information about the transport properties of the individual tubes.

5.3.1 Electrical resistance

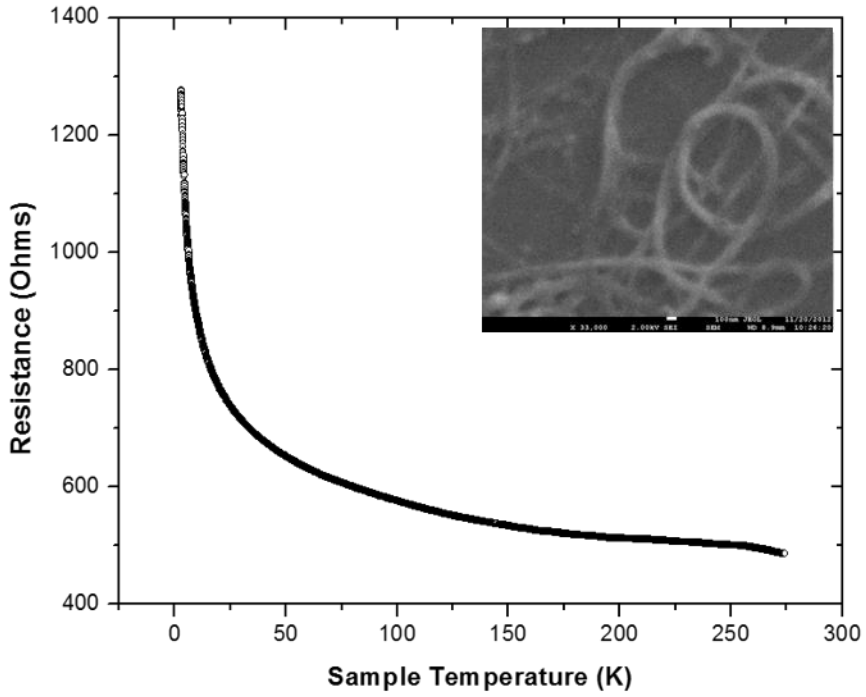

Figure 5.12: Resistance as a function of temperature of SWNT mats measured from 2 – 275 K showing an exponential relationship. Inset SEM image of SWNT mat.

The resistance, *R* of the SWNT mat at room temperature was measured to be 500-1000 Ω subject to contact quality using a Fluke multi ammeter, which is in good

agreement with results reported in literature [**107**]. Figure 5.9 shows the resistance (R) as a function of temperature (T) for several samples of SWNT samples. For all the samples characterized the resistance, increases exponentially as the temperature is decreased, with a significant increase from $T < 200$ K which proposes a hopping kind of conduction mechanism.

Fitting the R-T results confirms that the conduction mechanism in the SWNT mats is primarily hopping as proposed by the Mott Variable range hopping (VRH} model [**90**], given by Eqn. 5.2. The R-T data is well fitted by Mott's law for 3D VRH conduction.

$$\mathbf{R_T = R_0 \exp\left[(T_o/T)^{(1/d+1)}\right]} \qquad \mathbf{5.2}$$

Where the R is resistance and T_o is the Mott temperature which defines the thermally activated hopping among localized states at different energies. The d = 1, 2 or 3 in the Mott model determined by the dimensionality of the system and $T_o = \beta e^2/k_B \kappa \lambda$, where k_B is the Boltzmann constant, κ is the dielectric constant of the material, λ is the electron localization length and $\beta = 18.1$ [**108**]. Figure 5.13 shows that the best fit for the experimental data is for n=3, the other exponents give a poor fit implying

that T_0 = 13.57 K and R_0 = 310 Ω, determined from the graph.

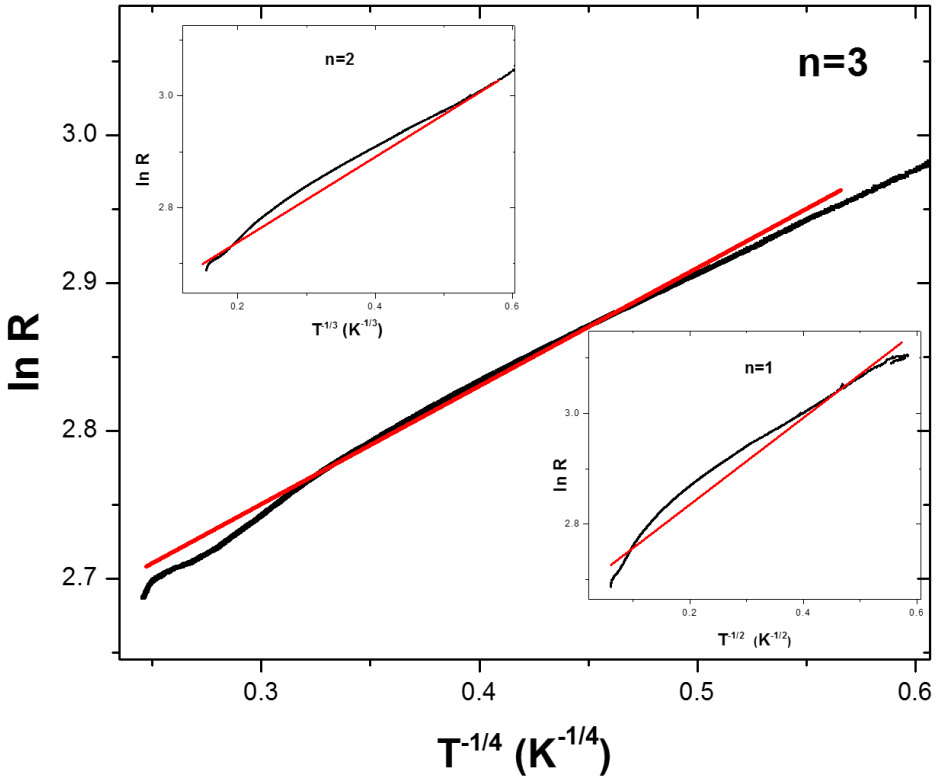

Figure 5.13: **Fitting the resistance temperature dependence data for a SWNT mat show that Motts 3D VRH is the predominant conduction mechanism. The upper inset shows the poor fit for 1D VRH indicating that the Coulomb interaction between electrons is negligible. The lower fit shows the poor fit for 2D VRH.**

The Mott 3D VRH as shown by Figure 5.13 is the dominant conduction mechanism within a SWNT mat synthesized by pulsed laser ablation revealing the 3D nature of the electrical transport in the mat consisting of the ID SWNTs. The poor fit to its 2D VRH, as shown in the lower inset of Figure 5.13, shows that the Coulomb range VRH conduction mechanism [**109**,**110**] is not applicable hence coulomb interactions between electrons is insignificant in the 3D mat. This realization is important due to the significance of the Coulomb interactions in the 1D SWNTs that comprise the mat. This implies that even as the temperature is decreased the

Coulomb effect is negligible and electrons hop to the most probable site within the neighborhood of the Fermi level as expressed in Eqn. 5.2. The poor fit in the 2D – VRH model (upper fit) shows that this is not the dominant conduction mechanism in SWNT mat. The hopping ranges can be determined from *MR* measurements by using this equation;

$$\mathbf{R_h = \frac{3}{8}\left(\frac{T_0}{T}\right)^{1/4}\lambda} \qquad \mathbf{5.3}$$

Where R_h is the hopping range T_0 is the Mott temperature, T is the temperature and the λ the electron localization length.

5.3.2 Magneto-resistance

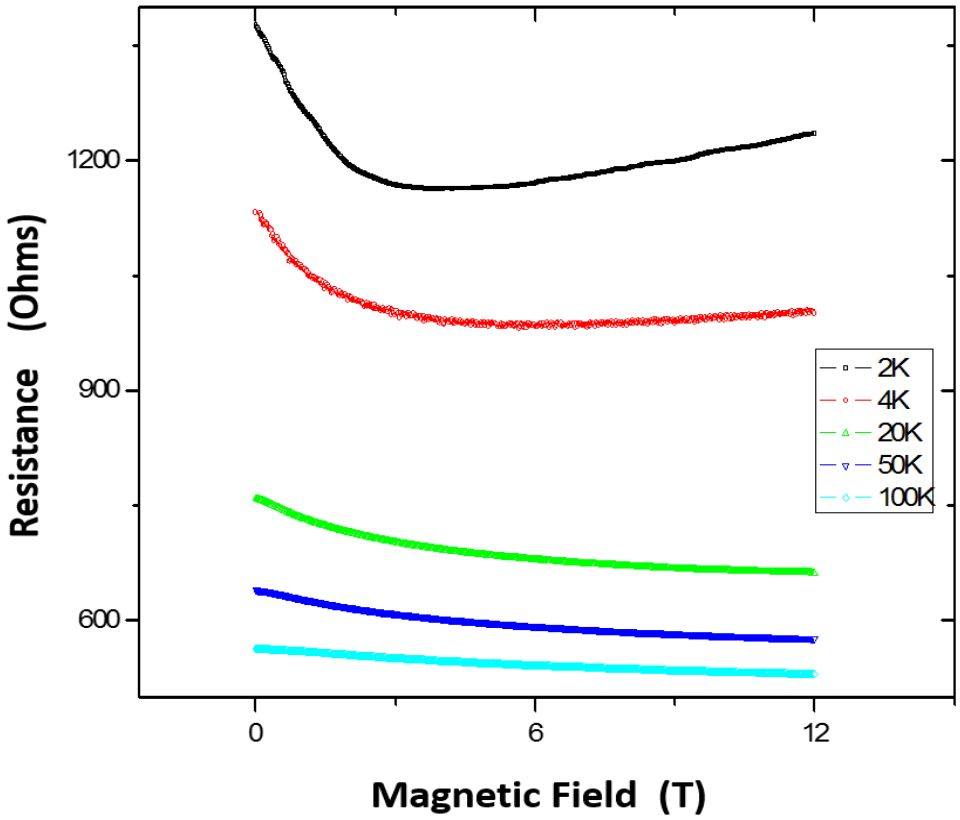

Figure 5.14: **Resistance against magnetic field at different temperatures from 2 to 100 K for a SWNT mat in the cryogenic high field measurement system showing the transition from parabolic to linear response.**

The resistance of a material changes as the magnetic field is varied. The change in resistance as a magnetic field is applied to a mat of SWNTs is shown in Figure 5.14. It shows a temperature dependent trend from 2-100 K. The magneto-resistance (*MR*), well-defined as the difference in resistance divided by resistance at zero magnetic field, was plotted for different temperatures as shown in Figure 5.15. It was found that it is predominantly negative with a parabolic nature which decreases to a linear nature as the temperature is increased. The parabolic nature is an indication that the overall *MR* dependence on the applied magnetic field is a sum of the positive and the negative contributions. Furthermore it was found that the *MR* is strongly related to the temperature hence the change from parabolic to linear response.

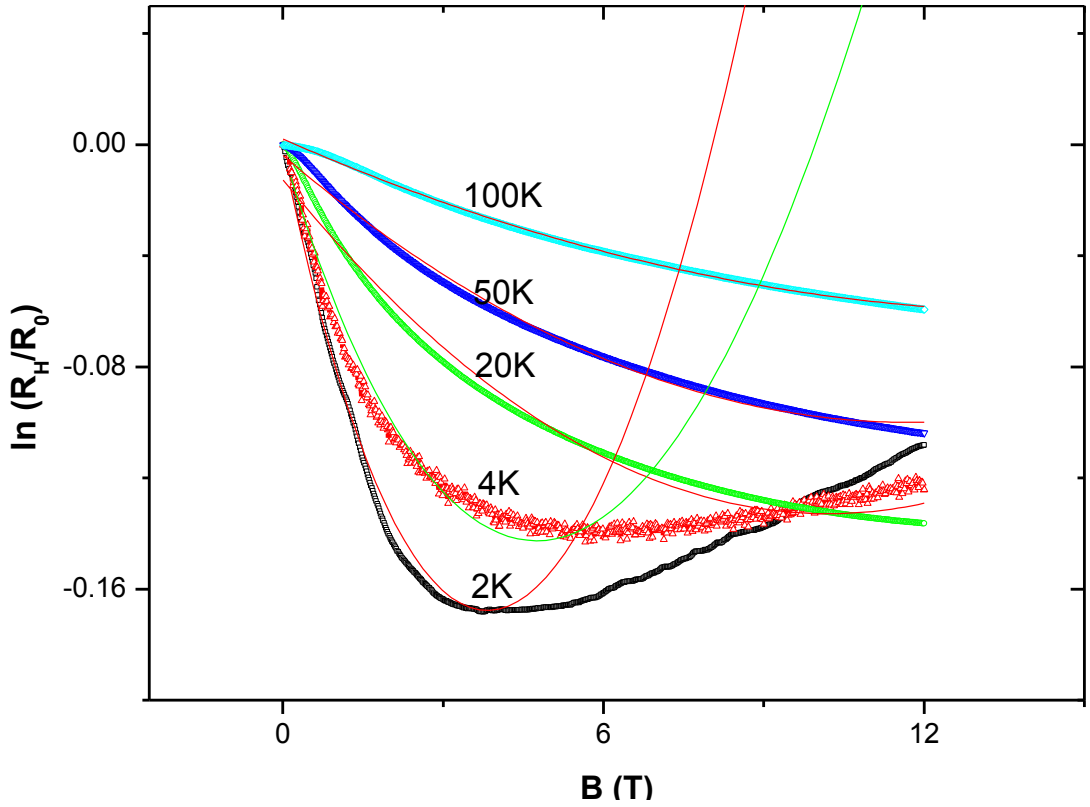

Figure 5.15: **Magneto-resistance at different temperatures exhibiting a parabolic nature at low temperatures and linear nature at higher temperature due to quantum interference and wave function shrinkage respectively.**

The negative *MR*, which seems to be linear against magnetic field, in the low field limit (0 – 6 T) is a consequence of quantum interference between numerous hopping paths as reported by Nguen *et al* [**111**].Quantum interference is associated with the scattering of electron due to impurities along the conduction strip. So the resulting hopping amplitude is the sum of different tunnelling paths, which interfere among themselves. The nature of hopping conductivity is such that backscattering is strongly emphasized and thus the interference contribution leads to a decrease of the conductivity [**112**]. The magnetic field suppresses the interference and leads to the negative magneto-resistance. The positive MR which is more apparent at low temperatures and magnetic fields greater than 6 T is a consequence of wave function shrinkage, a state where the electron orbitals shrink at extremely low temperatures resulting in the positive *MR* due to a reduced hopping probability [**113**].

Below 4 K the MR is parabolic within the 0 – 12 T range, whereas above 20 K it starts to decrease to a predominantly linear response. The positive and negative *MR* contributions affect the conductivity differently. Fitting the data shows that the conduction mechanism at low temperatures below 4 K is different from that above 20 K. In all the samples measured at temperatures above 20 K the effect of the additive mechanism could be modeled by;

$$\mathbf{ln(\rho_H/\rho_0)} = -\mathbf{a_1 B} + \mathbf{a_2 B^2} + \mathbf{a_3} \qquad \textbf{5.4}$$

Where the a_1 is the coefficient of quantum interference, a_2 is the coefficient of wave function shrinkage and a_3 is the coefficient which accounts for the complex nature at low fields. The coefficients a_1 and a_2 can be determined by fitting the *MR* data to Eqn.5.4 as illustrated by the lines in Figure 5.15 for each temperature. More details on the scattering and hopping processes happening in the SWNT mat can be evaluated from the value of the coefficients. For strongly localized systems the wave function shrinkage gives the positive *MR* as;

$$\ln(\rho_H/\rho_0) = t(\lambda/L_H)^4(T_{mott}/T)^{3/4} \qquad 5.5$$

Where *t* is a constant = 0.0025 in 3D, and $L_H = (\hbar/eB)^{1/2}$ denotes the magnetic length [**114**] where h-bar is the reduced Planck's constant and λ the electron localization length. However it is observed that model expressed in Eqn. 5.5 does not qualitatively fit the *MR* response at low temperatures, below 4 K. It can explain the negative *MR* response at low temperatures but deviates for the positive magneto-resistance as seen in Figure 5.15.

$$\ln(MR + 1) = \gamma B^2 T^{-3/4}$$

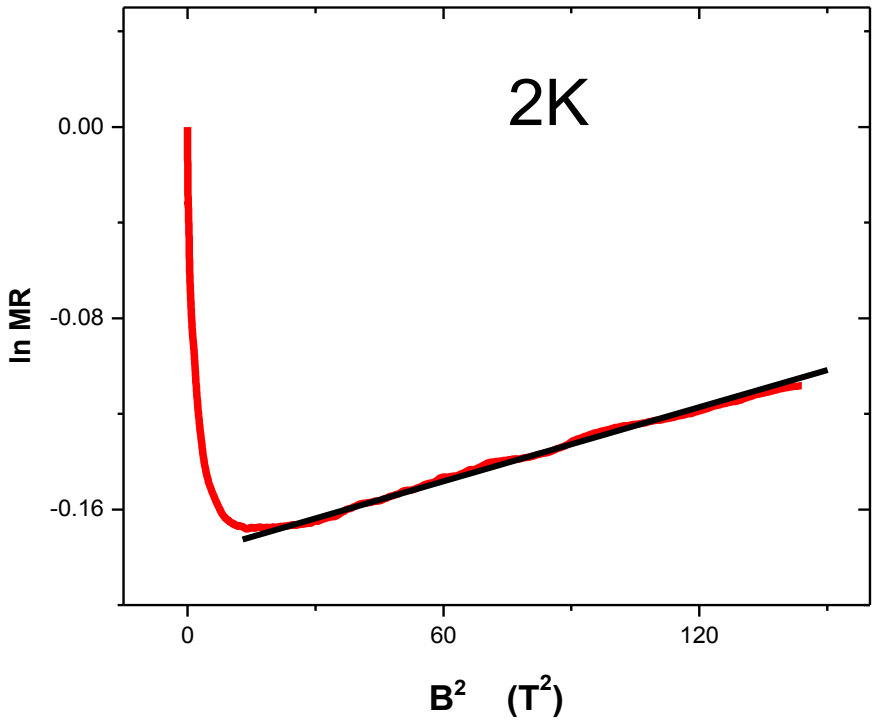

Figure 5.16: Positive magneto resistance at low temperature (extracted from figure 5.15) for SWNT mats showing exponential B^2 dependence due to pronounced wave function shrinkage effects.

This positive *MR* upturn at low temperatures can be explained by the theory developed by Shklovskii [**115**], as shown in Figure 5.16 the positive MR satisfies the following equation:

$$\mathbf{ln(MR + 1) = \gamma B^2 T^{-3/4}} \qquad \mathbf{5.6}$$

Where *MR* is the magneto-resistance, γ is a constant, *B* and *T* are the temperature and magnetic field respectively. Using Eqn.5.3 and the temperature dependence of the coefficient of wave function shrinkage, a_2, the electron-localization lengths and hopping ranges were determined respectively, with respect to temperature as shown in Table 5.1. The coefficient of the quantum interference, a_1, from the *MR* fits was plotted as a function of temperature so as to determine the scattering limit of the SWNT mat.

Table 5.1: Calculated parameters from R (T) and R (H) data

Temperature (K)	**a_1**	**a_2**	**T_{mott}**	**Localization length (λ) (nm)**	**Hopping Range (nm)**
2	0.0989		13.57		
4	0.0671				
20	0.0236	2.8636 E -4		16. 05	5.46
50	0.0163	6.9805 E -4		23. 83	6.44
100	0.0085	0.001162		30.78	8.31

The coefficient of quantum interference determined in Table 5.1 was plotted against temperature, Figure 5.17 to determine the scattering limit of the SWNT mat. Theoretically a_1 is expected to be constant in a strong scattering limit and increases with a decrease in temperature in a weak scattering limit [**116**]. As seen from Figure 5.17 the latter is true for our samples where $a_1 = 0226T^{-0.75}$ which is similar to the

expected theoretical prediction for a 3D system, $a_1 \approx T^{-0.88}$ [**117**].The coefficient of quantum interference of our sample decreases with temperature implying that the scattering of the electron wave function due to impurities becomes more pronounced as the temperature is increased hence increasing conductivity.

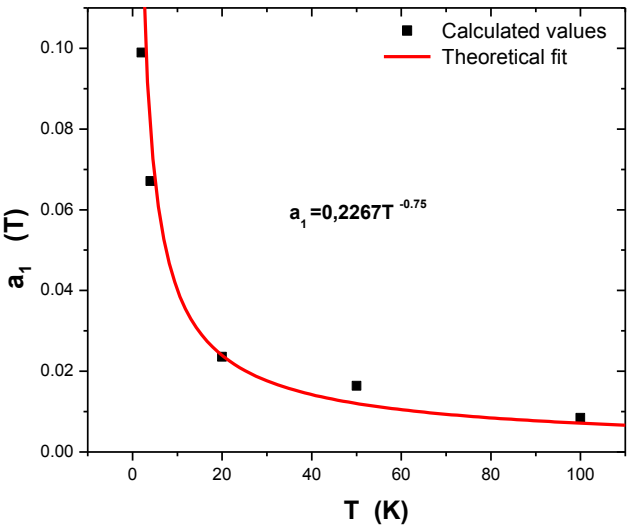

Figure 5.17: Temperature dependence of a_1 (from Table 5.1) determined from the fits in Figure 5.15 used to determine the scattering limit of SWNT mat.

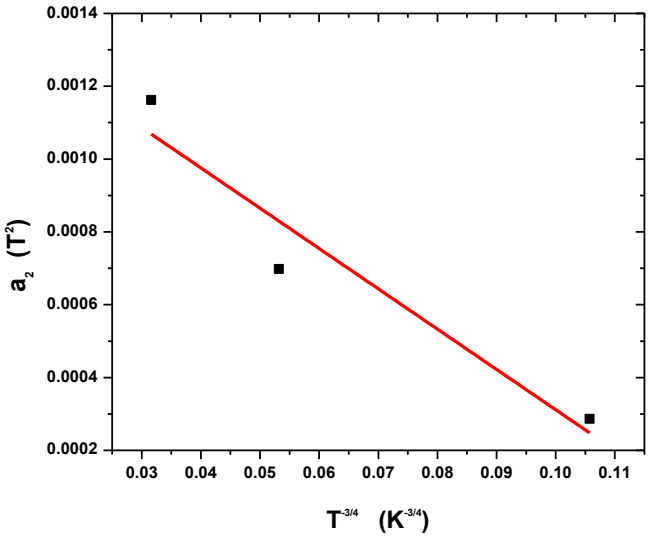

Figure 5.18: **Calculated a_2 (from Equation 5.3) at different temperatures to determine the localization length of the SWNT mat.**

The physical significance of a_2, the coefficient of wave function shrinkage, is defined in Eqn. 5.5 for temperatures above 4 K in relation to the localization length. Using the absolute value of the gradient determined from Figure 5.18 the localization length of the SWNT mat is 23 nm. The coefficient of the wave function shrinkage is directly proportional to temperature, which implies that the probability of electron hops increases with thermal energy. Hence as the temperature is increased the shrinkage of the wave function becomes less pronounced due to enhanced hopping and the resistance of the sample decreases.

5.3.3 Discussion

The *R (T)* and *R (H)* data both support 3D VRH as the dominant as the conduction mechanism in a nonporous system of a SWNT mat. Since the localization length, λ is much less that the sample thickness ~ 1 mm but comparable to the individual rope diameter that comprise the mat, ~20 nm, hence the 3D VRH is between the ropes

through the nanotube-bundle contacts in a mat.

The SWNT mat forms a system of localized electrons where the electronic states are three dimensional with a radius much greater than the distance between intertube contacts. This result is inconsistent with any model of localization in which the tube electrons are confined to a single tube or bundle. We suggest instead that the carriers in an SWNT mat are in fact localized by disorder caused by intertube or intratube defects or deformations.

The negative magneto-resistance in the low field limit is due to dependence of the localization lengths on the thermal energy. The positive magneto-resistance is a result of intrastate interactions as the occupation probability of the electron changes due to a magnetic field at low thermal energies. Even though the intrastate interaction does not change the temperature dependence of the resistivity, the electron-electron interactions in the Anderson localized states [**118**] play an essential role in the magneto-resistance. At low temperatures the electron propagates larger distances compared to higher temperatures due to quantum effects. The negative *MR* arises from structural defects within the SWNT mat leading to quantum interference of the electronic wave function, which localizes the charge carriers in one-dimensional systems and increases resistance.

5.4 Electronic transport in a rope of metal incorporated SWNTs.

It is well known that SWNT's have potential for numerous applications. Modification of their physical properties is important so as to extend their applications. Metal incorporation is of particular interest due to the fact that it extends the application of the SWNT to spintronic device application, provided the metal used is ferromagnetic. However it is very difficult to incorporate metal into the constricted area within the inner core of the nanotube due to its very small diameter 0.4 - 2 nm in comparison to the diameter of the filler elements. Hence a method to incorporate metal onto the outer surface of the SWNT is used to investigate resulting electronic properties.

We investigated the electronic transport properties of individual and bundled ropes of nickel incorporated (SWNT) using low temperature studies. Decoration efficiency was also investigated through SEM microscopy which showed that the metal was incorporated around the SWNT ropes. Raman spectroscopy studies were also used to investigate the effect of incorporating metal. Figure 5.19 is an SEM image of the SWNT's which were exposed to nickel incorporation by a wet chemistry method before purification. Figure 5.20 is a SEM image showing effective incorporation of nickel around the outer surface of the individual ropes after purification. After purification the incorporation of the nickel onto the outer walls of the SWNT ropes is clearly seen. The metal appears as randomly spaced beadlike material along the rope.

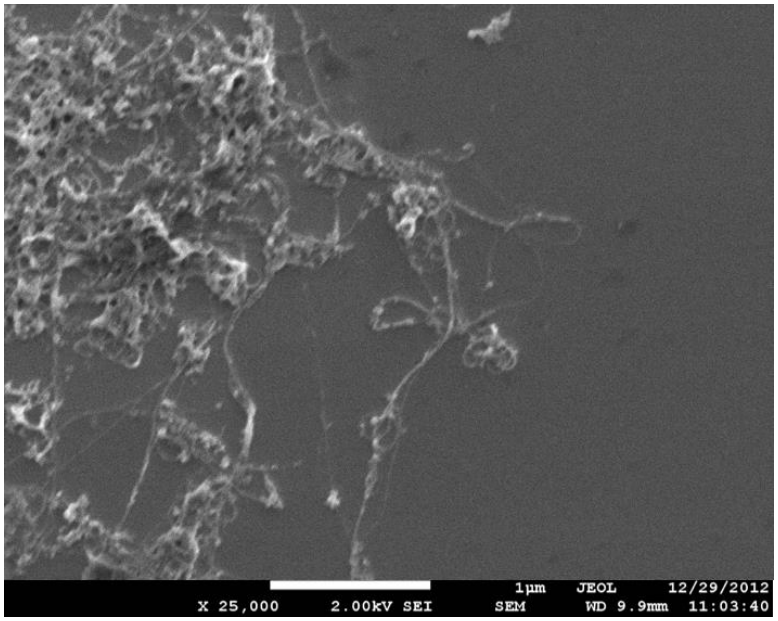

Figure 5.19: SEM image of metal incorporated SWNT ropes before purification.

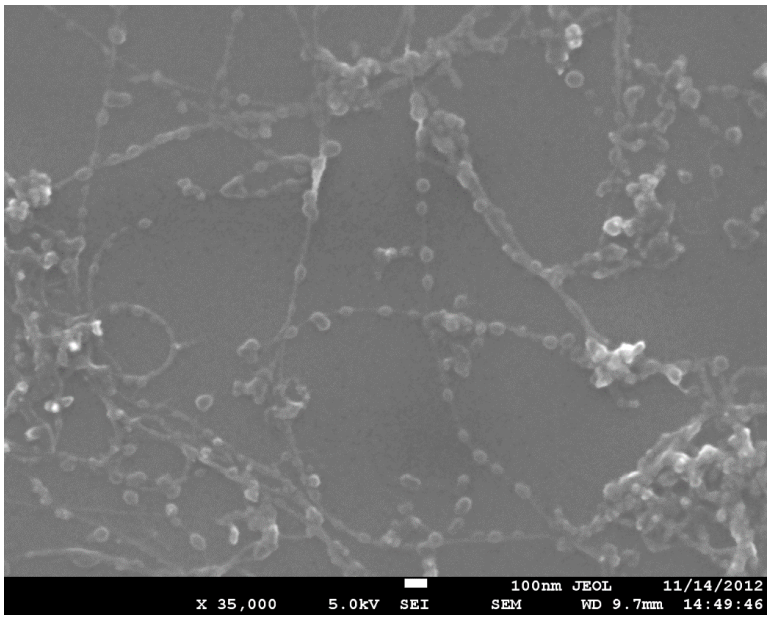

Figure 5.20: SEM image of metal incorporated of SWNT ropes after purification showing effective decoration of the outer walls of the SWNT ropes.

5.4.1 Raman spectroscopy studies

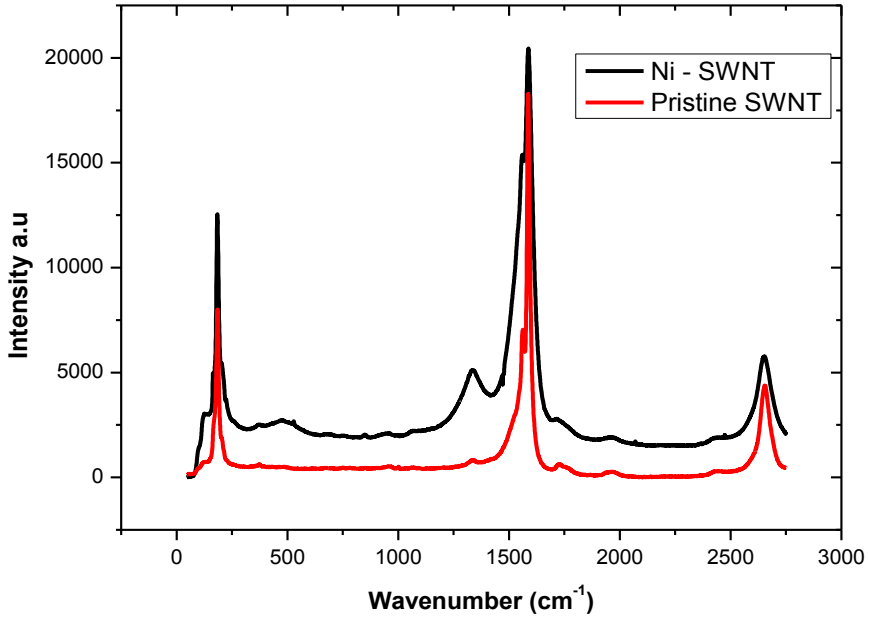

Figure 5.21: Raman Spectra of metal incorporated SWNT showing a slight shift in the G peak and RBM and an increase intensity of the D band due to metal incorporation.

The Raman spectra of nickel incorporated (Ni-SWNTs) composites shows a change in the RBM frequency profile. The spectra for the Ni-SWNT composite taken for a sample prepared at 200 ^{o}C for 7 days, shifts in RBM-peaks at 200 and 228 cm^{-1}. This implies a diameter change which might be due to doping of the SWNT due to metal incorporation but we do not have enough information to conclude this. There is also an increase in intensity of the *D* peak due to the disorder introduced during metal incorporation. Annealing the nickel decorated nanotubes caused the Raman peaks to have much higher intensity, possibly because the heat annealed the nickel onto nanotubes, eliminating some of the defects. The position and profile of the G band shows a clear splitting for the Ni-SWNTs into G^{+} and G^{-} which confirms doping of the nanotubes due to metal incorporation.

5.4.2 Electronic transport studies

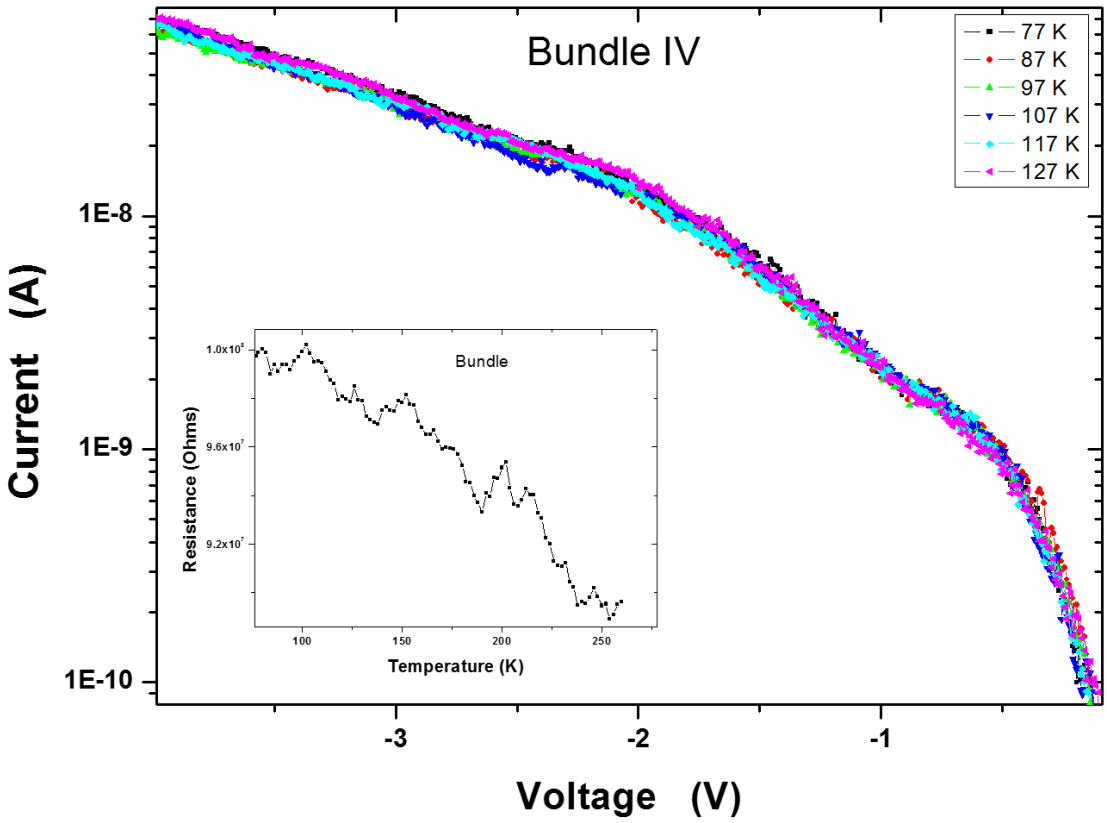

Figure 5.22: ***I-V*** **curve for metal incorporated SWNT bundle. Inset showing** ***R-T*** **of metal incorporated SWNT bundle exhibiting** T^2 **temperature dependence**

The bundle of tubes exhibits semi metallic behavior with a T^2 temperature dependence. This is characteristic of highly disordered metallic systems. A very small energy gap has been observed in the *I-V* characteristics of these samples which shows step like features related to resonant tunneling phenomena. The metallic nature maybe attributed to the Ni decoration which becomes more pronounced for a bundle complemented by the Raman analysis which also reports doping.

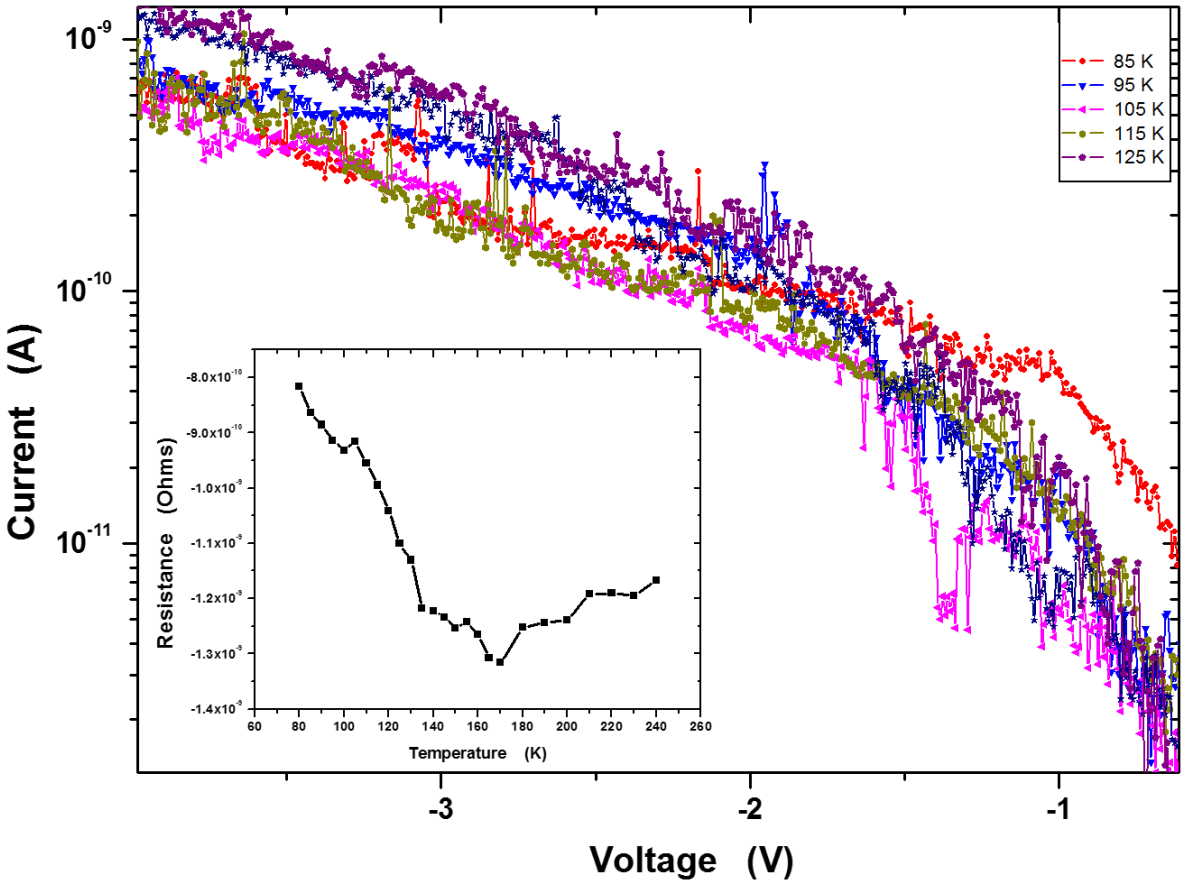

Figure 5.23: ***I-V*** **of individual metal incorporated SWNTs exhibiting non-exponential features. Inset showing** ***R-T*** **for individual SWNT showing a transition from metallic to semiconducting respectively as seen for pure nanotubes.**

Individual SWNT ropes showed a metallic nature from 300 K down to 140 K and a weakly activated conduction at low temperatures, below 140 K complemented by the non-exponential *I-V* characteristics. This is characteristic of highly disordered low dimensional systems where the constructive interference of elastically backscattered electronic wave functions increases the resistance at low temperatures. This may be due to the metal incorporation which introduces disorder to the SWNT rope. As the temperature increases the electron wave function is inelastically scattered by phonons thereby destroying the coherence of the backscattered wave functions which overturns the increase in resistance.

This study can be used to develop an understanding of the metal-nanotube interaction and the overall effect of the incorporated material on the electronic and magnetic properties of SWNTs.

5.5 Conclusion

In this study we optimized the synthesis process to produce high quality SWNTs and investigated their electronic properties in different geometries. The morphology studies showed the effects of the different process parameters on the yield and quality of SWNT produced. Effective separation of the SWNT into ropes was shown through microscopy studies. Most of the nanotubes were found as ropes ~20 nm diameter implying implies that the inter-tubular interaction within the individual SWNTs might be significant.

The dominant conduction mechanism within a mat of SWNTs is 3D variable range hopping where the electrons hop within the outer walls of the 1D structures. From the MR studies we determined the weak scattering limit and a localization length of 23 nm for the SWNT mat. It is also clear that for a mat the Coulomb blockade is not significant. Metal incorporation of aligned tubes changes the bulk properties of the material and not the individual properties as seen from the measurements presented above. When the metal is not in the inner core of the 1D structure its electronic properties remain unchanged. The bulk properties of bundled tubes are changed due to the fact that the predominant conduction mechanism in bulk is hopping hence the presence of the metal contribute to electron propagation.

Hence devices made from single walled carbon nanotubes mats are realizable and promise good results as seen from this work. Further work can be done by varying the thickness of the mat. Metal incorporation is not effective for individual SWNT geometries but evident in bundled but still requires further optimization for uniform incorporation and controllable adherence of the metal onto within single nanotubes.

6 Luttinger Liquid behaviour in single walled carbon nanotube ropes

6.1 Introduction

The dimensionality of a system plays an important role in determining the extent of electron-electron interactions which become more pronounced in reduced dimensions. 1D interacting electron systems are expected to behave differently from their higher dimensional counterparts. The significance of Coulomb interactions strongly modifies its properties resulting in non- Fermi liquid (FL) behavior, a state known as Tomonaga-Luttinger liquid (TLL). This model was proposed to explain electronic transport in 1D systems where the Fermi liquid model was inapplicable due to confinement as a result of reduced size effects. In this section we present measurements of the conductance of aligned SWNTs as a function of temperature and applied voltage which agree with the predictions for tunneling into a TLL system. The differential conductance of the devices fabricated from aligned SWNT ropes conforms to the power law behavior which is also in good agreement with the predicted TLL theoretical value and scaling of the devices differential conductance. Furthermore high frequency studies complement this finding to verify the existence of the TLL state in our devices.

6.1.1 Luttinger liquid model

The discussion given in section 2.5 was derived from a FL picture of interacting electrons in low dimensional systems. However electrons in 1D metals represent a TLL [**30**] where the interactions are enhanced, in contrast to a Fermi liquid (FL) [**31**], which is characteristic in 3-dimensional (3D) and 2D metals where electrons can be treated quasi-independently as shown in Figure 6.1. The FL theory precisely predicts the quantization of conductance in narrow channels but it does not consider

several major realisations.

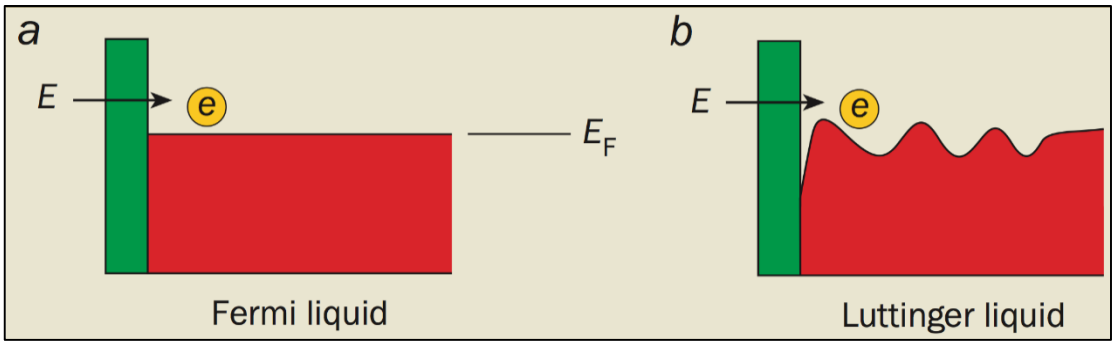

Figure 6.1: **Electrons in one dimension (a) illustration of an electron tunneling through a Fermi liquid from a metal electrode leaving the other electrons in the system undisturbed (b) Electron tunneling through a Luttinger liquid has to overcome the collective excitations from the electrons within the system [**119**].**

Unlike the "metallic" picture of the Fermi liquid model of excitations in the locality of the Fermi level, the electronic properties of electrons confined to 1D can be considered as collective excitations of charge density and spin density waves propagating at different velocities as illustrated in the Figure 6.2. The Peierls gap in the energy spectrum arises due to nesting of the Fermi surface at $2\overrightarrow{k_f}$ leads, when the $\pm\vec{k}$ states are connected adiabatically by electron-electron interactions [**120**]. The charge density wave possesses a plasmonic nature and propagates at a velocity determined by the strength of the interaction with some external perturbation. The spin density waves propagate at a velocity that can be approximated to be equal to the unperturbed Fermi velocity [**121**].

As a result, the states which are closest to the Fermi energy i.e. quasi-stable eigenstates known as the quasiparticle lifetime in Fermi liquid theory, $(E - E_F)^{-2}$vanish. In this sense, the quasiparticle excitations of the Fermi liquid no longer adequately describe the dynamics of the system. Instead, the TLL model derived from the low-energy dynamics of the system, found that the excitations

could be modelled as exactly soluble collective bosonic modes [**30**]. The model shows that the presence of electron-electron interactions in a 1D system renormalizes various energy scaling's and even the conductance quantum by a microscopically derived "Luttinger parameter." A more formal and thorough treatment of the topic can be found in literature [**122**].

Strange things happen when there is a shortage of space. The Pauli Exclusion Principle is well known for its effect on fermions, but bosons (for instance, photons) also behave interestingly when pressed for space. For this reason, researchers are very interested in schemes that create this kind of environment, in search of new physics and new technologies. One of these schemes is outlined by Dimitris Angelakis *et al* [**123**] propose an intriguing theoretical scenario in which photons in a spatially confined nonlinear optical medium take on the characteristics of a strongly correlated one-dimensional system of interacting fermions, mimicking a Luttinger liquid. In the Luttinger liquid regime, which can occur for fermions in one-dimensional systems, excitations of the fermions take on a bosonic character. Here, the scenario is essentially the reverse—bosons take on a fermion like character. The scheme relies on a one-dimensional hollow fiber acting as a waveguide (Figure 6.2), into which two atomic species are loaded and subjected to multiple laser fields. Exploiting the method of electromagnetically induced transparency (a technique that renders the medium transparent over a narrow frequency range and leads to extreme dispersion), different laser frequencies are tuned to create strongly interacting light-matter excitations known as polaritons. Angelakis *et al* have shown that polaritons can mimic highly tunable (variable interaction strength) Luttinger liquid behavior in the regime of effective repulsive interactions. This regime is experimentally accessible for realistic conditions.

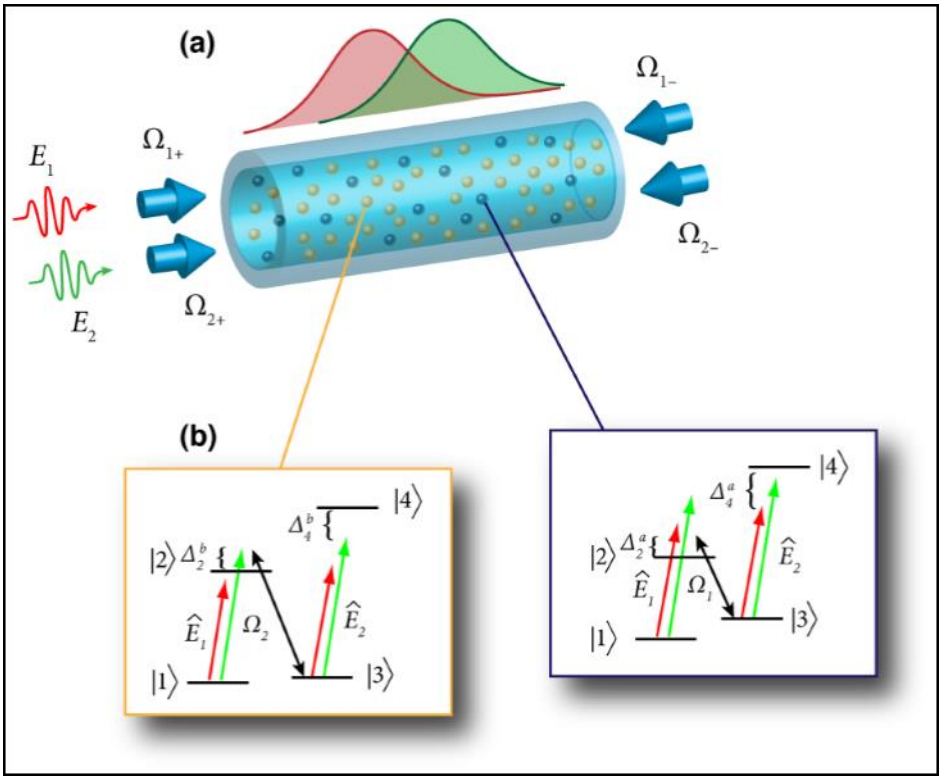

Figure 6.2: Schematic of the device. Two different species (yellow and blue) populate the waveguide. Two counter propagating quantum light fields (*E*) and two classical control beams (Ω) create spin and charge separation, represented by the red and green wavefronts above the waveguide. (b) Energy level diagrams for the two species of atom. Four atomic levels are exploited for optimal tunablility. The strongly interacting polariton gas is created by shifting in the fourth level after a pulse of photons enters the fiber [123**].**

Introducing an electron into a TLL system incomparable to excitation of a collection of one-dimensional plasmons and hence it is termed a "Liquid" due to the significance of the interactions. The formation of these plasmons leads to the evolution of high frequency properties and performance of SWNT based devices, extending their applications for high speed nano-optoelectronic devices and spintronic devices.

The results observed in this study for electronic transport in a rope of SWNTs conform to the TLL state as will be shown in the subsections that follow. The TLL state is an elusive phenomenon to observe experimentally. Before it is observed

there are conditions to be satisfied namely; low defect conduction path, the length of the conductor should be approximately the same as the electron mean free path and the device geometry should possess a low contact resistance. In this study these conditions are satisfied due the high quality material synthesized by pulsed laser ablation.

The TLL model is applicable when the Fermi liquid model breaks down (in certain instances). Non-Fermi liquid behavior is observed in the devices' differential conductance as illustrated in Figure 6.1. Electrons tunneling into a LL produce a power-law dependence of the conductance on both temperature and bias voltage which is dependent of the energy regime. The dependence of the current on the electric field and temperature is predicted to follow a universal scaling behaviour such that the curves collapse to one, when parameterized by Equation 6.1 in Ref [**124**,**35**];

$$\boldsymbol{J = I_0 T^{\alpha+1} \sinh\left(\frac{eV_s}{2k_BT}\right) . \left|\Gamma\left(1 + \frac{\alpha}{2} + i\frac{eV_s}{2\pi k_BT}\right)\right|} \qquad \textbf{6.1}$$

where I_0 is a constant, e the electron charge, k_B is the Boltzmann constant, $\Gamma(x)$ the gamma function, and V_S *is* the voltage drop over a single CNT. In our sample geometry the distance between the external sample contacts L (see Figure 6.3) is much larger than the average length l_{ef} between intertube contacts. Under these conditions the expression for V_S can be written

$$\mathbf{V_s = \frac{l_{ef}}{L}\gamma V} \qquad \textbf{6.2}$$

where V is the voltage drop over the sample and γ is a parameter. Equation 6.1 has two asymptotic behaviors as follows:

(a) In the low field limit, $eV_s/k_BT < 1$ and Eqn. 6.1αreduces to $J/V \sim G \propto T^{\alpha}$,
(b) In the high field limit, $eVs/k_BT > 1$, resulting in $J \propto V^{1+\alpha}$.

The exponent α can thus be deduced in two independent ways from experiments carried out in the two limiting cases. The exponent depends on the number of one dimensional channels and whether the electrons from the Fermi liquid tunnels into the end or bulk of the TLL. The device geometry used (nanotube on electrodes) in this work allows for bulk tunneling. Such that the exponent is;

$$\boldsymbol{\alpha = (g^{-1} + g - 2)/8} \qquad \textbf{6.3}$$

where **g** is the TLL parameter which is determined by the strength of the e-e interactions.

6.2 Electronic transport in single walled carbon nanotube ropes

6.2.1 Di-electrophoresis process optimization

The devices for electronic transport were fabricated by DEP as described in Section 4.3.1. The process had to be optimized of proper alignment of the SWNTs. The critical parameters for DEP are the frequency, voltage applied and the solvent used to disperse the SWNTs.

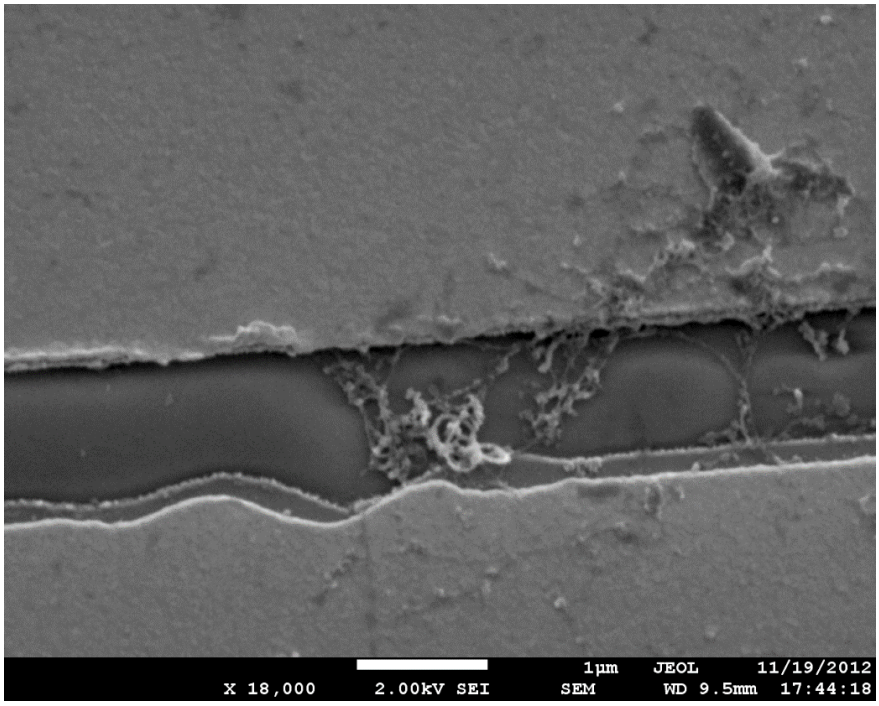

Figure 6.3: DEP aligned SWNT ropes at a voltage below 5 V p-p showing nanotubes bundled up across the gap.

Figure 6.3 shows the material aligned before optimization when voltage was below 5 V p-p. The SWNTs are bundled up at low voltage hence 5 V is the appropriate voltage for alignment. Figure 6.4 shows SWNTs aligned at frequencies above 1 MHz the nanotubes tend to burn at such high frequencies.

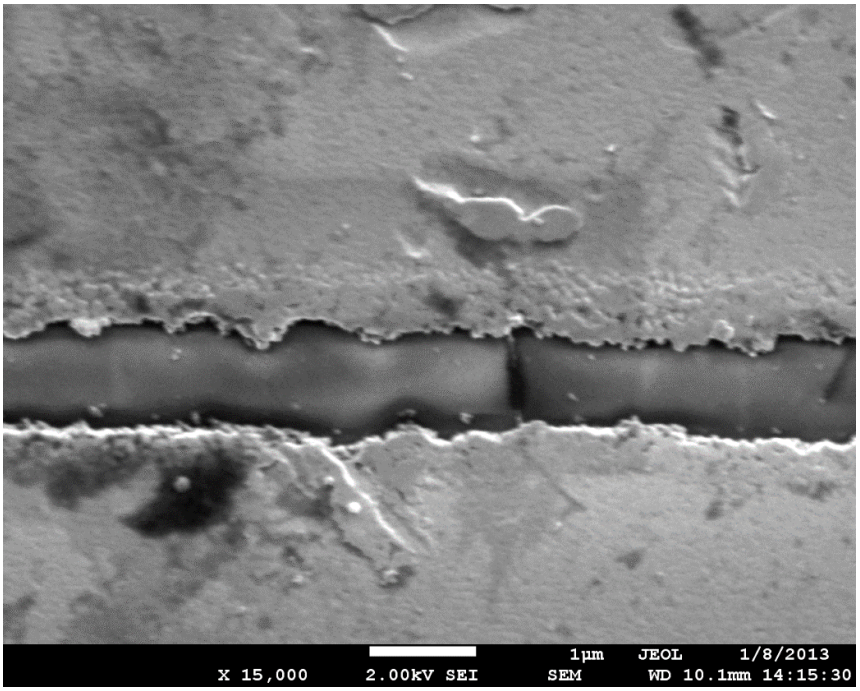

Figure 6.4: SWNT ropes aligned by DEP at a frequency greater than 1 MHz showing nanotubes burning.

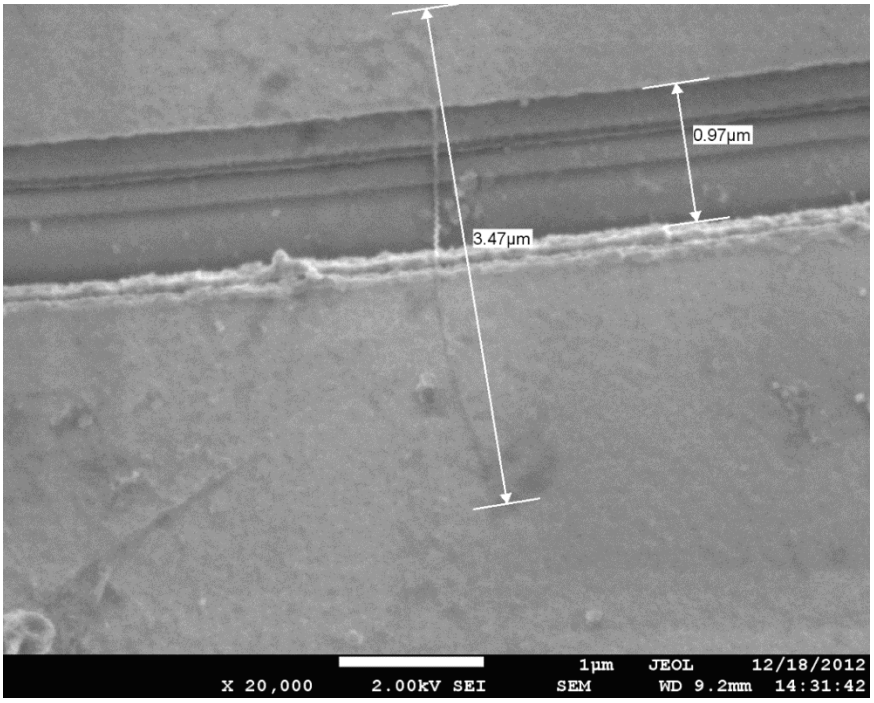

Figure 6.5: SEM of efficiently aligned SWNT ropes at optimized condition; 1 MHz and 5 V p-p voltage. The length of nanotube rope is large compared to the gap between the electrodes.

Efficient alignment of the SWNT ropes was achieved with an alternating current at 5 V p-p and frequency of 1 MHz using DMF as a solvent as shown in Figure 6.5

6.2.2 Current voltage characteristics

Figure 6.6 a- c shows SEM images of the devices resulting from the DEP process after optimization. The images show multiple and a few ropes of SWNT s aligned across the 1 µm gaps across the gold micro-electrodes illustrated in Figure 4.. The morphology was dependent on the concentration of the SWNT in the solution used and the exposure time was kept constant. Figure 6.3d is a sketch showing that the devices were fabricated within the requirements of the TLL model were the length of the conductor $L >> d_t$, the diameter of the SWNT rope.

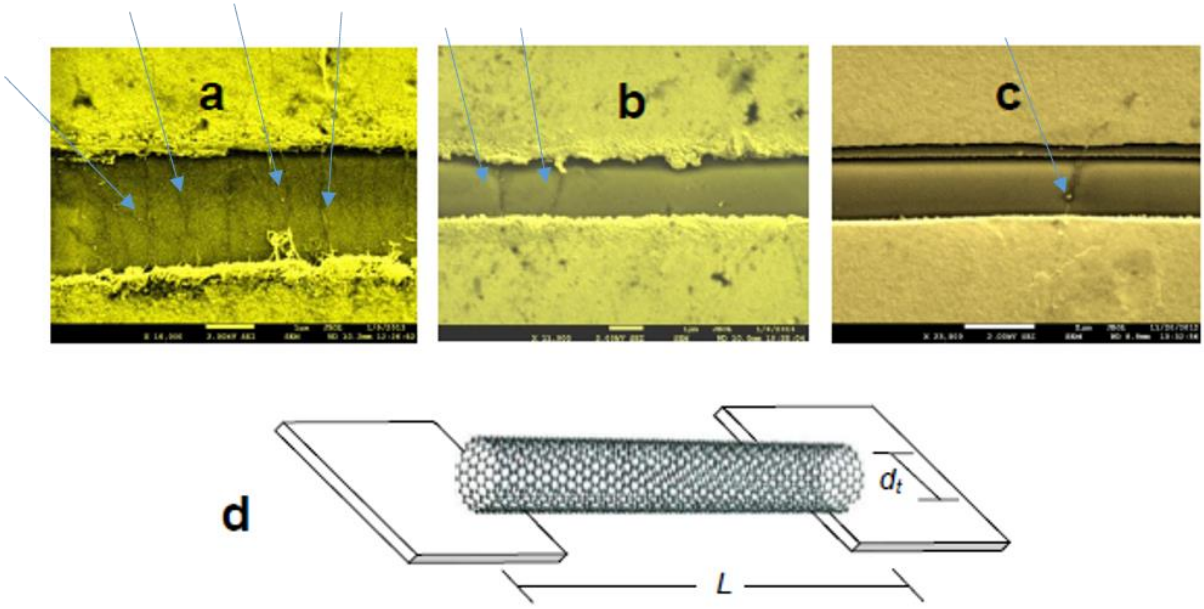

Figure 6.6: **(a-c) Di-electrophoresis aligned SWNT ropes (diameter d_t~ 20 nm) shown by the blue arrows spanning an inter-electrode gap of L ~ 1 µm between gold electrodes. (d) Sketch showing the 1D model satisfying the condition $d_t << L$**

For all the devices fabricated by DEP the current-voltage characteristics traced on the B1500A semiconductor analyser exhibited no significant asymmetry or any rectification effects in the 70-290 K temperature range as shown in Figure 6.7, indicating that the Schottky barrier effects associated with potential barriers at the metal-SWNT interface do not play a pivotal role in the devices' electronic transport characteristics. This is due to the fact that DEP favours the alignment of metallic SWNTs which are less susceptible to Schottky barrier effects [**79**].

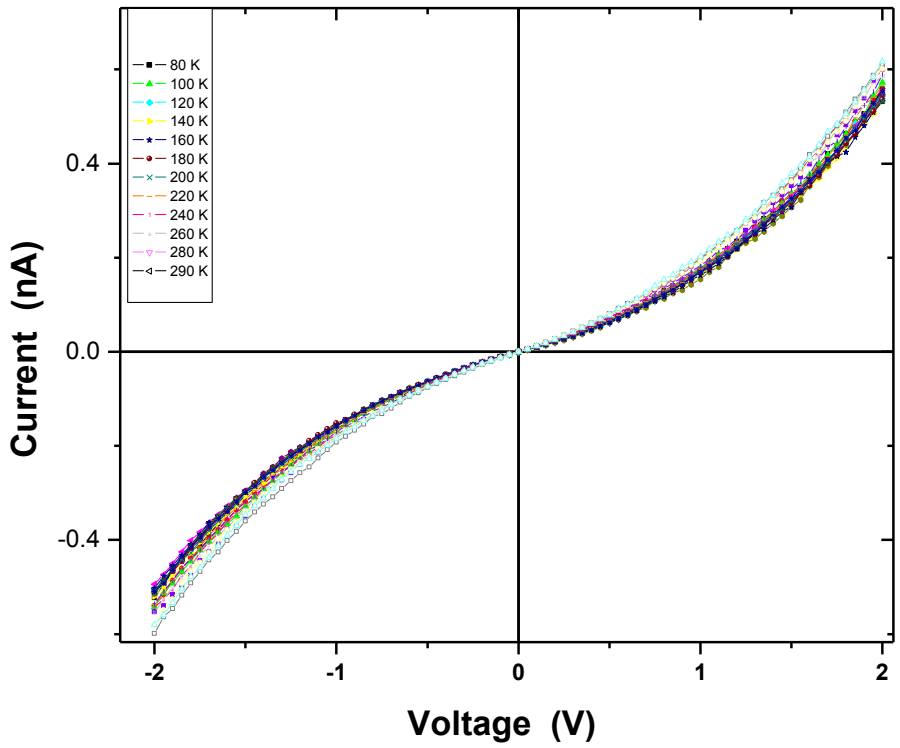

Figure 6.7: Typical I-V characteristics for a few ropes of nanotubes aligned across a 1 µm gap between two gold electrical contacts for temperature range 80 to 290 K

6.2.3 Conductance of aligned SWNT ropes

Temperature dependent *I-V* data from the two probe configuration (Figure 6.7) was used to deduce the resistance - temperature (*R-T*) dependence for the devices. Figure 6.8 data shows a metal-insulator transition from room temperature to 77 K at different potentials. The crossover occurs around 150 K which has been reported before for a single rope [**86**] as shown in Figure 6.8. Such metal-insulator transitions have been widely studied in the context of disordered metals [**125**,**126**,**127**].

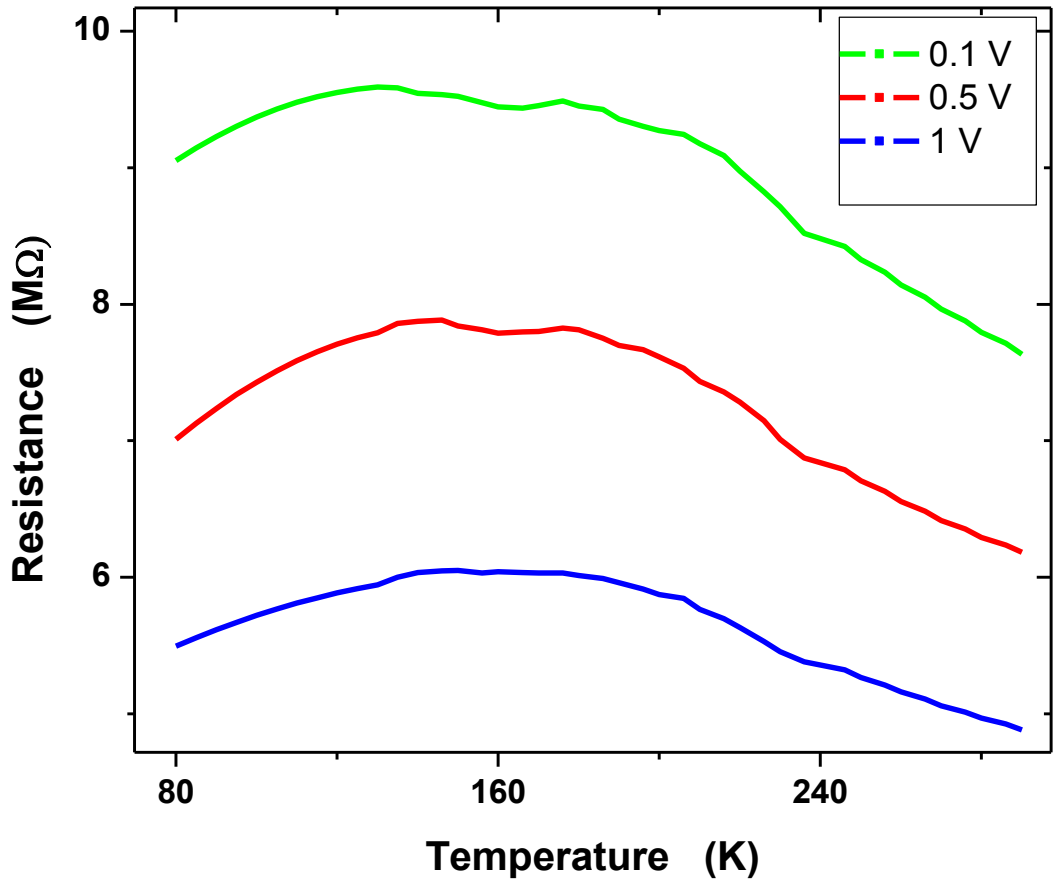

Figure 6.8 : **Resistance-temperature dependence of SWNT ropes at different voltages showing a metal insulator transition as the temperature is increased from 77 K to 300 K and a decrease in resistance as the potential is increased.**

This can be explained within the Ziman theory with the scattering term of the Boltzmann Transport Equation extended to include the structure factor which is invoked to determine the scattering probability. The contribution of inelastic scattering increases the resistance with temperature while elastic scattering reduces the resistance with increasing temperature due to the temperature dependence of the Debye-Waller factor [**128**]. These two competing phenomena result in the metal-

insulator transition. This analysis is applicable to the present study since transport occurs predominantly through metallic tubes [**129**] where there are local defects such as kinks in the tubes and intertube contacts. For an aligned rope of tubes potential barriers are introduced by tubes with different electronic structures that make up a rope and inter rope contacts shown in the TEM image, Figure 5.9.

6.2.4 Differential Conductance

As we are interested in features due to electronic degrees of freedom careful data analysis was needed because transport data can be affected by many factors. Plotting the graph of differential conductance against applied voltage (for the same device that the *I-V* characterization was done on), which fingerprints electronic properties of the molecular device; our data clearly shows differential conductance fluctuations with voltage at different temperatures. The outstanding feature of these curves is the deviation from Fermi liquid behavior where the tunneling rate into a clean 3D metal is featureless i.e. neither suppressed nor enhanced at zero bias resulting in unimpeded creation of electrons or holes close to the Fermi surface even as temperature is increased. We found direct evidence of the existence of a TLL from 77 K up to 290 K. This is discussed in the following text.

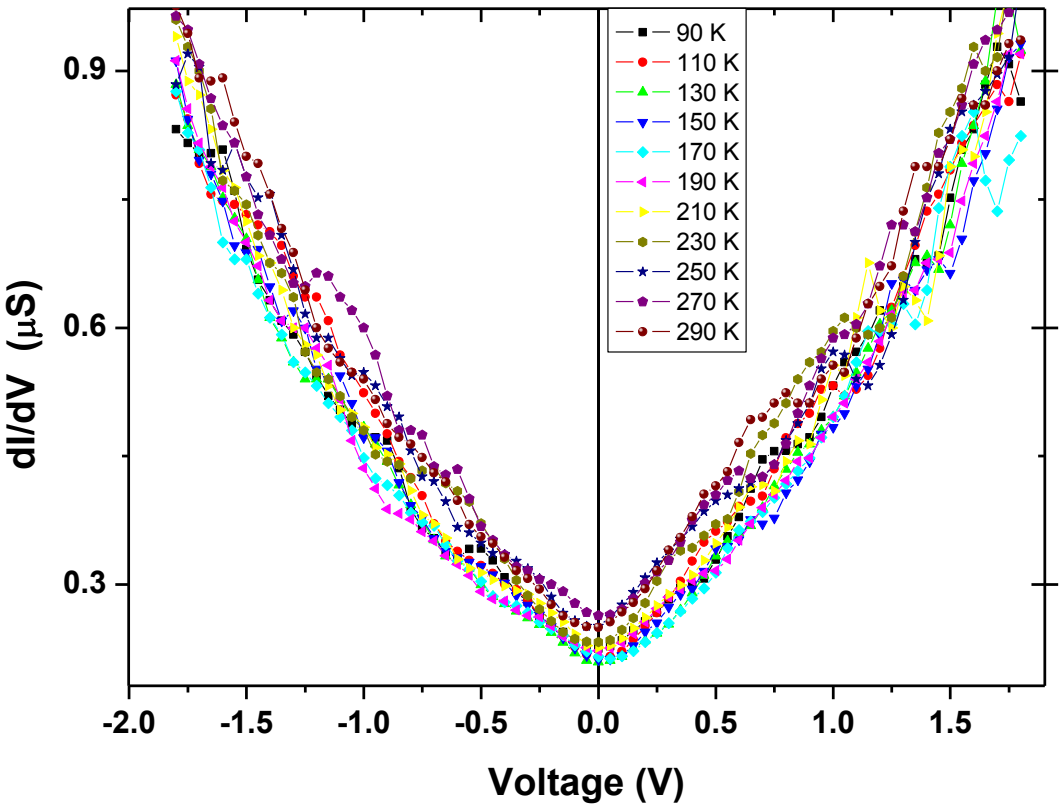

Figure 6.9: Differential Conductance against bias voltage from 77 K to 290 K exhibiting deviation from Fermi liquid behavior

We note that the differential conductivity decreases for very low applied bias, consistent with TLL behavior. In a Fermi liquid the differential conductivity is expected to remain constant because the conductivity is a material characteristic. We did not observe saturation of differential conductivity in our devices. Our data, Figure 6.9 clearly shows differential conductance fluctuations with voltage at different temperatures.

The differential conductance exhibits a slight temperature dependence from 80 – 290 K complementing the overlapping *I-V* curves (Figure 6.7). In this regime the

conduction is suppressed due to coulomb blockade when the applied potential is less than the charging energy as discussed in section 2.5.2. Once the CB regime is overcome the plasmonic quantized charge conduction dominates. The CB smears out the effect of power law behavior of the conductance at low biases. From calculation the CB effect is in the low field limit ($V_s < \frac{k_B T}{e}$) with T=77 K, V_s= 6.6 mV, hence these devices can be considered to be operational within the high bias regime ($J \propto V^{1+\alpha}$).

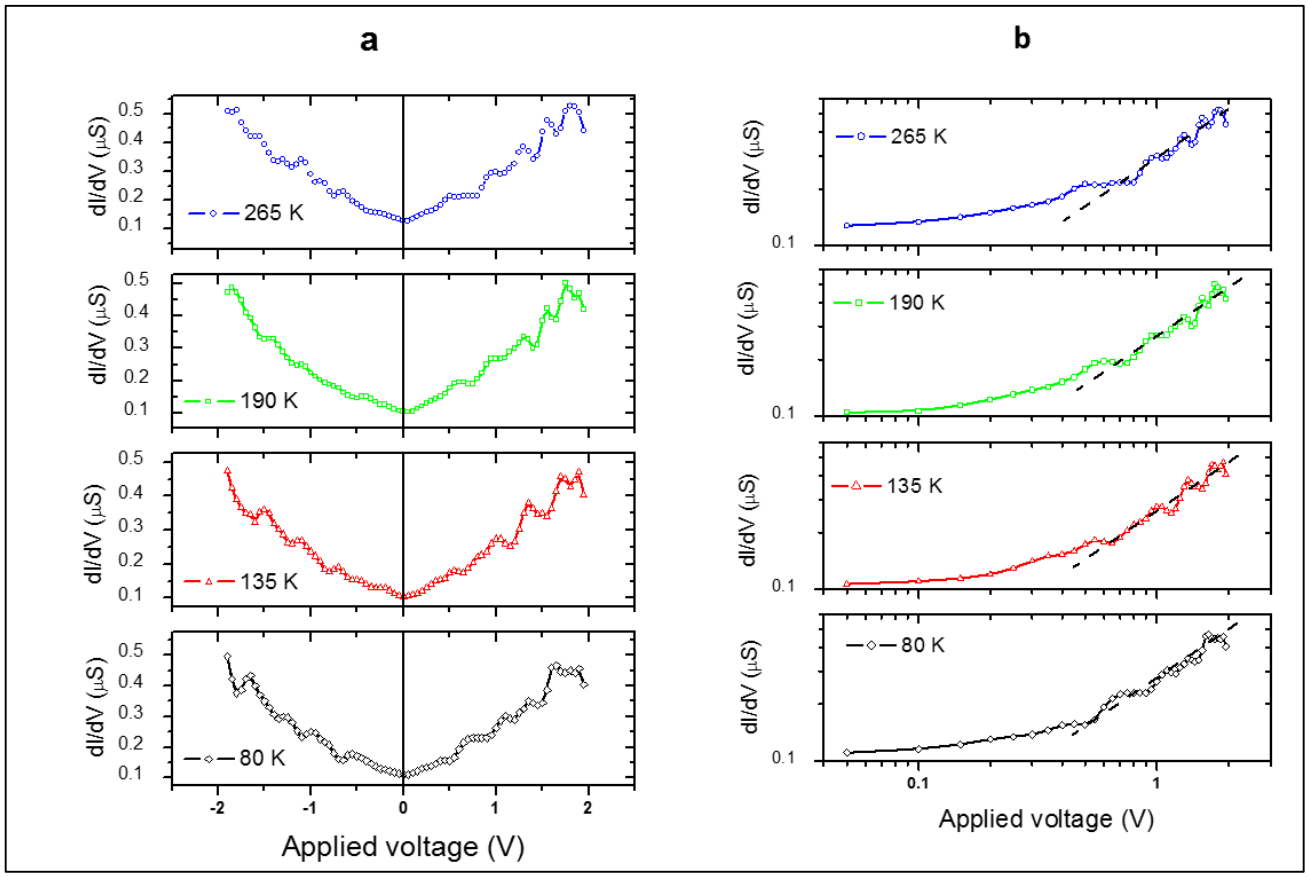

Figure 6.10: **(a) Differential conductance as a function of applied bias voltage for SWNT ropes. Quantum leaps of differential conductance are evidence of discrete conducting channels situated at different energy levels. The decrease of the differential conductance around zero bias is associated with the Coulomb blockade. (b) Double log plots show the power laws with slope (dashed lines) α ~ 0.45. The lower slope is related to Ohm's law of slope = 1.**

A careful analysis of individual curves at different temperatures as shown in Figure 6.9 yields and Figure 6.10 above clearly showing that the curves exhibit step like features in the differential conductance which is indication of quantized charge conduction in multiples of the universal value $G_o \sim 2e^2/h$. The curves exhibit step like features in the differential conductance in the higher bias regime with a slope ~ 0.45. This is an indication of quantized charge conduction which can explained by considering the plasmonic nature of the charge carriers in a TLL [**130**] propagating at different velocities dependent on the strength of the interaction [**35**]. Increase in voltage is akin to increasing the charging across the 1D SWNT capacitors. When a transport channel is encountered at energy $E + \Delta E$, the charge quantum is released giving rise to increased conductance as voltage is increased. Once the channel has been super ceded by the voltage, again the conductance is suppressed, leading to constant conductance (flattened regions in the *dI/dV* curves) with a power law dependence to the voltage. The steps are flat at low biases and sloped at higher biases which shows that the conductance is not dependent on the electron density at low biases i.e. in the Coulomb blockade regime and depends on the electron density at higher biases. The step sizes shows a degree of correlation on different scales which may be due there being multiple plasmons involved in the transport as a result of several conducting tubes within a rope. Hence we have described the experiments on plasmon propagation across aligned metallic SWNTs across a 1 μm gap between two gold electrodes which will be explained in the sections that follow.

6.3 Luttinger liquid behaviour in SWNT ropes

It has been pointed out that an indication of the TLL behaviour of a system is the scaling behaviour of a devices' differential conductance. Figure 6.11 is a plot of the

data obtained experimentally showing a relationship $\left[\frac{dI}{dV}(V,T) \propto V^{\alpha}\right]$, derived from Equation 6.1; hence a TLL state is implied.

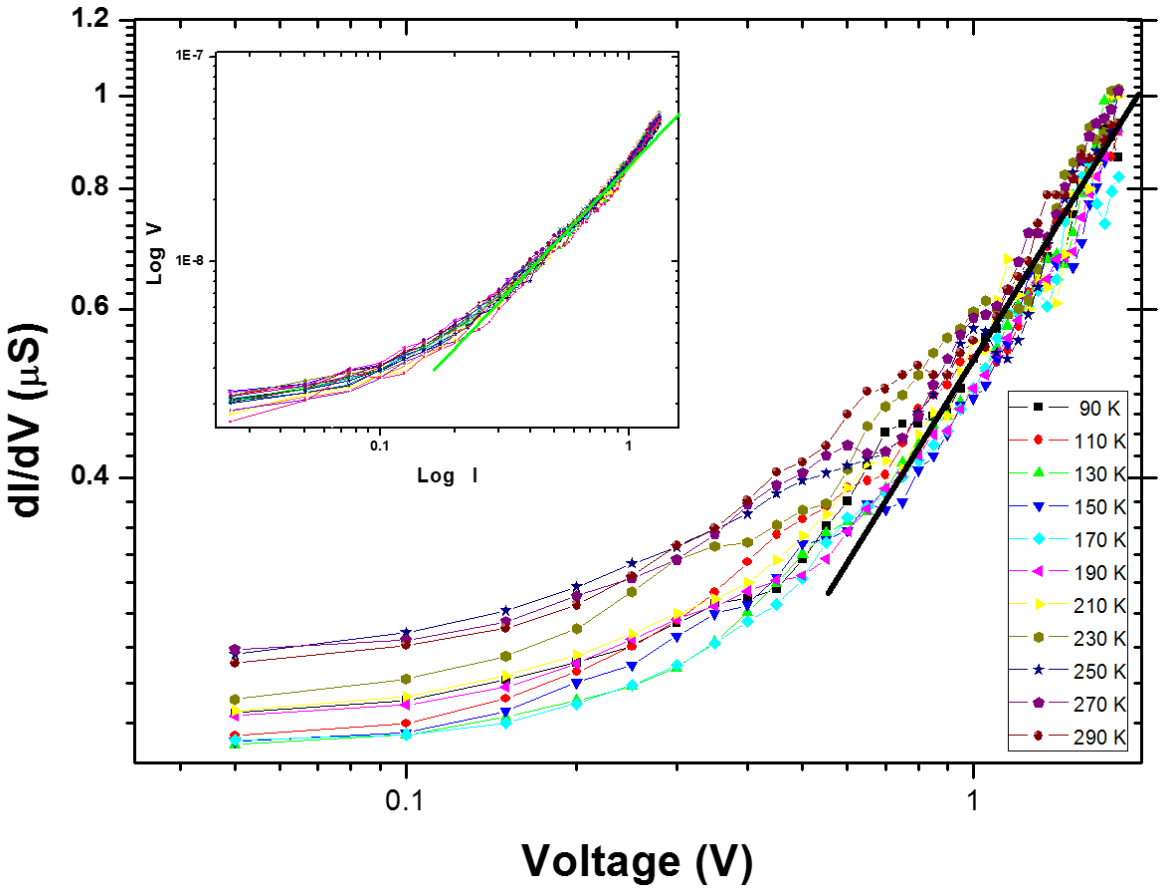

Figure 6.11: Differential conductance against voltage showing scaling of the differential conductance in the high field limit as predicted by the TLL theory. Inset I-V double log plot shows the same power law in the high field limit

The curves at different temperatures collapse into a single curve at higher biases as predicted by the scaling equation where the exponent α can be determined from the gradient. The bias voltage dependence on differential conductance for the SWNT ropes is attributed to the suppressed tunnelling DOS in the TLL system. The exponent α depends on the number of channels available for conduction, electron-electron interaction strength, and the device geometry. The exponent was calculated

to be 0.45 in this study from the slope of the graph, as predicted by theory for our device geometry i.e. bulk [**35**]. The inset in Figure 6.11 shows a transition from Ohmic in the low field limit, to the power–law exponent in the high field as V increases, as predicted by the theory.

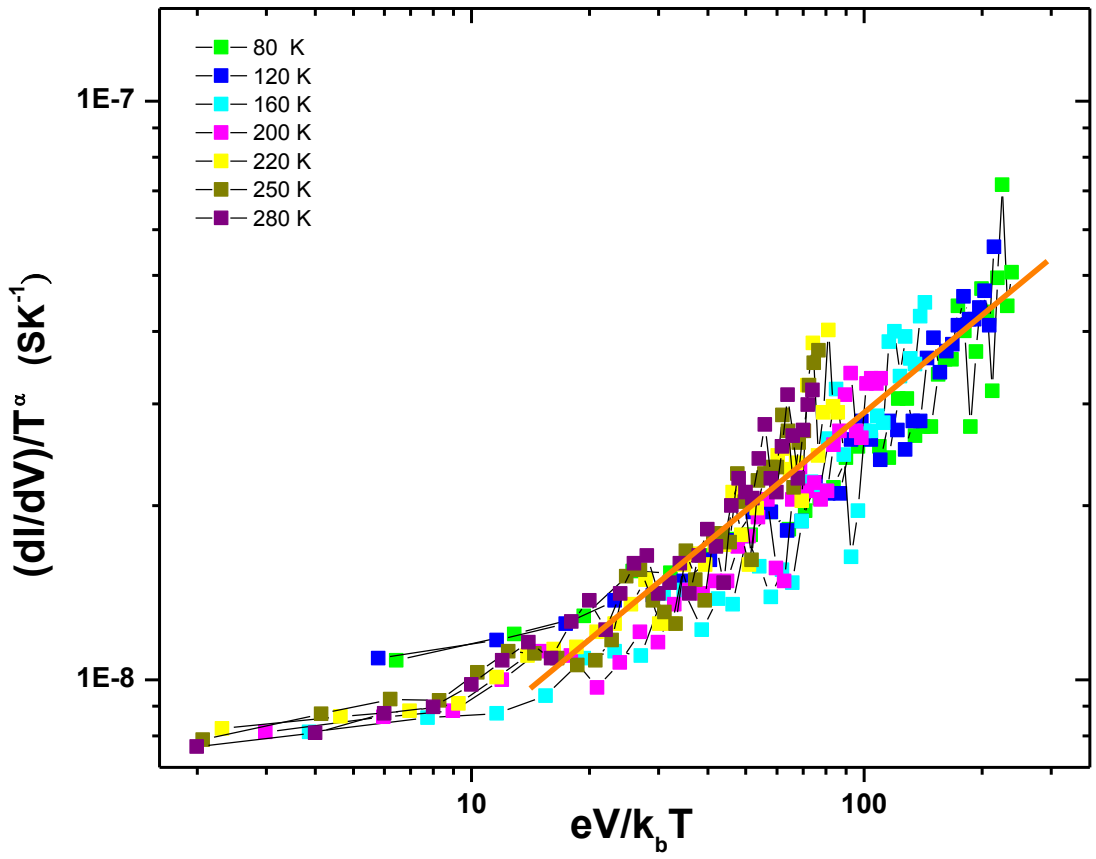

Figure 6.12: Collapsed curves in universal scaling coordinates, when scaled using the power law exponent the curves at different temperatures roughly collapse to one as predicted by Luttinger liquid theory; Eqn. 6.1

Figure 6.12 is a plot derived from the scaling Eqn. 6.1. It confirms the theoretical prediction of the TLL theory of the collapse of the devices differential conductance

at different temperatures when plotted in the universal coordinates. The set of measurements presented above show the possibility of TLL behavior for devices made from ropes of aligned SWNTs. We extend this study by measuring the high frequency response of the same device at room temperature. We also investigate for the possibility of TLL excitation in these devices. The performance of the devices depends critically on the contact resistance. The method is described below.

6.4 Frequency response studies

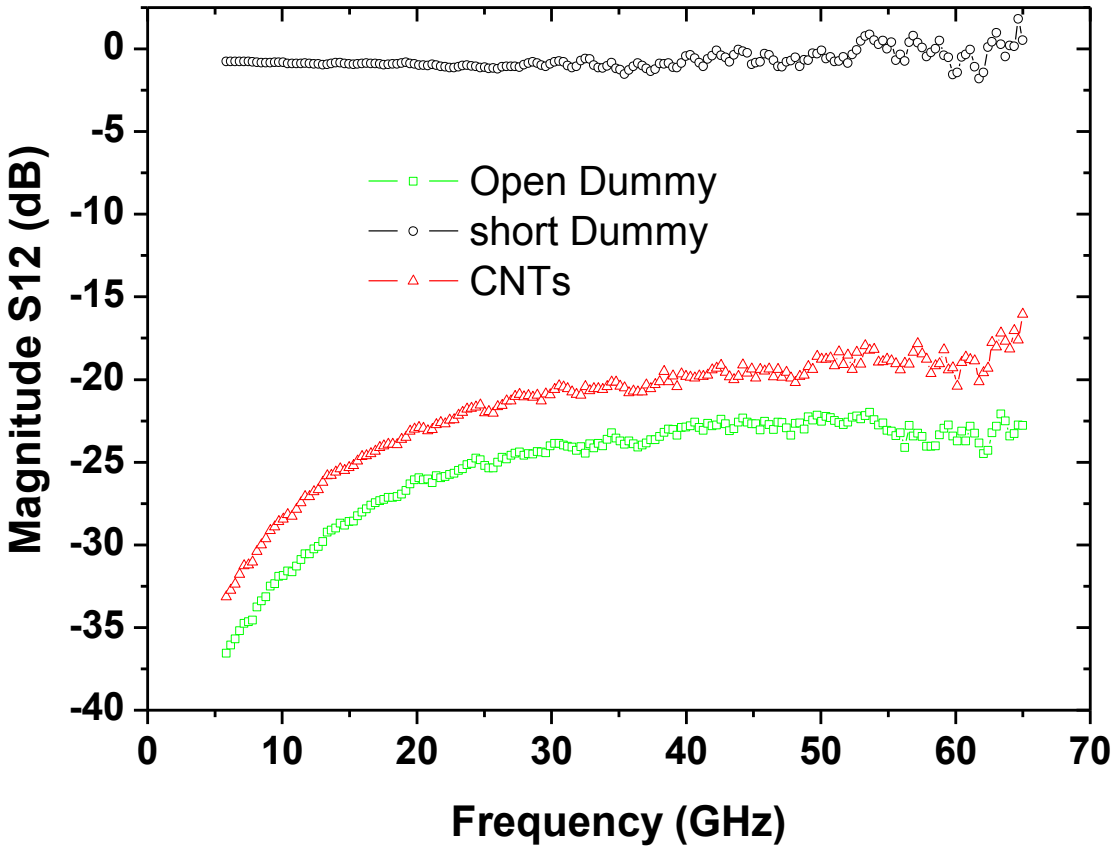

Figure 6.13: Scattering parameters S_{12} showing the insertion loss in dB for SWNTs, open and short dummy waveguides.

The frequency response of device under test (DUT) (SWNT rope) data was obtained by converting the admittance (*Y*) to impedance (*Z.*) using standard conversion equations. Figure 6.13 clearly shows that about 3 to 5 dB of the transmitted power (i.e. the difference between the Open and SWNT device) in the measured CPW devices can be attributed to SWNT ropes. The transmission capability increases with frequency and there is no indication of saturation showing that the transmission capability of SWNTs is well beyond 65 GHz. These results are complemented by the complex impedance data shown in Figure 6.14 below.

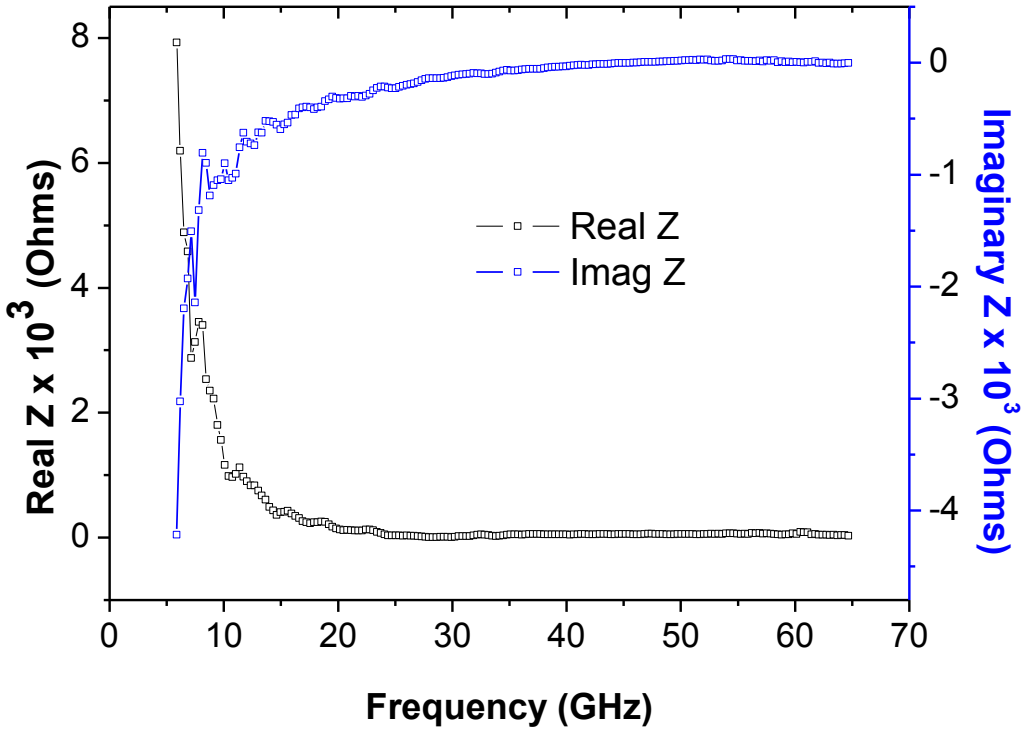

Figure 6.14: Real and Imaginary Impedance of SWNTs after de-embedding.

After de-embedding the parasitic effects using an industrial approved Open-Short technique [**68**], the complex impedance of the SWNTs is shown in Figure 6.14. The absolute value of the real and imaginary parts of the impedance decreases with

frequency indicating an increase in transmission. The imaginary component is predominately capacitive.

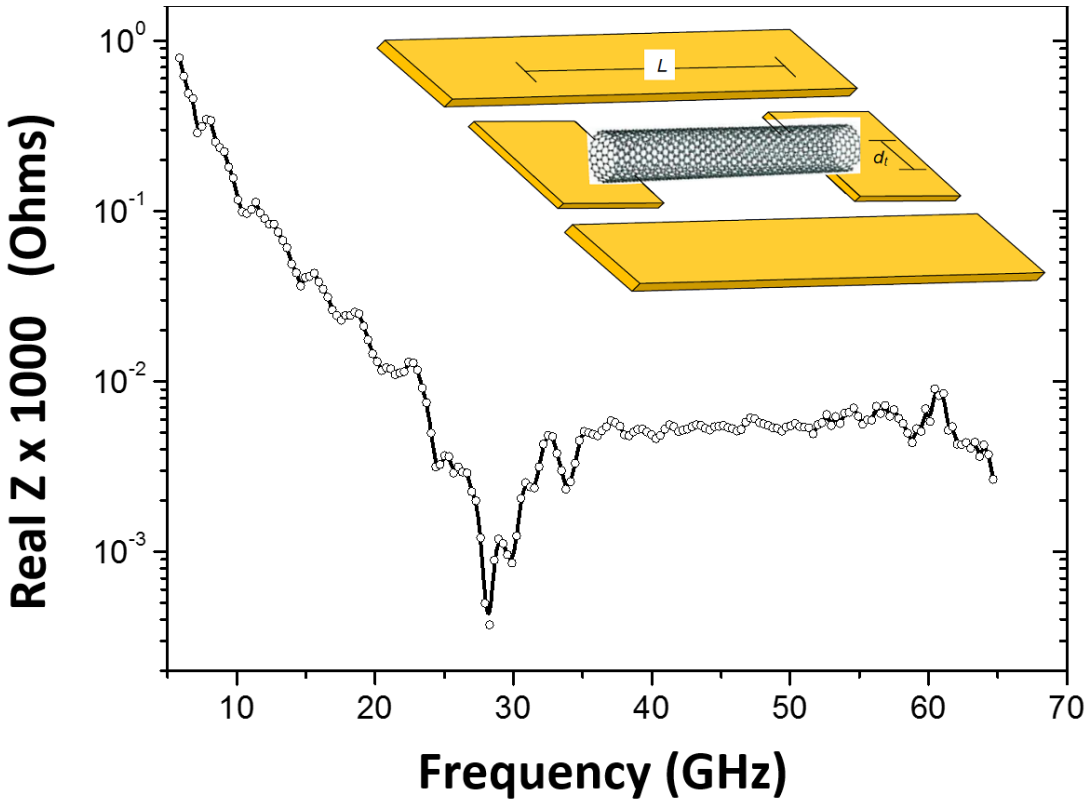

Figure 6.15: **Real Impedance of SWNTs showing and oscillatory response in the frequency range 6 to 30 GHz. Quantized conductance is consistent with TLL behavior. Impedance decreases with frequency up to 30 GHz; thereafter it increases to saturation more than 2 orders below the lowest frequency impedance value. The inset shows the device configuration employed**

A closer look at the complex impedance shows some oscillatory behavior in the frequency range 6 to 30 GHz, shown in Figure 6.15, such behavior has been predicted theoretically in the Luttinger Liquid model [**66**] and may be attributed to first, second, third, harmonic waves set by the finite length of the SWNTs. These resonant peaks appear to be damped as the frequency increases probably due to the

effect of contact resistance. Hence the simultaneous observation of the power law dependence and a non-trivial frequency dependence of impedance strongly supports the TLL theory.

6.5 Discussion

In this study we fabricated 1D devices using high quality SWNT ropes and observed non universal quantized conductance due to Luttinger liquid behavior. The geometry of the devices can be viewed as a 1D quantum wire coupled to two non-interacting Fermi leads. One of the fingerprints of a non-interacting 1D conductor is its quantized conductance. A perfectly contacted and clean SWNT is expected to have quantized conductance. The data clearly shows the existence Luttinger liquid behavior for devices made from ropes of aligned SWNTs from 77 K to room temperature. Differential conductance characteristics revealed TLL behavior for a wide temperature range of 77 to 290 K for these mesoscopic systems. Steps in the differential conductance confirmed quantized behavior, hence the propagation of plasmons undergoes quantum coherence at specific applied energies, and ballistic conductance occurs.

We were also able to show ropes of SWNTs are capable of transmitting electric signals through them, and that the frequency response also shows quantized conductance at low frequencies which becomes indiscernible at high frequencies as expected. The simultaneous observation of the power law dependence in the differential conductance and oscillations in the high frequency eliminates possibility of effects from environmental fluctuations confirming the TLL behavior Finally because of the observation of TLL behavior even with high contact resistances we propose that the SWNT nanotube ropes provide a better environment for the existence of a Luttinger liquid system compared to individual tubes and mats. We believe this can have far reaching consequences in the advancement of nanotechnology, leading to low dimensional fast switching devices.

7 Conclusions and recommendations

7.1 Synthesis of single walled carbon nanotubes

Single walled carbon nanotubes were synthesized by pulsed laser ablation and we found that the yield and morphology were closely related to the growth parameters. Both the gas parameters determined by the gas flow rate and pressure, and the thermal energy determined by the laser fluence and synthesis temperature affect yield and morphology of the synthesized material. A low flow rate and, or pressure affect the plume dynamics which determines the yield quality of material produced. If the fluence and temperature are both low, graphitic material is produced. If the fluence is low but the temperature is high enough low yield high defect SWNTs are produced. If the temperature is low and fluence is high still low yield high defect SWNTs are produced. We also found that not just the composition of the target mattered but the condition of the target also had a huge effect on the yield. Overtime, the target quality degrades due to damage of the surface by repetitive ablation and absorption of gaseous impurities. Hence it is recommended to always use a freshly annealed target. On the whole we optimized the laser ablation synthesis method for 532 nm, 10 Hz pulsed laser, in a tube of diameter 25 mm. High quality single walled carbon nanotubes were produced at a temperature of 1 373 K, Pressure 600 mbar, flow rate 200 sccm, laser fluence 860 mJ.

7.2 Electronic transport in single walled carbon nanotubes

We have investigated the evolution of the electronic transport properties of single walled carbon nanotubes starting with SWNT mats progressing to aligned metal incorporated SWNT ropes (bundles and individual) and finally aligned pristine SWNTs ropes. The study was done in order to interpret the transition from a 1D electronic transport channel to the 3D limit. Theoretically the electronic transport of the SWNT mat should give an idea of the individual nanotube properties. Our key conclusions are:

(i) From the combined study of R-T and M-R it is revealed that 3D VRH is dominant as the conduction mechanism in a nanoporous system composed of SWNT mats (bundled ropes) due to multi-channel effects. From the localization length, ~ 23 nm, it can be seen that VRH is between the ropes through the nanotube-bundle contacts in a mat. The SWNT mat forms a system of localized electrons where the electronic states are three dimensional with a radius much greater than the distance between intertube contacts as has been reported. This result is inconsistent with any model of localization in which the tube electrons are confined to a single tube or bundle. The carriers in an SWNT mat are in fact localized by disorder caused by intertube defects or deformations. Hence SWNT mat based devices have limited applications since the mean free path is minimized by scattering processes. This limits the device geometry for DC applications which is even more prominent in high frequency applications. Isolation of ropes from bundles minimizes the scattering due to lattice vibrations and gives detailed 1D quantum transport properties due to longer mean free path and longer coherence length. As the scattering is minimized the mobility is increased which makes the aligned rope devices a more reliable material. Aligning the ropes minimizes the effects of defect induced interactions arising due to interbundle interactions and extends the capability of the material to high frequency applications.

(ii) The metal incorporation did not change the properties of individual SWNT ropes but modified those of the bundle. Our recommendation is that to see the real effects of the metal on the electronic properties of SWNTs intercalation would be the best approach. The properties of filled SWNTs would be much more reliable compared to the incorporated and extend applications of the material to spintronic devices.

(iii) Our data for aligned SWNT ropes is consistent with the tunneling through an interfacial barrier into a Luttinger liquid, where the intrinsic barrier transmission probability is assumed to be energy dependent and the power law dependence arises from the suppression of the tunneling density of states near the Fermi level in the metallic SWNT or an environmental Coulomb blockade giving an equivalent behavior. Therefore multichannel effects from intertube interactions and other defects, are minimized in two-terminal devices fabricated by aligning SWNT (extracted from a mat). The effects of plasmon propagation, unique to one dimension, were identified in electronic transport of aligned ropes as a non-universal power law dependence of the differential conductance on temperature and source-drain voltage. The complex impedance showed high power transmission capabilities up to 65 GHz as well as oscillations in the frequency range up to 30 GHz. The measurements suggest that aligned SWNT ropes have a realistic potential for high speed device applications.

In conclusion we report the superiority of the electronic transport properties of SWNT ropes over SWNT mats verified from low temperature and frequency dependent transport measurements. The electronic transport properties of SWNTs evolve depending on the configuration. SWNT mats do not give an idea of the electronic transport properties of individual SWNT ropes. Coulomb interactions are more pronounced in individual SWNTs as compared to mats due to the large number of carriers in mats propagating on the outer walls of the nanotube ropes. This leads to the evolution of electronic transport from Luttinger liquid behavior to 3D variable range hopping. Metal incorporation does not alter the properties of the SWNTs significantly.

7.3 Future outlook

Much work has been done on individual SWNTs and mats, but ropes are less well studied. The devices fabricated from ropes exhibited interesting results which might counter the limitations of singular tube devices and the short comings of mats. The phenomena are not easy to explain but they merit further studies. This study can be extended to find the extent of the Coulomb interactions in the low field limit so as gain a better understanding of its significance on electron- electron interactions in 1D systems. Finding ways of synthesizing SWNTs of known diameter and chirality is also still an open problem that requires further investigation which would contribute immensely to device miniaturization.

References

1 M. F. L. De Volder, S. H. Tawfick, R. H. Baughman and A. J. Hart. *Science*, **339**, 535 (2013).

2 L. B. Hu, J. W. Choi, Y. Yang, S. Jeong, F. La Mantiaa, L. F. Cui and Y. Cui. *Proc. Nat. Acad. Sci*, **106**, 21490 (2009).

3 P. A. Williams, S. J. Papadakis, A. M. Patel, M. R. Falvo, S. Washburn and R. Superfine. *Appl. Phys. Lett*, **82**, 805 (2003).

4 M. C. Roco, C. A. Mirkin and M. C. Hersam. *J. Nanopart. Res*, **13**, 897 (2011).

5 F. Kreupl. *Nature*, **484**, 321 (2012).

6 S. J. Tans, A. R. M. Verschueren and C. Dekker. *Nature*, **393**, 49 (1998).

7 A. M. Ionescu and H. Riel. *Nature*, **479**, 329 (2011).

8 J. Appenzeller, Y. M. Lin, J. Knoch and P. Avouris. *Phys. Rev Lett*, **93**, 196805 (2004).

9 K. Jensen, J.Weldon, H. Garcia and A. Zettl. *Nano Lett*, **7**, 3508 (2007).

10 A. D. Franklin, M. Luisier, S. Han, G. Tulevski, C. M. Breslin, L. Gignac, M. S. Lundstrom, and W. Haensch. Nano Lett, **12**, 758 (2012).

11 C. Felser, G.H. Fecher and B. Balke. *Angew. Chem. Int. Ed*, **46**, 668 (2007).

12 S. Iijima. *Nature*, **354**, 56 (1991).

13 S. J Tans, M. H. Devoret, H. Dai, A. Thess, R.E. Smalley, L. J. Geerligs and C Dekker. *Nature*, **386**, 474 (1997).

14 C. Joachim, J. K Gimzewski, R. R Schittler and C. Chavy. *Phys. Rev. Lett*, **74**, 2102 (1995).

15 S. J Tans. *Nature*, **386**, 474 (1997).

16 M. A Reed, C. Zhou, C..J. Muller, T. P. Burgin and J. M. Tour. *Science*, **278**, 252 (1997).

17 R. Tucknott and S.N. Yaliraki. *Chem Phys*, **281**, 455 (2002).

18 L. Langer, V. Bayot, E. Grivei, J. P. Issi, J. P. Heremans, C. H. Olk, L. Stockman, C. Van Haesendonck and Y. Bruynseraede. *Phys. Rev. Lett*, **76**, 479 (1996).

19 S. Roche, F. Triozon, A. Rubio, and D. Mayou. *Phys. Rev. B*, **64**, 121401 (2001).

20 V. Deshpande, M. Bockrath, L. I. Glazman, and A Yacoby. *Nature*, **464**, 209 (2010).

21 P. L. McEuen, M. S. Fuhrer and H. Park. *IEEE Trans. Nanotechnol*, **1**, 78 (2002).

22 A. E. Islam. *Electronics*, **2**, 332 (2013).

23 R. Saito, M. Fujita, G. Dresselhaus and M. S. Dresselhaus. *Phys. Rev. B*, **46**, 1804 (1992).

24 B. Mahar, C. Laslau, R. Yip and Y. Sun. *IEEE. Sensors. J*, **7**, 2 (2007).

25 V. Perebeinos and P. Avouris. *Phys. Rev. Lett*, **101**, 057401 (2008).

26 P. M. Ajayan. *Chem. Rev*, **99**, 1787 (1999).

27 P. Chaturvedi, P. Verma, A. Singh, P. K. Chaudhary, Harsh, and P. K. Basu. *Def. Sci. J*, **58**, 5 (2008).

28 A. A Eliseev, M. V Kharlamova, M. V Chernysheva, A. V Lukashin, Y. D Tretyakov, A. S Kumskov and N. A Kiselev. *Russ. Chem. Rev*, **78**, 9 (2009).

29 Z. K. Tang, L. Zhang, N. Wang, X. X. Zhang, G. H. Wen,G. D. Li, J. N. Wang, C. T. Chan, P. Sheng. *Science*, **292** (2001).

30 F. D. M Haldane. *J Phys. C: Solid State Phys*, **14**, 2585 (1981).

31 E. M. Landau and L. D. Lifshitz. *Course of Theoretical Physics. Vol. 9*. Addison-Wesley, (1980).

32 H. Steinberg, G. Barak, A. Yacoby, L. N. Pfeiffer, K. W. West, B. I. Halperin and K. Le Hur. *Nat. Phys.*, **4**, 116 (2008).

33 C. Blumenstein, J. Schafer, S. Mietke, S. Meyer, A. Dollinger, M. Lochner, R. Matzdorf and R Claessen. *Nat. Phys.*, **7**, 776 (2011).

34 R. Egger and A. O. Gogolin. *Eur. Phys. J. B*, **3**, 281 (1998).

35 M. Bockrath, D. H. Cobden, J. Lu, A. G. Rinzler, R. E. Smalley, L.Balents, and P. L. McEuen. *Nature (London)*, **397**, 598 (1999).

36 Z. Yao, H. W. C. Postma, L. Balents and C. Dekker. *Nature (London)*, **402**, 273 (1999).

37 Y. Jompol, C.J.B. Ford, J.P. Griffiths, I.Ferrer, G.A.C Jones, D Anderson, D.A Ritchie, T.W Silk, A.J Schofield. *Science*, **325**, 597 (2009).

38 P. Avouris. *Acc. Chem. Res*, **35**, 1026 (2002).

39 T. H. Ning. *IEEE Solid-State Circuits Newsletter*, **12**, 27 (2007).

40 R. Chau, B. Doyle, S. Datta, J. Kavalieros and K. Zhang. *Nat. Mater.*, **6**, 810 (2007).

41 M. Fuechsle, J. A. Miwa, S. Mahapatra, H. Ryu, S. Lee, O. Warschkow, L. C. L. Hollenberg, G. Klimec and M. Y. Simmons. *Nat. Nano*, **7**, 242 (2012).

42 A. Javey, J. Guo, Q. Wang, M. Lundstrom and H. Dai. *Nature*, **424**, 654 (2003).

43 J. E. Field. *The Properties of natural and synthetic diamond*. Academic Press, (1992).

44 A. K Novoselov and K. S. Geim. *Nat. Mater.*, **6**, 183 (2007).

45 M. S. Dresselhaus, A. Jorio and R. Saito. *Annu. Rev. Condens. Matter Phys*, **1**, 89 (2010).

46 K. S. Novoselov. *Rev. Mod. Phys*, **83**, 837 (2011).

47 C. Jae-Young, K. Taek, C. Seong-Ho and C. Hyun-Jong. *Nature* , **479**, 338 (2011).

48 S. K. Min, W. Y. Kim, Y. Cho and K. S. Kim. *Nat. Nanotechnol.*, **6**, 162 (2011).

49 R. Setton. *Synth Met*, **23**, 467 (1988).

50 M. T. Yin. *Phys. Rev. B*, **29**, 6996 (1984).

51 H. W. Kroto, J. R. Heath, S. C. O'Brien, R. F. Curl and R. E. Smalley. *Nature* , **318**, 162 (1985).

52 A. Sedlmayr and E. Goeres. *Chem. Phys. Lett*, **184**, 310 (1991).

53 S. Bosi, T. Da Rosail, G. Spalluto and M. Prato. Euro. J. Med. Chem, **13,** 913 (2003).

54 D. S. Bethune, C. H. Kiang, M. S. de Vries, G. Gorman, R. Savoy, J. Vazquez and R. Beyers. *Nature*, **363**, 605 (1993).

55 S. Iijima and T. Ichihashi. *Nature*, **363**, 603 (1993).

56 M. Monthioux, P. Serp, E. Flahaut, M. Razafinimanana, C. Laurent, A. Peigney, W. Bacsa and J. M. Broto. *Introduction to Carbon Nanotubes*. Springer, 2007.

57 R. Bandyopadhyaya, E. Nativ-Roth, O. Regev and R. Yerushalmi-Rozen. *Nano Lett.*, **2**, 25 (2002).

58 T. Ando. *J. Phys. Soc. Jpn*, **74**, 777 (2005).

59 J. W. G. Wilder, L. C. Venema, A. G. Rinzler, R. E. Smalley and C. Dekker. *Nature*, **391**, 59 (1998).

60 M. Ouyang, J. Huang , and C. M. Lieber. *Acc. Chem. Res.*, **35**, 1018 (2002).

61 G. Goldsman and N. Pennington. *Phys. Rev. B*, **68**, 045426 (2003).

62 H. Katauraa, Y. Kumazawaa, Y. Maniwaa, I. Umezub, S. Suzukic, Y. Ohtsukac and Y. Achibac. *Synth. Met*, **103**, 2555 (1999).

63 B. Q. Wei, R. Vajtai, and P. M. Ajayan. *Appl. Phys. Lett*, **79**, 1172 (2001).

64 J. O. J. Wesstrom. *Phys. Rev. B* , **5**, 16 (1996).

65 G. Cuniberti, M. Sassetti, B. Kramer. *J. Phys. Condens. Matter*, **8**, 2 (1996).

66 P. J. Burke. *IEEE Trans. Nano*, **1**, 129 (2002).

67 S. Salahuddin, M. Lundstrom, and S. Datta. *IEEE Trans, Electron Devices*, **52** , (1734).

68 M. C. A. M. Koolen, J. A. M. Geelen and M. P. J. G. Versleijen. " An improved de-embedding technique for on-wafer high-frequency characterization", Bipolar Circuits and Technology Meeting (Minneapolis 1991).

69 Y. Ma, P. O. Lehtinen, A.S. Foster and R. M. Niemine. *New J. Phys*, **6**, 68 (2004).

70 D. W. Boukhvalov and M. I. Katsnelsona. *Eur. Phys. J. B*, **68**, 529 (2009).

71 K. Lafdi, A. Chin, N. Ali and J. F. Despres. *J. Appl. Phys*, **79**, 6007 (1996).

72 W. Kratschmer, L. D. Lamb, K. Fostiropoulos, and D. R Huffman. *Nature*, **347**, 354 (1990).

73 P. M. Ajayan and T. W. Ebbesen. *Nature*, **358**, 220 (1992).

74 E. Joselevich, H.Dai, J. Liu, K. Hata, J. Liu, A. H. Windle. *Top. Appl. Phys*, **111**, 101 (2008).

75 A. M. Cassell, J. A. Raymakers, J. Kong and H. Dai. *J. Phys. Chem. B*, **103**, 6484 (1999).

76 T. Guo, P. Nikolaev, A. Thess, D. Colbert and R. Smalley. *Chem. Phys. Lett*, **243**, 49 (1995).

77 M. C. Hersam. *Nat. Nanotechnol*, **3**, 387 (2008).

78 A. Vijayaraghavan, S. Blat, D. Weissenberger, M. Oron-Carl, F. Hennrich, D. Gerthsen, H. Hahn and R. Krupke. *Nano Lett*, **7**, 1556 (2007).

79 M. Duchamp, K. Lee, B. Dwir, J. W. Seo, E. Kapon, L. Forro and A. Magrez. *ACS Nano*, **4**, 279 (2010).

80 M. Semke and E.D Zheng. *J. Am. Chem. Soc*, **129**, 6084 (2007).

81 Li, W. Xue and P. Dielectrophoretic Deposition and Alignment of Carbon Nanotubes. In Yellampalli, S., ed., *Carbon Nanotubes - Synthesis, Characterization, Applications*. InTech, 2011.

82 F. Seichepine, S. Salomon, M. Collet, S. Guillon, L. Nicu, G. Larrieu, E. Flahaut, and C. Vieu. *Nanotechnology*, **23**, 1 (2012).

83 M. F. Lin, D. S. Chuun, and K. Shung. *Phys. Rev. B,* **56**, 1430 (1997).

84 A. Glatz, V. I. Kozub, V. M. Vinokur. *Theory of Quantum Transport in Metallic and Hybrid Nanostructures*. Springer, (2003).

85 V. P. Singh, A. Agrawal and S. B. Singh. *International Journal of Soft Computing and Engineering*, **2**, 2231 (2012).

86 J. E. Fischer, H. Dai, A. Thess, R. Lee, N. M. Hanjani, D. L. Dehaas, and R. E. Smalley. *Phys. Rev. B*, **55**, 4921 (1997).

87 A. B. Kaiser. *Rep. Prog. Phys*, **64**, 1 (2001).

88 J. S. Dugdale. *The Electrical Properties of Disordered Metals*. Cambridge University Press, (1995).

89 M. A Gallagher, B. L Howson. *Phys. Rep*, **170**, 265 (1988).

90 N. F. Mott, E. A. Davis. *Electronic proceesses in non-crystalline materials*. Oxford City Press, (1979).

91 A. Einstein. *Z. Phys*, **18**, 121 (1917).

92 F. M. Dickey. *Optics and Photonics News*, **14**, 30 (2003).

93 G. A. Mesyats, V. V. Osipov and V. F. Tarasenko. *Optics & Photonics News*, **6**, 48 (1995).

94 M. E. Innocenzi, H. T. Yura, C. L. Fincher and R.A. Fields. *Appl. Phys. Lett*, **56**, 1831 (1990).

95 Y. Silberberg, P. W. Smith, D. J. Eilenberger, D. A. B. Miller, A. C. Gossard and W. Wiegmann. *Optics. Lett*, **9**, 507 (1984).

96 G. H. B. Thompson. *Physics of semiconductor Laser devices*. Wiley-Interscience, (1980).

97 N. Bohr. *Philos. Mag*, **26**, 476 (1913).

98 C. D. Scott, S. Arepalli, P. Nikolaev, R.E. Smalley. *Appl. Phys. A*, **72**, 573 (2001).

99 S. Lebedkina, P. Schweissb, B. Renkerb, S. Malika, F. Hennrichc, M. Neumaierc, C. Stoermerc and M. M. Kappesa. *Carbon*, **40**, 417 (2002).

100 A. Jorio, C. Fantini, M. Dantao, M. A. Pimenta, A. G. Souza Filho and G. G. Samsonidze. *Phys. Rev B*, **66** , 115411 (2002).

101 E. Borowiak-Palen, E. Mendoza, A. Bachmatiuk, M.H. Rummeli, T. Gemming, J. Nogues, V. Skumryev, R.J. Kalenczuk, Pichler and S.R.P. Silva. *Chem. Phys. Lett*, **421**, 129 (2006).

102 S. S. Harilal, T. Sizyuk, A. Hassanein, D. Campos, P. Hough, and V. Sizyuk. *J. Appl. Phys*, **109**, 063306 (2011).

103 S. M. Bachilo, M. S. Strano, C. Kittrell, R. H. Hauge, R. E. Smalley and R. B. Weisman. *Science*, **298**, 2361 (2002).

104 S. S. Islam, K. A. Shah, H. S. Mavi, A. K. Shaukla and S. R. Harsh. *Mater. Sci.*, **30**, 295 (2007).

105 A. M. Rao, E. Richter, S. Bandow, B. Chase, P. C Eklund, K. A. Williams, S. Fang, K. R. Subbaswamy, M. Menon, A. Thess, R. E. Smalley, G. Dresselhaus and M. S. Dresselhaus. *Science*, **275**, 187 (1997).

106 J. Kong, N. R. Franklin, C. Zhou, M. G. Chapline, S. Peng, K. Cho, H. Dai. *Science*, **287**, 622 (2000).

107 P. G. Collins, A. Zettl, H. Bando, A. Thess, R. E. Smalley. *Science*, **278**, 100 (1997).

108 M. Pollak and B.I. Shklovskii. *Hopping transport in solids*. Elsevier, (1990).

109 C. Kane. *Phys. Rev. Lett.*, **79**, 5086 (1997).

110 A. G. Zabrodskii. *Philos. Mag. B* , **81**, 1131 (2001).

111 V. L. Nguyen, B. Z. Spivak, and B. I. Shklovskii. *Phys. JETP*, **62**, 1021 (1985).

112 M. E. Raikh and G. F. Wessels. *Phys. Rev. B* , **47**, 15609 (1993).

113 D. P. Wang et al. *arXiv:cond-mat*, 0610747 (unpublished).

114 G. Chimowa, E. C. Linganiso, D. Churochkin, N. J. Coville, and S. Bhattacharyya. *Phys. Rev. B* , **84**, 205429 (2011).

115 Y. L. Zhao, W. M. Lv, Z. Q. Liu, S. W. Zeng, M. Motapothula et al. *AIP*

Advances, **2**, 012129 (2012).

116 N. V. Agrinskaya and V. I. Kozub. *Phys. Status Solidi B* , **205**, 11 (1998).

117 M. Jaiswal, W. Wang, K. A. Shiral Fernando, Y. P. Sun and R. Menon. Phys. Rev. B, 113401 (2007).

118 Yoshida, H Fukuyama and K. *J. Phys. Soc. Jpn*, **46**, 102 (1979).

119 P. L. McEuen. *Physics World*, **12**, 31 (2000).

120 C. Bourbonnais and D. Jérome. Springer Series in Materials Science. In Lebed, A., ed., *The Physics of Organic Superconductors*. Springer, Heidelberg, 2008.

121 O. Ciftja. *Int. J. Mod. Phys. B*, **26**, 1244001 (2012).

122 J. Voit. *Rep. Prog. Phys*, **58**, 977 (1995).

123 D. G. Angelakis, M. Huo, E. Kyoseva, and L. C. Kwek. *Phys. Rev. Lett*, **106**, 153601 (2011).

124 K. A Glazman and L. I. Matveev. *Phys. Rev. Lett*, **70**, 990 (1993).

125 P. J. Cote and L. V. Meisel. *Phys. Rev. Lett.* , **40** , 1586 (1978).

126 K. Frobose and J. Jackle. *Journal of Physics F: Metal Physics*, **7**, 2331 (1977).

127 T. Matsuda, N. Shiotani, and U. Mizutani. *Journal of Physics F: Metal Physics*, **14**, 1193 (1984).

128 U. Mizutani and K. Yoshino. *Journal of Physics F: Metal Physics* , **14**, 1179 (1984).

129 M. Bockrath, D. H. Cobden, P. L. McEuen, N. G. Chopra, A. Zettl, A. Thess, R. E. Smalley. *Science*, **275**, 1922 (1997).

130 V. V. Deshpande, M. Bockrath, L. I. Glazman and A. Yacoby. *Nature*, **464**, 209 (2010).

131 M. Bockrath, D. H. Cobden, P. L. McEuen, N. G. Chopra, A. Zettl, A. Thess, R. E. Smalley. *Science*, **275**, 1922 (1997).